Modeling generation and characterization of attosecond pulses

by

Siddharth Bhardwaj

B.S.,Electrical Engineering, University of Southern California (2007)
S.M., Massachusetts Institute of Technology (2010)

Submitted to the Department of Electrical Engineering and Computer Science
in partial fulfillment of the requirements for the degree of

Doctor of Philosophy in Electrical Engineering and Computer Science

at the

MASSACHUSETTS INSTITUTE OF TECHNOLOGY

June 2014

Signature redacted

Author .....
Department of Electrical Engineering and Computer Science
May 20, 2014

Signature redacted

Certified by .....
Franz X. Kärtner
Adjunct Professor of Electrical Engineering
Thesis Supervisor

Signature redacted

Accepted by .....
Leslie A. Kolodziejski
Professor of Electrical Engineering
Chair, Department Committee on Graduate Students

Modeling generation and characterization of attosecond pulses

by

Siddharth Bhardwaj

Submitted to the Department of Electrical Engineering and Computer Science
on May 20, 2014, in partial fulfillment of the
requirements for the degree of
Doctor of Philosophy in Electrical Engineering and Computer Science

Abstract

Generation of high-order harmonics has emerged as a powerful technique for the generation of broadband coherent radiation in the EUV regime. This has lead to the development of table-top EUV sources that can produce attosecond pulses. These pulses can serve as a probe to resolve atomic attosecond dynamics and image atomic orbitals and molecular motion. Due to high spatial and temporal coherence, high-order harmonic radiation can also be used to seed free electron lasers, which allow the generation of high-intensity X-ray radiation that can be used for imaging bio-molecules.

Since the first observation of high-order harmonics, effort has been made to accurately model both the generation and the characterization of attosecond pulses. Work on the modeling of high harmonic generation can be divided into two parts: (a) description of the interaction between the IR pulse and atoms that leads to emission of attosecond pulses (the single atom response) and (b) modeling of the propagation of attosecond pulses by accounting for macroscopic phase matching effects. In this work, we will focus on the single atom response which can be calculated either by numerically solving the time dependent Schrödinger equation (TDSE) or through the semi-classical three step model (TSM).

In Chapter 2, the theory of light-atom interaction will be reviewed with the focus on the calculation of the dipole trasition matrix element (DTME) in the strong field formalism. It will be shown that the choice of the basis states - Volkov states and Coulomb Volkov states - to describe electrons in the continuum is crucial to the accuracy of DTME calculation. In Chapter 3, the TSM will be derived from the Schrödinger equation by using the saddle point approximation. Through this derivation, the quantum mechanical laser-atom interaction is reduced to a semi-classical model comprising of ionization, propagation and recombination . The numerical scheme for solving the TDSE will be discussed. It will then be used to demonstrate the generation of isolated attosecond pulses from non-sinusoidal sub-cycle pulses. The results of ADK and non-adiabatic ionization models will be compared with that from numerical TDSE, and then used to calculate the harmonic spectra in the tunneling

and multi-photon ionization regimes.

The recombination step of the TSM, which plays a crucial role in determining the qualitative shape of the high-order harmonic spectrum, will be investigated in Chapter 4. A commonly observed feature of Argon's high-order harmonic spectrum is the presence of a minimum at around 50 eV called the Cooper minimum. The minimum in the high-order harmonic spectrum has been attributed to the minimum in the recombination amplitude. The recombination amplitude will be calculated - in the strong field formalism - using length and acceleration form for two choices of continuum electron wavefunction description (Volkov and Coulomb-Volkov).

Attosecond pulse characterization techniques, which are an extension of the sub-picosecond pulse characterization technique like FROG and SPIDER, rely on the photoionization process to transfer the amplitude and phase information of the attosecond pulse to the photoelectron spectrum. For accurate pulse characterization, it is crucial to model the photoionization process accurately. Since photoionization and recombination are reverse processes, the improvements in the calculation of the recombination amplitude in Chapter 4, can be used to improve the model function of the pulse retrieval algorithm. It will be shown that the proposed improvements are crucial for accurate characterization of low energy EUV pulses

Thesis Supervisor: Franz X. Kärtner
Title: Adjunct Professor of Electrical Engineering

Acknowledgments

Ernest Hemingway is said to have once remarked: "It is good to have an end to journey toward; but it is the journey that matters, in the end." My journey, that began at a quaint boarding school in Kurseong, has taken me through New Delhi, Los Angeles and finally to Cambridge. Now that I am at the verge of finishing my PhD, it is but natural to look back and acknowledge the contribution of all those who helped me get here.

I am grateful to my advisor, Prof. Franz Kärtner for giving me the opportunity to be a part of this group. Franz is a great scientist and I have always been in awe of the breadth and depth of his knowledge. I was struck by his optimistic nature, and his ability to motivate and inspire deflated spirits. However, if I had to choose one attribute that I would like to embody, it would undoubtedly be Franz's work ethic. I am amazed by his ability to seamlessly supervise two groups on two continents. I am also grateful to him for giving me the opportunity to spend a year at DESY (Deutsches Elecktronen-Synchrotron) where I collaborated with Prof. Robin Santra and Dr. Sang-Kil Son. Working with Prof. Santra and Dr. Sang-Kil Son was a great learning experience, and I am grateful to them for patiently answering my questions.

I would also like to thank Prof. Ippen and Prof. Orlando for agreeing to be on my thesis and RQE committees. They carefully perused through my thesis and provided valuable feedback. I was also a teaching assistant in Prof. Orlando's graduate course on applied quantum and statistical physics. I realized that one can truly claim to understand a subject only after he/she can teach it to others.

I developed a special kinship with Anatoly Khilo and Vasileios Gkortsas, my officemates for almost six years. We had many interesting discussions over a wide range of topics, not all of which can be mentioned in this acknowledgement! Vasileios was also with me in Germany, where we spent our weekends either travelling or complaining about the weather. Over the last two years, I have worked closely with Donnie Keathley. He patiently showed with me the ropes in the lab. We spent countless hours, sometimes over the weekends, discussing physics and the life of a

graduate student. In the process, we became close friends. I would also like to thank Dr. Jeff Moses for guiding and mentoring me whenever I needed help. Dr. Guillaume Laurent joined our lab towards the end of my PhD. He brought a fresh perspective and played an integral role in our work on the characterization of attosecond pulses. I am also grateful to the other members of the OQE group who made working at MIT a great experience. Prof. Gene Bickers, you helped me discover my love for physics without which I probably would not have gone to graduate school.

Seven years at an institution is a long time. My journey at MIT would not have been possible without the encouragement and support of my friends. Thank you Himanshu Dhamankar for being a close friend and a roommate for several years. I thoroughly enjoyed your excellent cooking. I would also like to thank Daniel Prashanth, Jaisree Iyer, Somani Patnaik, Omair Sadaat and Sreerang Chhatre. In my last two years at 218 Broadway, I spent a lot of time with my roommates: Tushar Krishna, Sourav Padhy, Harshad Kasture and Muralidaran Vijayaraghavan. We had a great time pulling each others leg and discussing, sometimes vigorously, topics ranging from movies to Indian politics to "Democracy Now." Graduate school experience would have been monotonous without your company . I would also like to thank Bhavya Chhaochharia, my friend for over 20 years. I always looked forward to talking to you over the phone and meeting you when I visited India.

I would not have made it to MIT, much less get a PhD, without the support and sacrifice of my family members in India and in the US. I remember that many years ago, Shivajee mama had written a letter to my mother expressing how nice it would be if somebody from our family got an education at a reputed institution like MIT. Years later, when I came to the US for undergrad, I found a second home at Saratoga. Thank you Shivajee mama, Parul mami and Sanjay mama! I am also thankful to my father who spent numerous sleepless nights when we traveled from Patna to Kurseong; my grandfather for relentlessly tutoring me when I was a boy; my grandmother for her excellent cooking; my brother for the fun times we have had together; and last but not the least, my mother, for her love.

Contents

List of Figures

List of Tables

Chapter 1

Introduction

Invention of lasers as a source for bright coherent radiation, in the early 1960's, revolutionized many areas of research [9]. The intensity of the laser was strong enough to lead to nonlinear light-matter interaction such as generation of second and third harmonics. These interactions could be described using perturbation theory. Invention of chirped pulse amplification led to further increase in laser field strengths which then became comparable to atomic electric fields [10].

The increase in the laser intensity was accompanied by the decrease in the pulse duration. As shown in Figure 1-1, invention of modelocking techniques, soon after the invention of the laser led to an exponential decrease in the pulse duration from picoseconds to tens of femtoseconds. By mid 1980's, the modelocking techniques had been pushsed to its limits and the dramatic decrease in pulse duration, that occured during the previous decade, considerably waned. In order to push the pulse duration down into the attosecond regime, a new technique of generating coherent multi-eV broadband radiation was needed. This break through came in the form of high-order harmonic generation process which was a result of the ability to generate laser fields to perform nonlinear optics in the non-perturbative regime.

One of the first observation of high-order harmonic generation was when researchers were trying to look into the photoelectron spectrum of Xe interacting with intense laser fields ($\sim 10^{13}\mathrm{W/cm^2}$) from Nd:YAG laser (1064 nm) [11]. As high as 21^{st} harmonics were observed which were separated by twice the Nd:YAG laser fre-

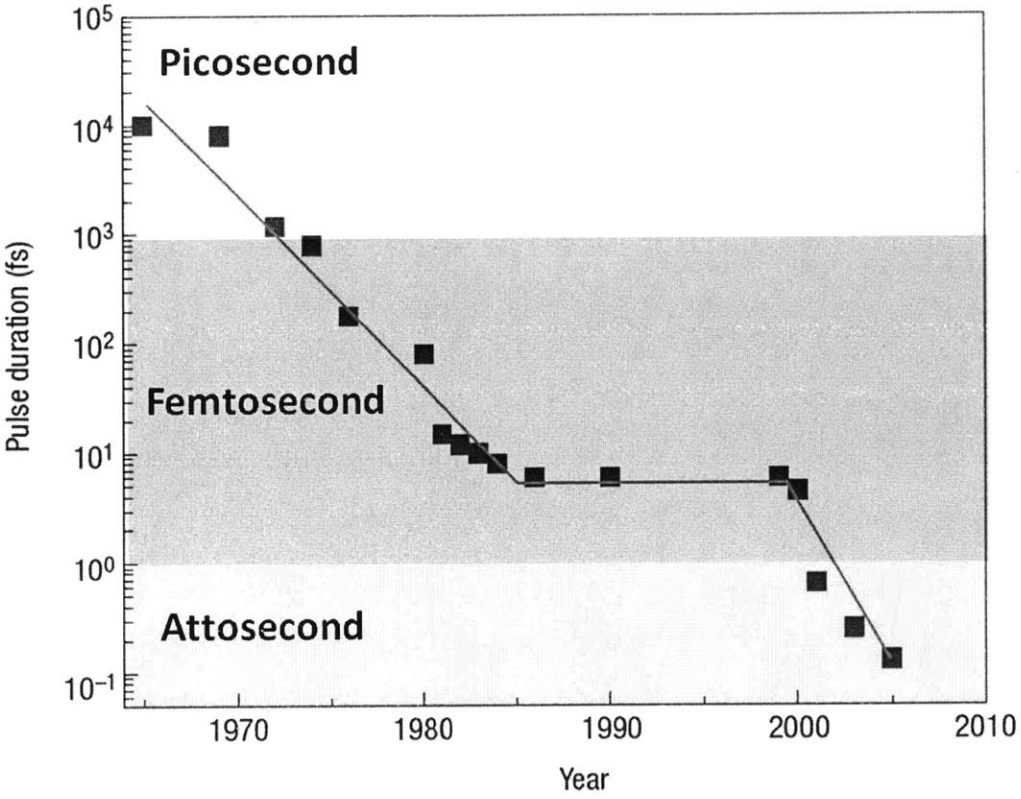

Figure 1-1: Duration of the shortest available pulse vs time. Invention of modelocking in 1964 and high-order harmonic generation in 2000 led to dramatic decline in the pulse duration. This figure is taken from [1]

quency. A characteristic feature of the high-order harmonic was the existence of a broad plateau marked by a sudden cut-off. See Figure 1-2. Moreover, the plateau was broad enough to sustain pulses in the attosecond regime.

The theoretical techniques, such as perturbation theory, that were used to describe perturbative nonlinear optics, could not explain the high-order harmonic spectrum. Two approaches were taken to model the high harmonic generation process. The first was to solve the time dependent Schrödinger equation of intense laser-atom interaction [12]. The second was the development of a semi classical three step model in which the quantum mechanical laser-atom interaction was reduced to ionization of outermost electron, its propagation under the influence of the laser field and then recombination back to the atom [13]. The three step model was able to reproduce

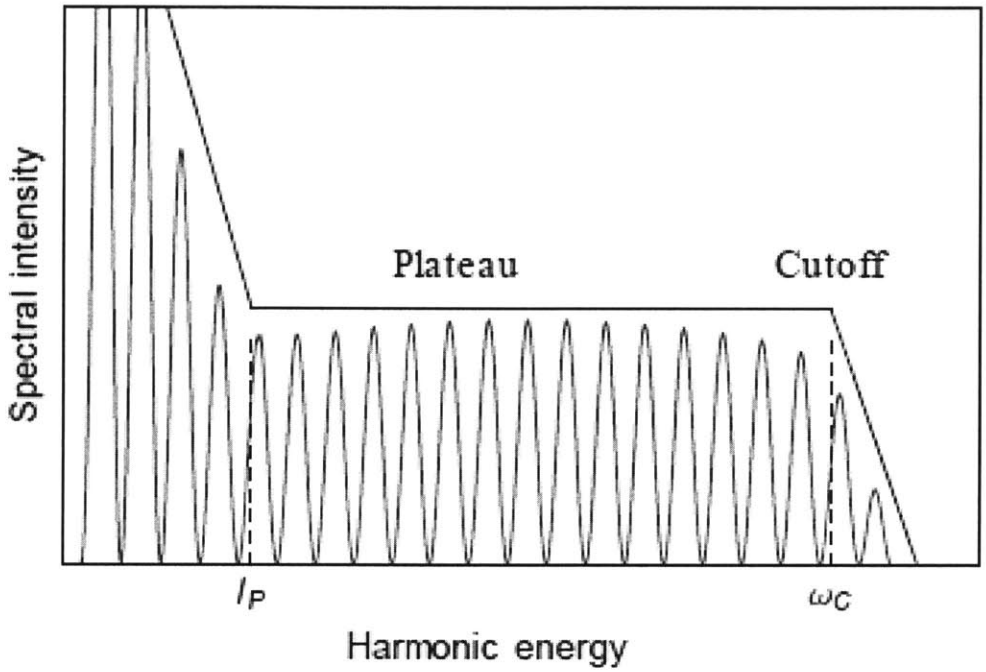

Figure 1-2: High order harmonic spectrum has a plateau comprising of harmonics that are separated by twice the driver laser wavelength. There is a sudden drop in harmonic intensity after the cutoff frequency. This figure is taken from [2]

the the qualitative feature - existence of odd harmonics and sharp cut-off - of the harmonic spectrum

By Heisenberg time-energy uncertainty principle, the timescale of electronic motion is inversely proportional to the energy difference between the energy levels. In molecules, the typical energy seperations are that of millielectronvolts which corresponds to timescales of hundred femtosecond. Electronic transition in molecules has been observed through pump-probe techniques that use femtosecond pulses [14].This area of research, referred to as femtochemistry, led to a noble prize in 1999 to Ahmed Zewail. The separation of energy level in atoms is of the order of electron volts. Observations of electronic transition in atom requires attosecond precision. This became possible after the invention of high harmonic generation.

Attosecond pulses serve as a window into the world of electrons in two ways. The first, called high harmonic interferometry, is based on the coherent nature of the high harmonic generation process. The ionized electron serves as a probe: the amplitude and phase of the harmonics that are generated due to the recombination of the electron provide a snapshot of the bound electron dynamics at the time of recombination. This idea was used to image the outermost orbital - both amplitude and phase - of N_2. [15]. Similarly, the attosecond multi-electron dynamic of the orbitals of CO_2 that participate in the harmonic generation process was decoded [16]. Attosecond pulses are also used in pump-probe experiments: the femtosecond pump pulse sets the electron dynamics in motion which is then probed by the attosecond pulse. This technique was used to measure in real time the subfemtosecond motion of valence electrons Krypton over a multifemtosecond time span [17].

The generation of attosecond pulses also spurred the developement of attosecond metrology techniques. These techniques rely on the photoionization process through which the amplitude and phase information of the attosecond pulse is transferred to the photoelectron spectrum. Once the photoelectron pulse is generated, their phase is modulated by an IR field. By measuring the photoelectron spectrum for various delays between the attosecond and the IR pulse, the amplitude and phase of the attosecond pulse can be reconstructed. In pump-probe experiments it is critical to know the duration and the spectrum of attosecond pulses.

The recombination step in the generation of attosecond pulses and the ionization step in the characterization of attosecond pulses are very similar . While the first involves the transition of electrons from the continuum to the bound state, the second involves the transition of electrons from the boundstate to the continuum. Therefore it is extremely important to ensure that the ionization and recombination steps in the modeling of high harmonic within the strong field approximation formalism is accurate. In this thesis these processes will be accurately modeled within the strong field approximation. It will be shown that inability to do so can lead to significant errors in our ability to model the generation and characterization of attosecond pulses.

Chapter 2

Theory of laser-atom interaction

In this chapter the formalism of laser-atom interaction is reviewed. In particular, emphasis will be laid on the derivation of the transition amplitude from the strong field formalism. In order to get a closed analytical expression for the transition amplitude, approximations need to be made to the exact form of the time propagator. The accuracy of the transition amplitude depends on the manner in which the propagator, represented by a dyson series, is terminated and the choice of the initial and final states [18]. To illustrate this, the derivation of the first order perturbation theory will be presented along with the claculation of the total and the differential photoionization cross-section. Next, the formalism of strong field approximation will be presented. This will serve as the basis for the derivation of the three step model in Chapter 3, the recombination amplitude in Chapter 4 and the photoelectron distribution in Chapter 5.

2.1 Equations for laser atom interaction

We start with the Schrödinger equation

$$i\frac{d}{dt}|\psi(t)\rangle = H(t)|\psi(t)\rangle \tag{2.1}$$

Here, $|\psi(t)\rangle$ is the multi-electron wavefunction. $H(t)$ is the hamiltonian of interaction between the laser field and the bound electrons of an atom. The hamiltonian can be partioned into two parts: the atomic part and the interaction part:

$$H(t) = H_0 + H_I(t) \tag{2.2}$$

The hamiltonian of an atom with atomic number Z is given by:

$$H_0 = \sum_{j=1}^{Z} \left(\frac{\mathbf{p}_j^2}{2} - \frac{Z}{\mathbf{r}_j} \right) + \sum_{j>k} \frac{1}{|\mathbf{r}_j - \mathbf{r}_k|} \tag{2.3}$$

The terms inside the bracket are the kinetic energy and the potential energy (due to the nucleus) of the j^{th} electron. The next term is the electron-electron interaction term. In the length gauge, the interaction of the atom with an electric field $\mathbf{E}(t)$ is given by:

$$H_I(t) = -\mathbf{E}(t) \sum_{j=1}^{Z} \mathbf{r}_j \tag{2.4}$$

Solving Equation 2.1 exactly for a multi-electron atom is not possible. It is common to use the *Single Active Electron* (SAE) approximation which assumes that only a single electron in the atom is "active" and interacts with the laser and the other electrons remain frozen. As we will see in Chapter 4, this approximation fails to account for electron-electron correlation effects which is responsible, for example, for the giant resonance in the harmonic spectrum of Xenon [19]. In spite of these limitations, the SAE approximation has been used to predict experimentally measured high-order harmonic spectra both analytically [20, 21] and numerically [12], and to model the photoionization process [6, 22, 23].

After the SAE approximation, the total hamiltonian of a multi-electron atom interacting with a linerly polarized electric field reduces to the hamiltonian of a one electron atom with an effective potential $V_{eff}(\mathbf{r})$:

$$\tilde{H}(t) = \frac{\mathbf{p}^2}{2} + V_{eff}(\mathbf{r}) - E(t)z. \tag{2.5}$$

The central potential can be obtained by Hartree-Fock Theory [24] or Hartree-Fock theory where the exchange interaction is replaced by a local density approximation [25].

2.2 Transition Amplitude

Quantum mechanics has provided the tools to describe physical processes such as light-atom interaction and scattering phenomena. Central to such a description is the idea of transition amplitude - the probability (the absolute square of the transition amplitude) of transitioning to a certain state provided the initial state and the interaction hamiltonian are known. The expression for the transition amplitude can be obtained by writing Equation 2.1 in the integral form:

$$|\psi(t)\rangle = U(t, t_0)|\psi(t_0)\rangle \tag{2.6}$$

$U(t, t_0)$ is the unitary time evolution operator which leads to the time evolution of a state from $|\psi(t_0)\rangle$ to $|\psi(t)\rangle$. It is the exponential of the total hamiltonian of the system

$$U(t, t_0) = e^{-i\int_{t_0}^{t} H(t')dt'} \tag{2.7}$$

The time evolution propagator also satisfies the Schrödinger equation:

$$i\frac{d}{dt}U(t, t_0) = H(t)U(t, t_0) \tag{2.8}$$

If the total hamiltonian is partioned into the atomic part and the interaction part, as shown in Equation 2.2, the time propagator can be written as:

$$U(t, t_0) = U_0(t, t_0) - i\int_{t_0}^{t} U(t, t')H_I(t')U_0(t', t_0)dt' \tag{2.9}$$

U_0 is the time propagator of the field-free atomic hamiltonian H_0, while U is the time-propagator of the total hamiltonian H. If the interaction hamiltonian $H_I(t)$

becomes zero, the time propagator reduces to the field-free propagator. The second term on the right hand side of Equation 2.9 can be interpreted as follows: the system evolves between t_0 and t' as if the perturbation (which in our case is the external electromagnetic field) does not exist; at t', the system "sees" the perturbation; after which the system evolves under the influence of the total hamiltonian. Thc transition amplitude form the initial state $|\psi_i(t_0)\rangle$ to a state $|\psi(t)\rangle$ is given by:

$$a_{if} = \langle\psi_f(t)|U(t,t_0)|\psi_i(t_0)\rangle \tag{2.10}$$

Thus far, no approximation has been made and the expression for transition amplitude in Equation 2.10 is exact. Since the exact time evolution operator U appears on both sides in Equation 2.9, a closed form for the transition amplitude (Equation 2.10) cannot be obtained. In order to obtain a closed form for the transition amplitude, it is common to make various approximations. These approximations are based on an intuitive understanding of the physics of the problem at hand. In the following sections, we will overview some of these approximations for various physical situations.

2.3 Perturbation theory

Perturbation theory is commonly used to analyze a quantum system where ($H_I << H_0$). It has been used to describe both time-independent perturbation, as in the case of relativistic corrections to the Schrödinger equation such as spin-orbit coupling and fine structure; and time-dependent perturbation, as in the case of an electromagnetic field causing bound-bound and bound-continuum transitions in atoms. Understanding bound-bound transitions using the perturbation theory has been used to calculate nonlinear optical susceptibilites [26]. Similarly, perturbatively calculated bound-continuum transition amplitude have been used to calculate photoionization cross section [22]. In this section, we will derive the first-order transition amplitude for bound-bound and bound-continuum transitions; then the bound-continuum transition will be used to derive the photoionization cross section. This will be useful in the later chapters where the high-harmonic generation process and pulse characteri-

zation techniques are discussed.

The eigenstates $|\varphi_n\rangle$ of H_0 constitute a complete orthonormal basis set with eigenenergies E_n:

$$H_0|\varphi_n\rangle = E_n|\varphi_n\rangle \tag{2.11}$$

The time evolution of the unperturbed eigenstate is given by

$$U_0(t,t_0)|\varphi_n\rangle = e^{-iE_n(t-t_0)}|\varphi_n\rangle \tag{2.12}$$

where U_0 is the time propagator of H_0. The exact time propagator of the total hamiltonian $H_0 + H_I(t)$ is given by [18]

$$U(t,t_0) = U_0(t,t_0) + \sum_{n=1}^{\infty} U_I^{(n)}(t,t_0) \tag{2.13}$$

where

$$U_I^{(n)}(t,t_0) = \Big(-i\Big)^n \int_{t_0}^{t} dt_1 \int_{t_0}^{t_1} dt_2 \cdots \int_{t_0}^{t_{n-1}} dt_n U_0(t,t_1)H_I(t_1)U_0(t_1,t_2)H_I(t_2)\cdots U_0(t_{n-1},t_n)H_I(t_n)U_0(t_n,t_0) \tag{2.14}$$

Equation 2.14 is very general. For laser-atom interaction, the n^{th} term corresponds to the absorption of n photons. In a scattering problem, the n^{th} term refers to the physical situation where the particle has interacted with the scattering potential n times. In first-order perturbation theory, the expansion is limited to $n = 1$:

$$U^{(1)}(t,t_0) = U_0(t,t_0) - i\int_{t_0}^{t} dt' U_0(t,t')H_I(t')U_0(t',t_0) \tag{2.15}$$

If at t_0, the system is in $|\varphi_i\rangle$ state, then the amplitude of transitioning to $|\varphi_f\rangle$ at time t is obtained by inserting Equation 2.15 into Equation 2.10:

$$a_{if}^{(1)} = -i \int_{t_0}^{t} dt' e^{i\omega_{mn}t'} H_I^{mn}(t') \tag{2.16}$$

Here the $H_I^{mn}(t') = \langle \psi_m | H_I(t') | \psi_n \rangle$ is the transition matrix element, and

$$\omega_{mn} = \frac{E_m - E_n}{\hbar} \tag{2.17}$$

is the transition frequency

2.3.1 Bound-Bound tansition

Next, we want to understand electronic transition from one bound state to another in an atom due to sinusoidal electric field given by:

$$\mathbf{E}(t') = \hat{\mathbf{z}} \frac{E_0}{2} (e^{i\omega_0 t'} + e^{-i\omega_0 t'}). \tag{2.18}$$

Again, SAE approximation is employed which results in an effective centro-symmetric potential V_{HFS}. In the spherical coordinate system, the initial and final states are given by:

$$\langle \mathbf{r} | \psi_i \rangle = \psi_i(\mathbf{r}) = \frac{u_i(r)}{r} Y_{l_i m_f}(\Omega_r) \tag{2.19}$$

and

$$\langle \mathbf{r} | \psi_f \rangle = \psi_f(\mathbf{r}) = \frac{u_f(r)}{r} Y_{l_f m_f}(\Omega_r) \tag{2.20}$$

Y_{lm} is spherical harmonic whose azimuthal quantum number is l and magnetic quatum number is m. The radial wavefunction $u(r)$ is calculated by solving

$$\big(-\frac{\nabla^2}{2} + V_{eff}(\mathbf{r}) \big) u(r) = \epsilon u(r) \tag{2.21}$$

Without any loss of generality, we can set $t_0 = 0$.The transition amplitude then becomes

$$a_{if}^{(1)} = -i\frac{E_0}{2}d_{if}\int_0^t dt'\left(e^{i(\omega_{if}+\omega_0)t'} + e^{i(\omega_{if}-\omega_0)t'}\right), \tag{2.22}$$

where

$$d_{if} = \langle\psi_f|\mathbf{r}|\psi_i\rangle = c_l\int_0^\infty dr u_f(r) r u_i(r) \tag{2.23}$$

is the dipole transition matrix element (DTME). The angular integration term is given by:

$$c_l = \int d\Omega_r Y^*_{l_f m_f}(\Omega_r)\cos\theta Y_{l_i m_i}(\Omega_r) \tag{2.24}$$

Using the expression,

$$\cos\theta = \sqrt{\frac{4\pi}{3}}Y_{10}, \tag{2.25}$$

the angular integration can be expressed in terms of Wigner 3j symbol [27]

$$\begin{aligned}&\int Y_{l_1 m_1}(\theta,\phi)Y_{l_2 m_2}(\theta,\phi)Y_{l_3 m_3}(\theta,\phi)\sin\theta d\theta d\phi \\ &= \sqrt{\frac{(2l_1+1)(2l_2+1)(2l_3+1)}{4\pi}}\begin{pmatrix} l_1 & l_2 & l_3 \\ 0 & 0 & 0\end{pmatrix}\begin{pmatrix} l_1 & l_2 & l_3 \\ m_1 & m_2 & m_3\end{pmatrix}\end{aligned} \tag{2.26}$$

Let us analyze the time integral in Equation 2.22. The $\omega_{if}+\omega$ term corresponds to the emission of a photon with angular frequency ω_0, while the $\omega_{if}-\omega$ term corresponds to the absorption of a photon with angular frequency ω_0. If $\omega_{if} > 0$, i.e., the final state $|\varphi_f\rangle$ is energetically higher than the initial $|\varphi_i\rangle$, then the $\omega_{if}+\omega$ terms is referred to as the counter-rotating term and the $\omega_{if}-\omega$ term is referred to as the rotating term. According to the rotating wave approximation (RWA), the counter-rotating term is neglected. This has a physical meaning: the transition from an energetically lower to an energetically higher state is more likely to occur by the absorption of a photon (rotating term) rather than by the emission of a photon (counter-rotating term). Vice-versa is true when $\omega_{if} < 0$. Under the RWA, Equation 2.22 can be

approximated by

$$a_{if}^{(1)} \approx -i\frac{E_0}{2}d_{if}e^{i\frac{\Delta\omega}{2}t}\left(\frac{\sin(\frac{\Delta\omega}{2})t}{\frac{\Delta\omega}{2}}\right), \tag{2.27}$$

where $\Delta\omega = \omega_{if} - \omega_0$ is the detuning term. Finally, the transition probability is given by:

$$P_{if}^{(1)} = \frac{E_0^2}{4}|d_{if}|^2 F(t, \Delta\omega) \tag{2.28}$$

where

$$F(t, \Delta\omega) = \left(\frac{\sin^2(\frac{\Delta\omega}{2}t)}{(\frac{\Delta\omega}{2})^2}\right), \tag{2.29}$$

In the limit $t \to \infty$

$$F(t, \Delta\omega) = 2\pi t\delta(\Delta\omega) \tag{2.30}$$

2.3.2 Bound-Continuum transition

The calculation of a bound-continuum transition probability closely follows the bound-bound transition probability. The main difference is that special care needs to be taken to account for the continuum-spectrum of the final state. This is done through proper normalization of the continuum states along with the correct choice of the density of states. The *momentum normalized* eigenstate representing an electron with momentum k in the direction Ω_k is

$$\psi_k^{sc}(\mathbf{r}) = \frac{1}{k}\sum_{l=0}^{\infty}\sum_{m=-l}^{m=l} i^l e^{-i(\delta_l+\sigma_l)}\frac{u_{kl}^{sc}(r)}{r}Y_{lm}(\Omega_r)Y_{lm}^*(\Omega_k) \tag{2.31}$$

where u_{kl}^{sc} is the radial wavefunction, δ_l is the phase shift against the regular coulomb wave (due to the short-range nature of the V_{eff}) and σ_l is the coulomb phase shift [28]. The radial wavefunction $u_{kl}^{sc}(r)$ can be obtained by solving Equation 2.21 for positive eigenenergies ϵ. The probability of transitioning from $|\psi_i\rangle$ to the state $|\psi_k\rangle$

is given by

$$dP = d\Omega_k \frac{E_0^2}{4} \int dk k^2 |d_k^{sc}|^2 F(t, \omega_k - \omega_0) \tag{2.32}$$

where d_k^{sc} is the dipole transition matrix element for bound-continuum transition. Similar to the case of bound-bound transition (Equation 2.23), it can be written as

$$d_k^{sc} = \langle \psi_k^{sc} | \mathbf{r} | \psi_i \rangle \tag{2.33}$$

Using the delta function relation (for $\omega = \frac{k^2}{2}$)

$$\delta(\omega - \omega_0) = \frac{\delta(k - k_0)}{k} \tag{2.34}$$

and Equation 2.30, the expression for transition probability becomes

$$\lim_{t \to \infty} dP = d\Omega_k \frac{E_0^2}{4} kt |d_k^{sc}|^2. \tag{2.35}$$

The differential photoionization cross section, which is defined as the transition probability per unit time divided by the photon flux, is given by [23]

$$\frac{d\sigma}{d\Omega_k} = \frac{4\pi^2 \omega k}{c} |d_k|^2 \tag{2.36}$$

Equation 2.36 is the cross-section of absorbing a photon ω and emitting an electron in the direction Ω_k with momentum k. The total photoionization cross-section can be obtained by integrating Equation 2.36 over all solid angles. Differential and total photoionization cross-section will be revisited when we discuss recombination amplitudes (Chapter 4) and attosecond pulse characterization (Chapter 5).

2.4 Strong Field Approximation (SFA)

The strong field approximation (SFA) is used to analyze the interaction of an intense IR field with an atom. Unlike the perturbation theory, the interaction hamiltonian

H_I (see Equation 2.2) is of the same order as the atomic hamiltonian H_0 and therefore the two need to be treated on the same footing. Since the IR photon energy is not sufficient to ionize the bound electron, multiple IR photons needs to be absorbed for ionization to occur. For example, to ionize the ground state electron of a Helium atom, 16 photons of Ti:sapph laser (800nm) are needed. Therefore, several higher order terms in the expansion of the exact propagator in Equation 2.13 are needed. Although this can be done in principle, the resulting expression of the transition amplitude becomes cumbersome and hard to calculate. This problem is circumvented by using the intense-field many-body S-matrix theory (IMST) to obtain the strong-field transition amplitude [29].

The main goal of the SFA is to capture the physics of the intense-laser atom interaction as accurately as possible while keeping the expression of transition amplitude simple. The SFA is based on the assumption that the bound electron, owing to its proximity to the nucleus, does not feel the IR field, and can therefore be described using the eigenstates of the field-free atomic hamiltonian (H_0). The ionized electron, on the other hand, does not feel the coulomb field of the nucleus and behaves like a free electron in an IR field and is therefore described by Volkov states [13].

In this section, we will first describe the Volkov state. Then we will derive the transition amplitude for interaction between strong IR field and atom. Finally, the photoelectron distribution due to the interaction of an atom with a superposition of EUV and IR field will be derived.

2.4.1 SFA based on Volkov states

A Volkov state is the eigenstate of a free electron in a sinusoidal electric field. It is of the form

$$\psi^V_{k+A(t)}(\mathbf{r},t) = e^{i\left((\mathbf{k}+\mathbf{A}(t))\mathbf{r}-f(k,t)\right)} \tag{2.37}$$

Here $A(t)$ is the sinusoidal vector potential and $f(k,t)$ is the quantum phase obtained by integrating the kinetic energy:

$$f(k,t) = \frac{1}{2}\int^{t} dt''(\mathbf{k}+\mathbf{A}(t''))^2 \tag{2.38}$$

If $A(t) = 0$, the Volkov state reduces to a plane wave $e^{i(k\mathbf{r}-\omega t)}$ ($\omega = \frac{k^2}{2}$). Time evolution of the a Volkov state is given by

$$U_V(t,t')|\psi^V_{k+A(t')}(t')\rangle = e^{-i\int_{t'}^{t} dt'' H_V(t'')}|\psi^V_{k+A(t)}(t)\rangle \tag{2.39}$$

where

$$H_V(t'') = \frac{(\mathbf{k}+\mathbf{A}(t''))^2}{2}) \tag{2.40}$$

is the Volkov hamiltonian. Since the Volkov state is the eigenstate of Equation 2.40, we get

$$U_V(t,t')|\psi^V_{k+A(t')}(t')\rangle = e^{\frac{-i}{2}\int_{t'}^{t} dt'(\mathbf{k}+\mathbf{A}(t''))^2}|\psi^V_{k+A(t)}(t)\rangle \tag{2.41}$$

Interaction of an atom with strong IR pulse

We begin by writing Equation 2.5 in the velocity gauge:

$$H(t) = \frac{(\mathbf{k}+\mathbf{A}(t))^2}{2}) + V(\mathbf{r}) \tag{2.42}$$

Since the interaction term is being treated on the same footing as the field free part, Equation 2.42 can be partioned in two ways. The initial partition:

$$H^i(t) = H^i_0 + H^i_I(t) \tag{2.43}$$

where

$$H^i_0 = \frac{\mathbf{k}^2}{2} + V(\mathbf{r}) \tag{2.44a}$$

$$H^i_I(t) = \mathbf{k}\cdot\mathbf{A(t)} + \frac{\mathbf{A(t)}^2}{2} \tag{2.44b}$$

and the final partition

$$H_0^f = \frac{(\mathbf{k} + \mathbf{A(t)})^2}{2} \tag{2.45a}$$

$$H_I^f(t) = V(\mathbf{r}) \tag{2.45b}$$

The exact time propagation operator can be expressed for both the partitions:

$$U^i(t, t_0) = U_0^i(t, t_0) - i \int_{t_0}^{t} U^i(t, t') H_I^i(t') U_0^i(t', t_0) dt' \tag{2.46a}$$

$$U^f(t, t_0) = U_0^f(t, t_0) - i \int_{t_0}^{t} U^f(t, t') H_I^f(t') U_0^f(t', t_0) dt' \tag{2.46b}$$

Since $U^i(t, t_0)$ and $U^f(t, t_0)$ are equivalent, the expression of $U^i(t, t')$ can be replaced by $U^f(t, t')$. By inserting Equation 2.46b in Equation 2.46a, we get

$$U^i(t, t_0) = U_0^i(t, t_0) - i \int_{t0}^{t} U_0^f(t, t') H_I^i(t') U_0^i(t', t_0) dt' + \text{higher order terms} \tag{2.47}$$

Note that H_0^f is the Volkov hamiltonian $H_V(t)$ (therefore $U_0^f = U_V$). Neglecting the higher order terms and by dropping the superscript i, we get the expression of the SFA propagator:

$$U^{SFA}(t, t_0) = U_0(t, t_0) - i \int_{t_0}^{t} U_V(t, t') H_I(t') U_0(t', t_0) dt' \tag{2.48}$$

The SFA transition amplitude (from the bound ground state to a free Volkov state) is obtained by:

$$a^{SFA} = \langle \psi_k^V(t) | U^{SFA}(t, t_0) | \psi_g(t_0) \rangle \tag{2.49}$$

Using the Volkov propagator relation in Equation 2.41 and assuming that the ground state is orthogonal to the Volkov state, i.e., $\langle \psi_k^V(t) | U_0(t, t_0) | \psi_g(t) \rangle \approx 0$, the SFA

transition amplitude becomes

$$a^{SFA} = -i \int_{t_0}^{t} dt' e^{-iS(k,t,t')} \langle \psi^V_{k+A(t')} | H^i_I(t') | \psi_g \rangle. \tag{2.50}$$

The action term in the exponential is

$$S(k,t,t') = \int_{t'}^{t} dt'' \frac{(\mathbf{k} + \mathbf{A}(t''))^2}{2} - I_p(t - t'). \tag{2.51}$$

SFA amplitude in Equation 2.50 has a physical description: the electron sits in the ground state from the beginning of the interaction to t'; at t' the intense-laser causes the transition from the ground state to the Volkov state $\psi^V_k(t')$; then the electron evolves as as a free-electron in a sinusoidal field. The total quantum phase accumulated during the process is given by the action term.

Interaction of an atom with a superposition of EUV and IR fields

Interaction between an atom and a superposition of EUV and moderately strong IR pulse ($10^{10} - 10^{12}$W/cm^2) can be also be described using the SFA-Volkov formalism. Unlike the last section - where the IR is intense enough to ionized the bound electron through multiphoton absorption - moderately strong IR fields cannot ionized the bound electrons. The electron ionizes from the ground state to a Volkov by one EUV photon absorption.

Derivation of the formalism of interaction of an atom with a superposition of EUV and IR pulse is similar to the derivation of the formalism in the last section. We make one additional approximation: neglect the IR field in the calculation of the transition matrix element ($\langle \psi^V_k | H^i_I(t') | \psi_g \rangle$ in Equation 2.50) and neglect the EUV pulse in the propagation of the electron after ionization i.e. in the calculation of the action term (shown in Equation 2.51). Therefore, the transition amplitude in the length gauge is given by:

$$a^{SFA} = -i \int_{t_0}^{t} dt' e^{-iS(k,t,t')} \langle \psi^V_{k+A(t')} | E_X(t' - \tau) z | \psi_g \rangle. \tag{2.52}$$

The action term is the same as in Equation 2.51. Here $E_X(t)$ is the EUV electric field and $A(t)$ (in Equation 2.51) is due to the IR field only. The EUV pulse is delayed by τ with respect to the IR field - the reason for doing so will become clear in Chapter 5. Since the EUV pulse is of finite duration, we can set $t_0 \to -\infty$ and $t \to \infty$. Then the probability distribution (square of the SFA transition amplitude) of photoelectrons is given by

$$P(k,\tau) = \left| \int_{-\infty}^{\infty} dt' e^{-iS(k,t,t')} d^V_{\mathbf{k}+\mathbf{A}(t')} E_X(t'-\tau) \right|^2 . \tag{2.53}$$

The Volkov dipole transtion matrix element is given by:

$$d^V_{\mathbf{k}+\mathbf{A}(t')} = \langle \psi^V_k | z | \psi_g \rangle \tag{2.54}$$

2.4.2 SFA based on Coulomb Volkov states

Thus far, we have seen two descriptions of laser-atom interaction. In the first, perturbation theory was used to calculate the transition amplitude for one photon ionization where the initial and the final states are atomic eigenstates. This formalism accurately describes the ionization process where the external perturbation is weak. The second description, based on SFA, is suitable for treating laser-atom interaction where the external perturbation is comparable to the unperturbed hamiltonian. This formalism results in a simplified expression of the transition amplitude. However, as we will see in Chapter 4 and Chapter 5, ignoring the effect of the atomic potential on the continuum states does not accurately capture the physics of the laser-atom interaction. This is evident due to the fact that Volkov based SFA is unable to predict experimentally observed phenomena such as the cooper minimum [4]

The main challenge in describing the interaction of the an atom with a strong external perturbation is the choice of the basis states. If the exact propagation operator (Equation 2.13) were used, any choice of complete basis states would be equally valid. However, since the series expansion of the propagator is terminated to a few terms, the choice of basis state becomes important.

For instance, in the perturbation theory, it is assumed that the initial and the final states are the eigenstates of the unperturbed hamiltonian. The underlying assumption is that the external perturbation does not change the final states. In the SFA, the initial state is described by atomic eigenstate, whereas the final state is described by a Volkov state. In this case, the assumption is that due to strong external perturbation, the effect of the atomic potential on the external state can be neglected.

It turns out that another set of basis states, called Coulomb-Volkov (CV) states, are better suited to describe the electron in the continuum. It was first used to describe the compton scattering of an electron from an atom in the presence of an IR field [30]. As it will be shown in Chapter 4, CV states based SFA can predict the cooper minimum in the high-order harmonic spectrum of argon and krypton. The CV state is a product of the spatial part of the scattering eigenstate of the atom and the temporal part of the Volkov state:

$$\psi^{CV}_{k+A(t')}(\mathbf{r},t) = \psi^{sc}_{k}(\mathbf{r})e^{-if(k,t).} \tag{2.55}$$

Coulomb-Volkov state can be easily introduced into the SFA formalism developed in the last section. For instance, the CV based SFA can be used to calculate the photoelectron distribution calculated in the last section. Equation 2.53 becomes

$$P(k,\tau) = \left| \int_{-\infty}^{\infty} dt' e^{-iS(k,t,t')} d^{CV}_{\mathbf{k}+\mathbf{A}(t')} E_X(t'-\tau) \right|^2. \tag{2.56}$$

The Coulomb-Volkov dipole transtion matrix element is given by

$$d^{CV}_{\mathbf{k}+\mathbf{A}(t')} = \langle \psi^{sc}_{k+A(t')} | z | \psi_g \rangle \tag{2.57}$$

2.5 Comparison between Volkov and Coulomb-Volkov dipole transition matrix element

In the previous section, CV-SFA and Volkov-SFA formalism were used to derive the expression of the photoelectron spectrum due to ionization by an EUV pulse in the

presence of an IR field (Equation 2.53 and Equation 2.56). The difference between the two formalism lies in the choice of the dipole transition matrix element (Equation 2.54 and Equation 2.57). The SFA formalism can also be used to model the recombination of an electron with an atom - the process which leads to the emission of a photon - in the presence of an IR field. The dipole transition matrix element of the recombination process is the complex conjugate of the dipole transition matrix element of the ionization process.

The calculation of the dipole transition matrix element of ionization and recombination is governed by the dipole transition rule ($\Delta l = \pm 1$ and $\Delta m = 0$). For example, after absorption of one photon, the electron in the bound p orbital, will make a transition to either s or d orbital in the continuum (See Figure 2-1). Vice-versa is true in the recombination process. The two ionization (recombination) paths interfere. At energies at which the two paths destructively interfere, a minimum in the photoionization cross section (recombination cross section in high-order harmonic spectrum) is observed.

Next, the CV dipole transition matrix elements and Volkov dipole matrix elements are numerically calculated and compared. One important difference between the two matrix elements is that unlike the Volkov dipole transition matrix element, the CV dipole matrix element is complex. As a result, as we will see in detail in Chapter 5, the phase of the ionized photoelectron pulse is different from the EUV pulse. Therefore, it is important to calculate not only the absolute value of the dipole transition matrix element but also its phase. The absolute value of the coulomb-Volkov and the Volkov transition matrix element for neon, argon and krypton are plotted in Figures 2-2 - 2-4

The dipole transition matrix element also depends on the polar angle (Ω_k in expansion of the continuum eigenstate as shown in the Equation 2.31) with respect to the polarization axis. In the photoionization process, the polar angle determines the angle at which the photoelectrons are observed. Experimentally, this angle is determined by the positioning of the time of flight spectrometer with respect to the polarization axis of the EUV and IR pulse. In reality, the time of flight spectrom-

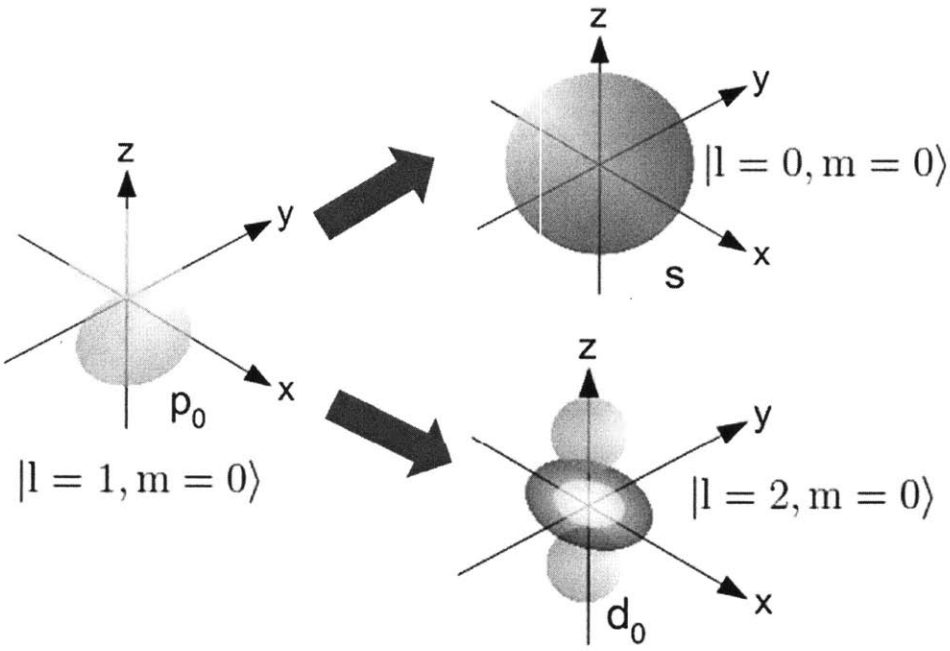

Figure 2-1: Cooper minimum: According to dipole transition rule ($\Delta l = \pm 1$), an electron from the bound p-orbital can only make a transition to a s- or d-orbitals. The two channels can destructively interfere to lead to a minimum

eter cannot resolve photoelectrons emited from one particular solid angle. Rather, photoelectrons emited over a range of solid angles, known as the acceptance angle of the time of flight spectrometer, are observed. Therefore, it is important to study the dependence of the dipole transition matrix element on the polar angle (Figure 2-5 - 2-10). In order to calculate the Volkov transition matrix element, the Volkov state which is a plane wave, can be expanded in the spherical coordinate system (like the scattering state in Equation 2.31). The *momentum normalized* plane wave is

$$\frac{1}{(2\pi)^{\frac{3}{2}}} e^{ikz} = \frac{1}{k} \sum_{l=0}^{\infty} \sum_{m=-l}^{m=l} i^l \frac{u_{kl}^{pl}(r)}{r} Y_{lm}(\Omega_r) Y_{lm}^*(\Omega_k). \tag{2.58}$$

The radial wavefunction is given by

$$u_{kl}^{pl} = (kr)j_l(kr) \tag{2.59}$$

where $j_l(kr)$ is the spherical bessel function. The Volkov transition matrix element can be calculated the same way as shown in Equations 2.23 -2.26.

The absolute values of the CV and Volkov dipole transition matrix element of neon, argon and krypton have been plotted in Figures 2-2 - 2-4. Ω_k has been set to zero. The minimum in the dipole matrix element can be observed. More importantly, the position for the minima depends on the choice of the matrix element. Close to the minima, the absolute values of the two matrix elements are very different. The CV dipole transition matrix elements act like low pass filters: the bound electrons have a higher probability of ionization at low energies than at high energies.

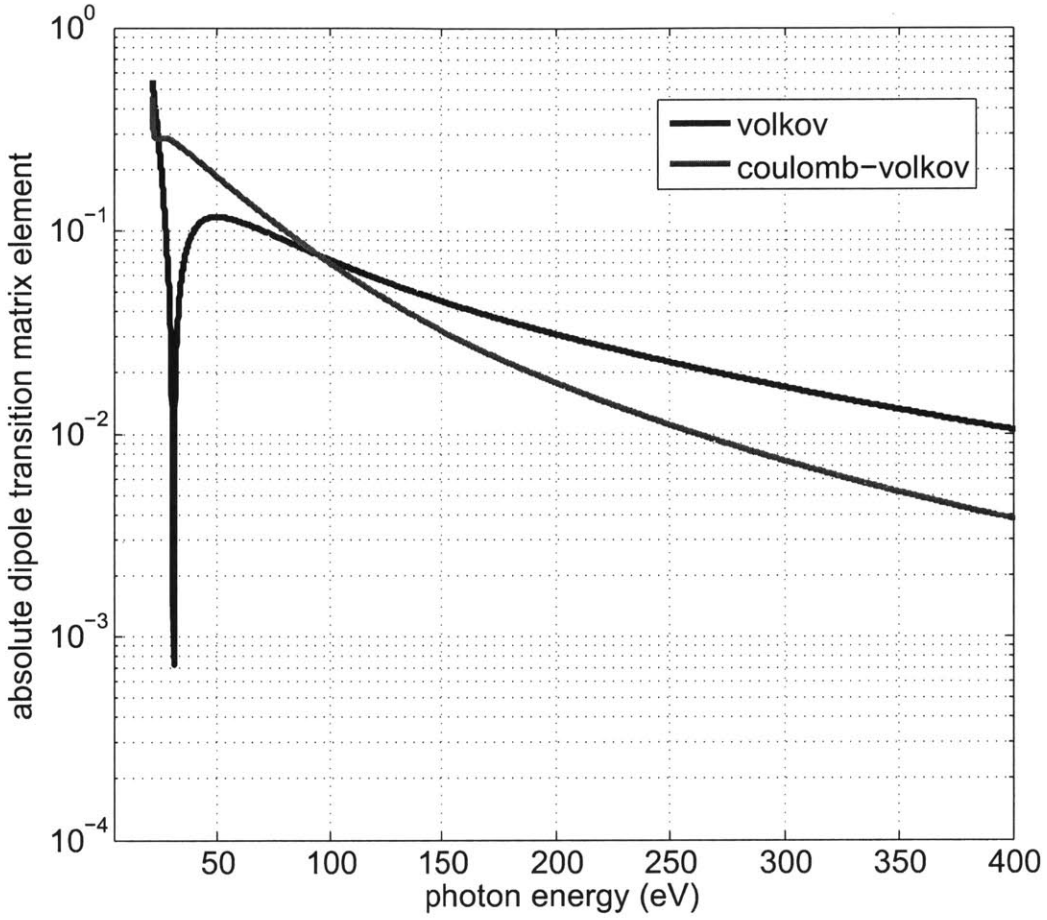

Figure 2-2: Comparison between Volkov and coulomb-Volkov dipole transition matrix elements for neon

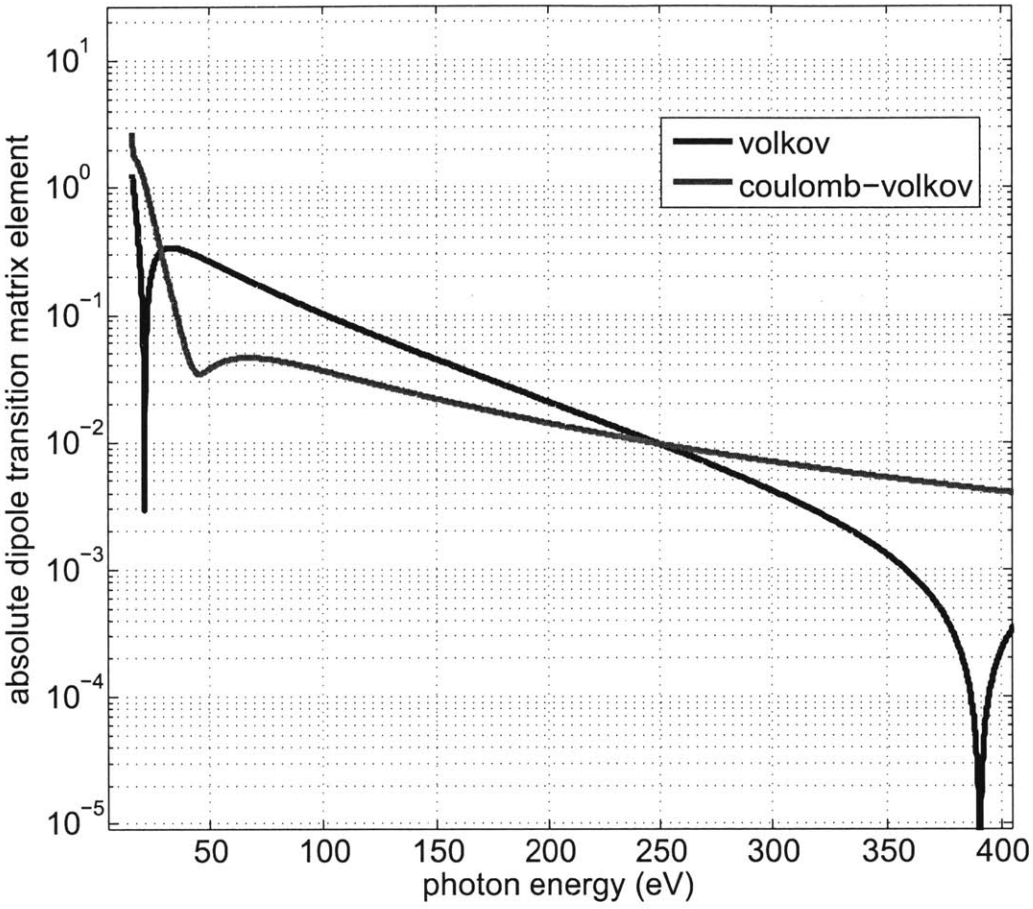

Figure 2-3: Comparison between Volkov and coulomb-Volkov dipole transition matrix elements for argon

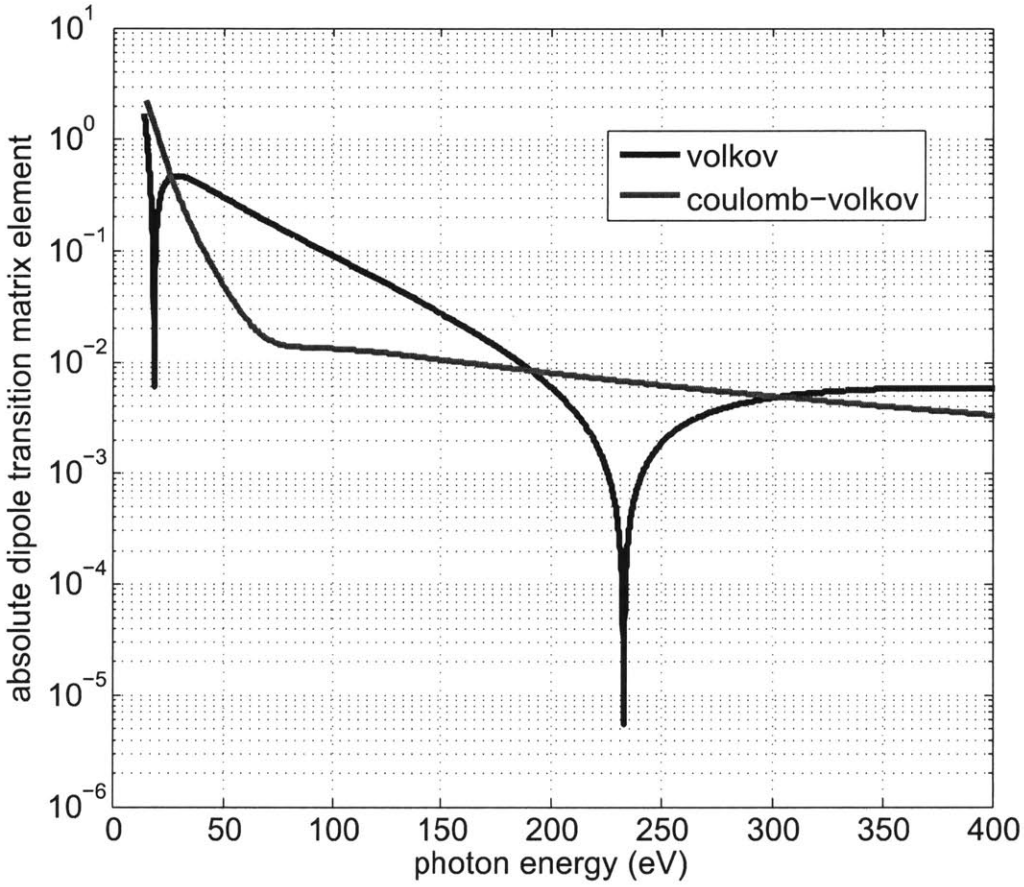

Figure 2-4: Comparison between Volkov and Coulomb-Volkov dipole transition matrix elements for krypton

Next, the angle dependence of the both the absolute value and the phase of the Coulomb-Volkov dipole transition matrix are plotted for neon (Figures 2-5 and Figure 2-6) argon (Figures 2-7 and Figure 2-8) and krypton (Figures 2-9 and Figure 2-10). The CV dipole transition matrix element is sensitive to the polar angle. This shows, than in experiments where photoelectron spectrum is measured using a time of flight spectrometer, it is important to ensure that the acceptance angle is well known. Additionally, as the acceptance angle increases, $|l = 1, m = 1\rangle$ and $|l = 1, m = -1\rangle$ bound orbitals can also participate in the ionization process.

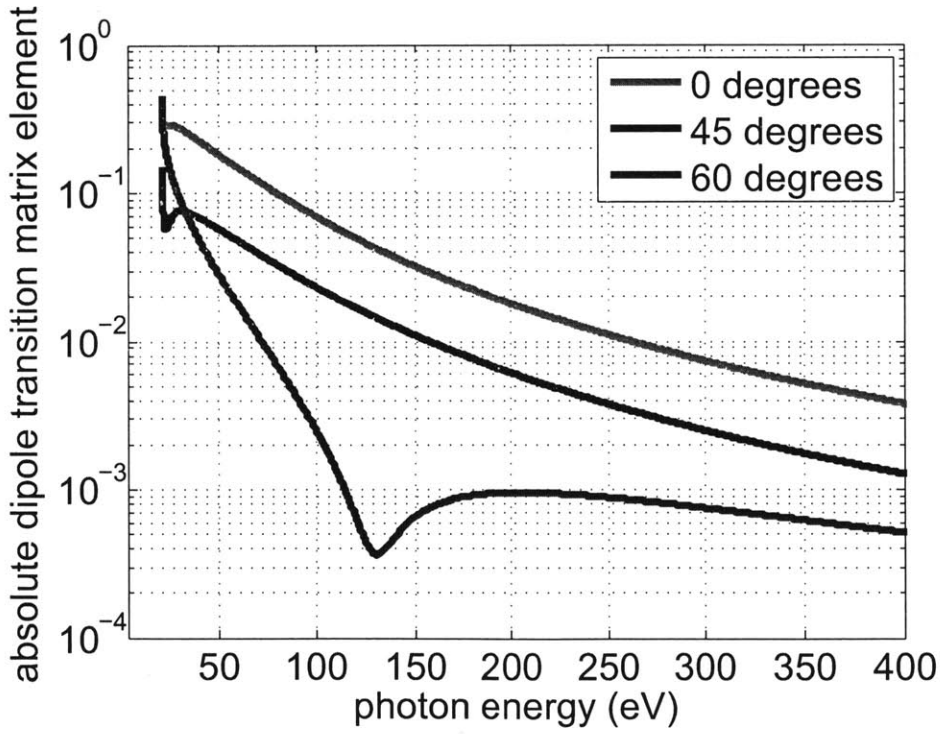

Figure 2-5: The absolute value of the CV dipole transition matrix element of neon at three polar angles. At 120eV, the curve for 60 degrees has a sharp minimum

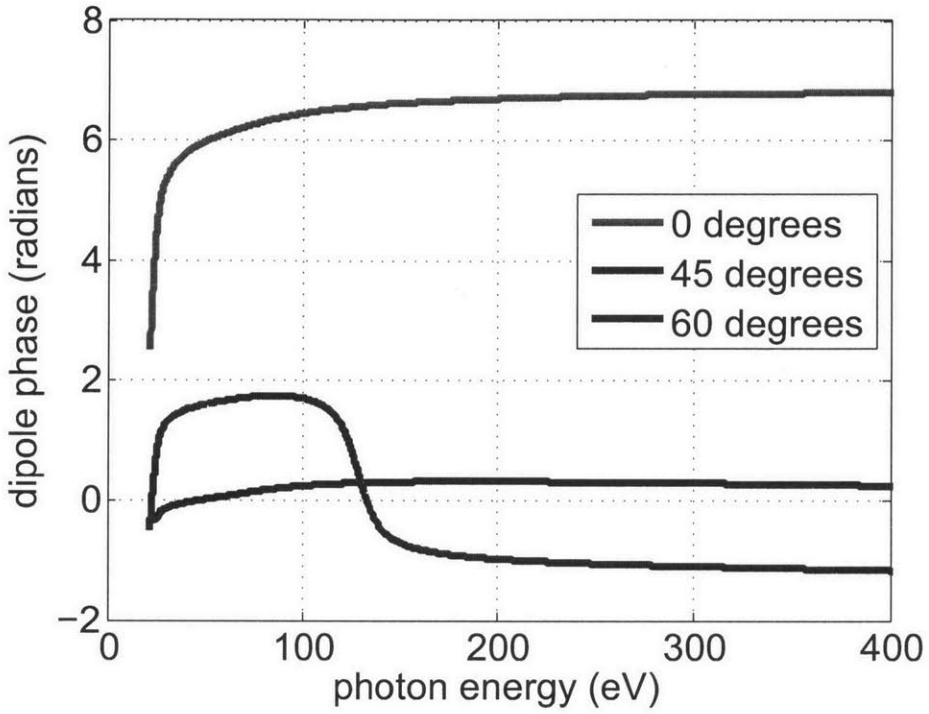

Figure 2-6: The phase of the CV dipole transition matrix element of neon is plotted for three polar angles

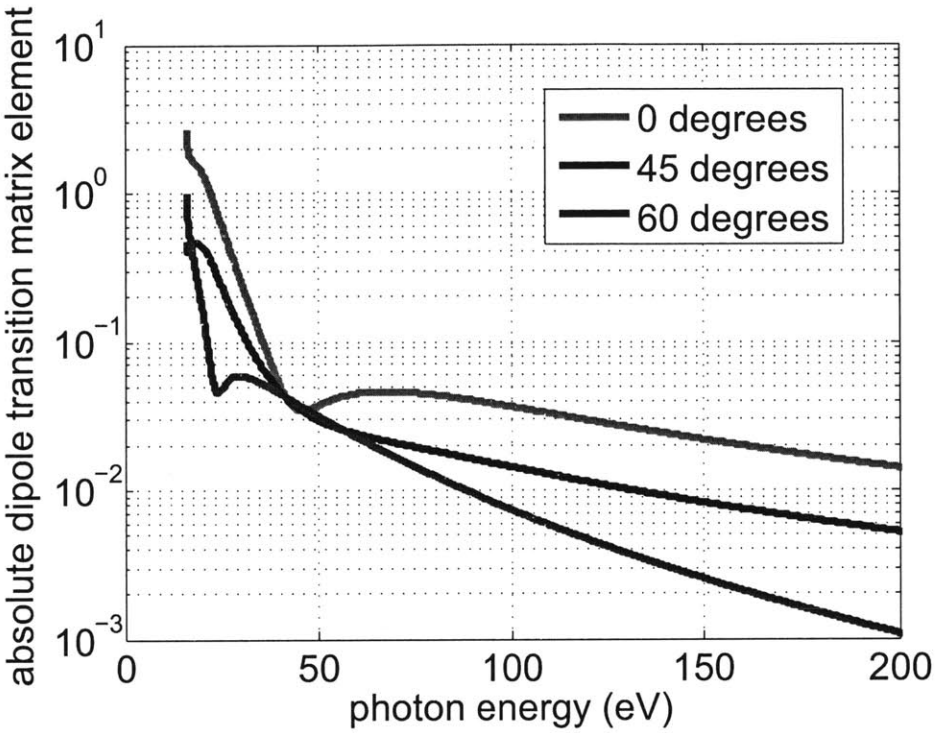

Figure 2-7: The absolute value of the CV dipole transition matrix element of argon at three polar angles

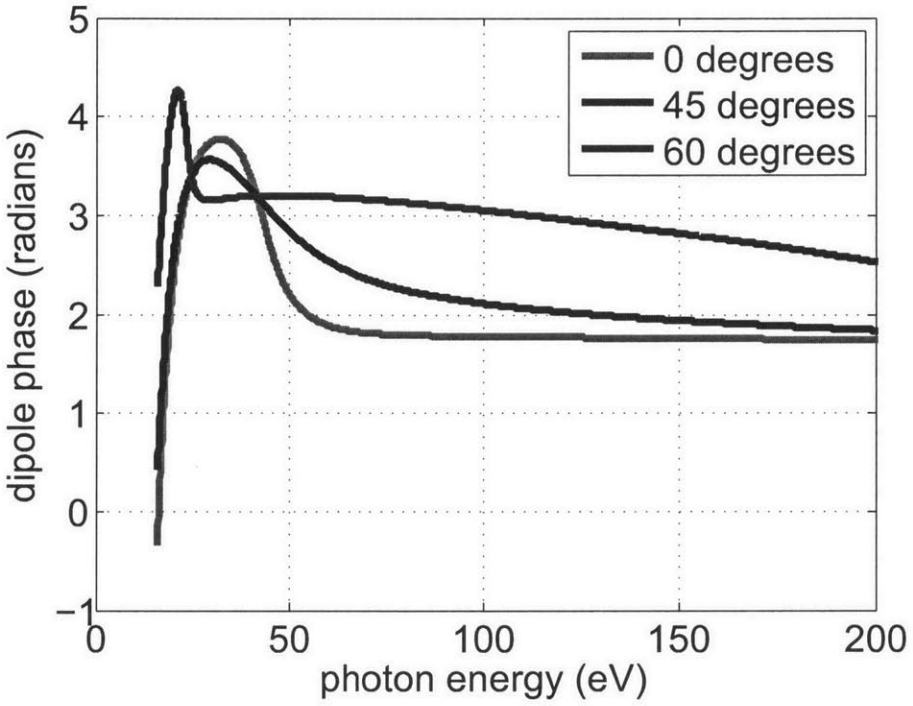

Figure 2-8: The phase of the CV dipole transition matrix element of argon is plotted for three polar angles

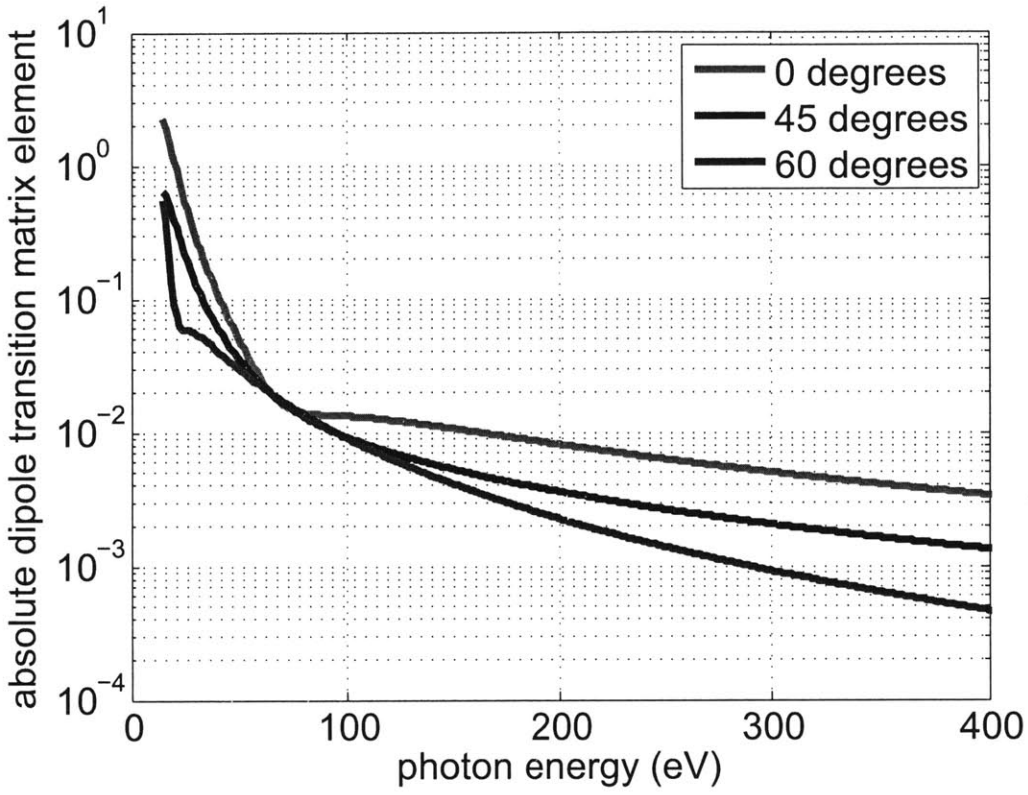

Figure 2-9: The absolute value of the CV dipole transition matrix element of neon at three polar angles.

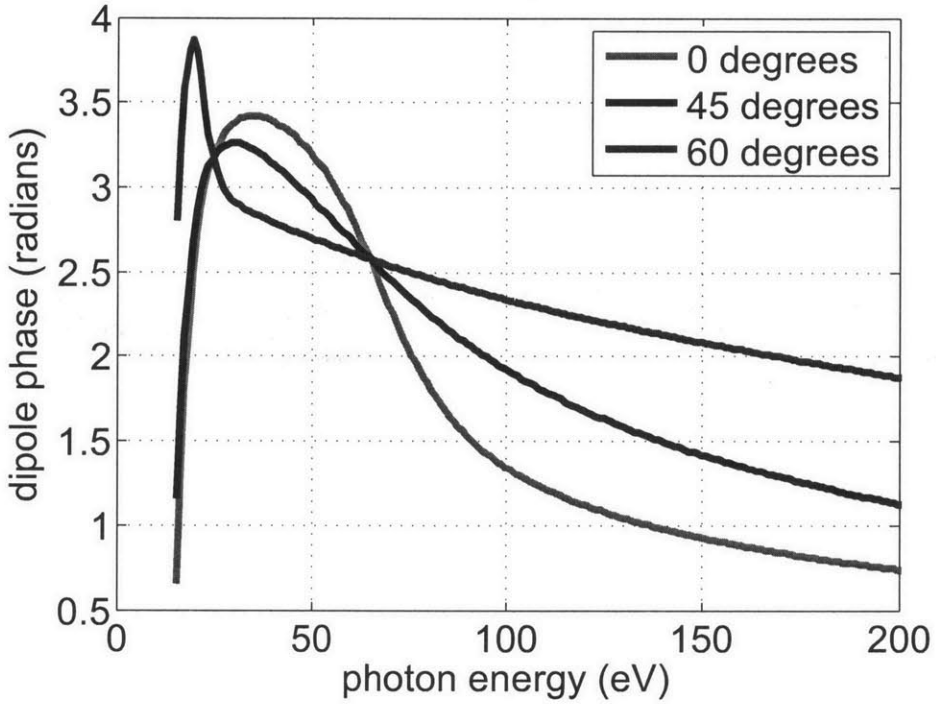

Figure 2-10: The phase of the CV dipole transition matrix element of krypton is plotted for three polar angles

Chapter 3

Modeling the single atom response

When an atom is placed in an intense IR pulse, the oscillating electric field of the latter perturbs the electron cloud. As a result of the perturbation, the atom acts like an antenna and radiates high-order harmonics. The goal of modeling the quantum mechanical interaction between the laser and the atom, referred to as the single atom response, is to calculate the atomic dipole acceleration term. The atomic dipole acceleration acts like the source term in the maxwell's equation

In this chapter, two techniques for calculating dipole acceleration, the semi-classical three step model and the numerical time dependent Schrödinger equation, will be presented. Then the ionization models used in the TSM will be compared with the ionization rates calculated from TDSE. The effect of the ionization models on the HHG spectrum will be studied. Finally, the TDSE and the TSM will be used to explore generation of isolated attosecond pulses by non-sinusoidal sub-cycle pulses.

3.1 Three Step Model

As the name suggests, the dynamics of an atom in a laser field that produces high harmonic generation can be divided into three distinct steps namely ionization of a single electron, its propagation and recombination. This is illustrated in Figure 3-1. In step (a), the electric field (yellow line) alters the shape of the coulomb potential allowing the electron to tunnel through the barrier. In steps (b) and (c) the electron

travels classically in the continuum (neglecting the influence of the coulomb potential) and returns back to the atom when the electric field reverses directions. In step (d) the returning electron collides with the atom and may be scattered or absorbed. In the case of the latter, its kinetic energy is released as a burst of photon energy as shown in step (d). Next, each of the three steps of the TSM will be discussed

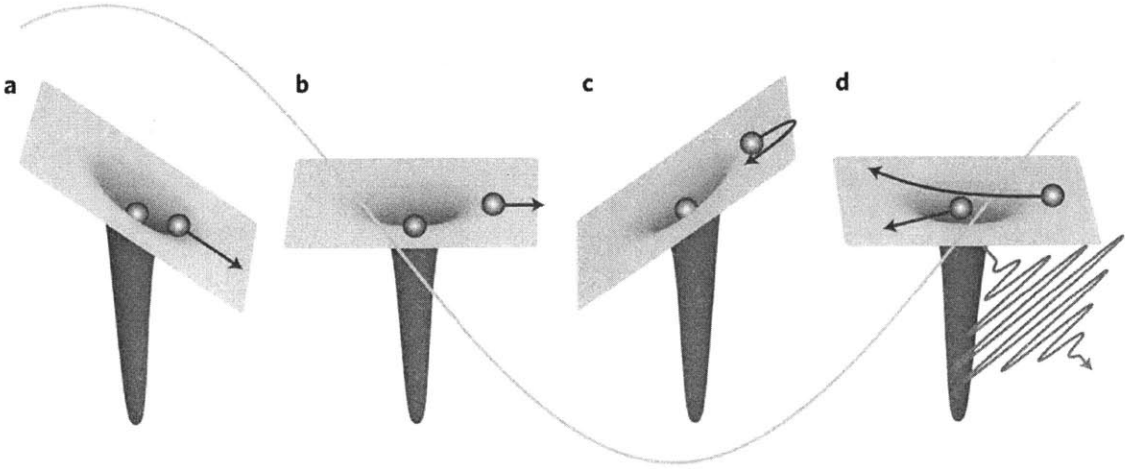

Figure 3-1: Cartoon of the three steps in the Three Step Model : (a) ionization; (b,c) propagation and (d) recombination. This Figure is taken from [1]

3.1.1 Ionization

A sinusoidal electric field with amplitude E and frequency ω can ionize an atom with ionization potential I_p . It is assumed that only a single electron of the atom is ionized while the rest of the electrons are frozen in the orbitals. This is often referred to as the Single Active Electron Approximation (SAEA). The laser field is time dependent and we can define an adiabaticity parameter called the Keldysh Parameter:

$$\gamma = \frac{\omega\sqrt{2I_p}}{E} \tag{3.1}$$

Depending upon the value of γ , ionization can either be in the tunneling regime $\gamma << 1$ or in the multiphoton regime $\gamma > 1$. In the tunneling regime, the electric field is high and the frequency of the laser is small. The electron ionizes by tunneling under the coulomb barrier. Multiphoton ionization occurs for small laser fields with

high frequency. In this case, the electron absorbs many photons and gains enough energy to overcome the ionization potential. The two limits of γ determine which ionization process is dominant. In reality, both of the ionization processes can co-exist for intermediate values of γ . If the electric field is so high that it completely suppresses the coulomb barrier allowing the electron to fly out of the atom, we refer to it as the Barrier Suppression regime.

Ionization of an atom in the presence of a laser field has been intensively studied [31, 32, 33] . The simplest case of ionization of an s orbital of a Hydrogen atom in the presence of a static field was solved using the WKB method [34]. This corresponds to $\gamma = 0$, and therefore the channel of ionization is purely tunneling. Later this idea was extended to an arbitrary orbital of Hydrogen with effective principal quantum number $n^* = Z/\sqrt{(2I_p)}$, azimuthal quantum number l and magnetic quantum number m for linearly polarized light[13] The ionization rate is

$$w(t) = A_{n^*,l} B_{l,|m|} I_p \left(- \frac{2(2I_p)^{3/2}}{3|E|} \right)^{2n^* - |m| - 1} exp\left(- \frac{2(2I_p)^{3/2}}{3|E|} \right) \tag{3.2}$$

where

$$A_{n^*,l} = \frac{2^{2n^*}}{n^* \Gamma(n^* + l + 1) \Gamma(n^* - l)} \tag{3.3}$$

and

$$B_{l,|m|} = \frac{(2l+1)(l+|m|)!}{2^{|m|}|m|!(l-|m|)!} \tag{3.4}$$

In literature, it is commonly referred to as the ADK theory. E is the electric field. The time dependent ionization rate can be found by replacing $E \rightarrow E_0 \cos(\omega t)$. This is valid as long as $\omega << I_p$, i.e the ground state wavefunction can adjust itself adiabatically to the laser field perturbation. The WKB method used to derive Equation 3.2, implies that the electron emerges with a zero velocity after tunneling.

The two limits of γ only tell us which of the two ionization regimes dominate. In reality, multiphoton ionization and tunneling ionization co-exist. Therefore, the ADK ionization rate will give smaller ionization rates even in intermediate values of γ . Another method to calculate the ionization rate has been shown using the

Landau-Dykhne method [35, 36]. Detailed discussion on Landau-Dykhne method can be found in [37]. This method is valid in the adiabatic regime and can account for multiphoton ionization and referred to as Nonadiabatic tunnel ionization [36]. The non-adiabatic ionization rate is given by

$$w(t) = N(t)exp\Big(- \frac{E_0^2}{\omega^3}\Phi(\gamma, \theta(t))\Big) \tag{3.5}$$

where the phase dependence is given by

$$\Phi(\gamma, \theta) = (\gamma^2 + \sin^2\theta + \frac{1}{2})\ln c - \frac{3\sqrt{b-a}}{2\sqrt{2}}\sin|\theta| - \frac{\sqrt{b+a}}{2\sqrt{2}\gamma} \tag{3.6a}$$

$$a = 1 + \gamma^2 - \sin^2\theta \tag{3.6b}$$

$$b = \sqrt{a^2 + 4\gamma^2\sin^2\theta} \tag{3.6c}$$

$$c = \sqrt{\Big(\sqrt{\frac{b+a}{2}} + \gamma\Big)^2 + \Big(\sqrt{\frac{b-a}{2}} + \sin|\theta|\Big)^2} \tag{3.6d}$$

and the prefactor is given by

$$N(t) = A_{n^*l}B_{l,|m|}\Big(\frac{3\kappa}{\gamma^3}\Big)^{1/2} C I_p\Big(- \frac{2(2I_p)^{3/2}}{3|E|}\Big)^{2n^* - |m| - 1} \tag{3.7a}$$

$$\kappa = \ln(\gamma + \sqrt{\gamma^2 + 1}) - \frac{\gamma}{\sqrt{\gamma^2 + 1}} \tag{3.7b}$$

$$C = (1 + \gamma^2)^{(|m|/2 + 3/4)} + A_m(\omega, \gamma) \tag{3.7c}$$

C is the correction to the quasistatic limit $\gamma << 1$ of the preexponential term [31, 32, 33]. The main difference between Equation 3.2 and Equation 3.5 is due to the difference in the exponential term.

3.1.2 Propagation

Once the electron appears in the continuum, it is accelerated by the sinusoidal laser field. We assume that the field is so strong that we can neglect the influence of the coulomb potential. This is called Strong Field Approximation (SFA). A free electron placed in a sinusoidal electric field obtains a time average kinetic energy called the ponderomotive energy. It is defined as

$$U_p = \frac{E^2}{4\omega^2} \tag{3.8}$$

According to the ADK theory of ionization, the electron appears in the continuum with zero velocity. We then treat the motion of the electron in the laser field classically. Depending on the phase of the laser field at which the electron appears in the continuum, it may or may not return back to the atom. This is shown in the Figure 3-2.

As we can see in Figure 3-2, some of the trajectories never return back to the atom. The cyan line represents the trajectory that returns back with the maximum kinetic energy. This corresponds to the highest harmonic also known as the cut-off

$$\omega_{max} = I_p + 3.17U_p \tag{3.9}$$

Those trajectories, which are born after but return back before the most energetic trajectory, are short trajectories. Those, that are born before but return back before the most energetic trajectory are called long trajectories.

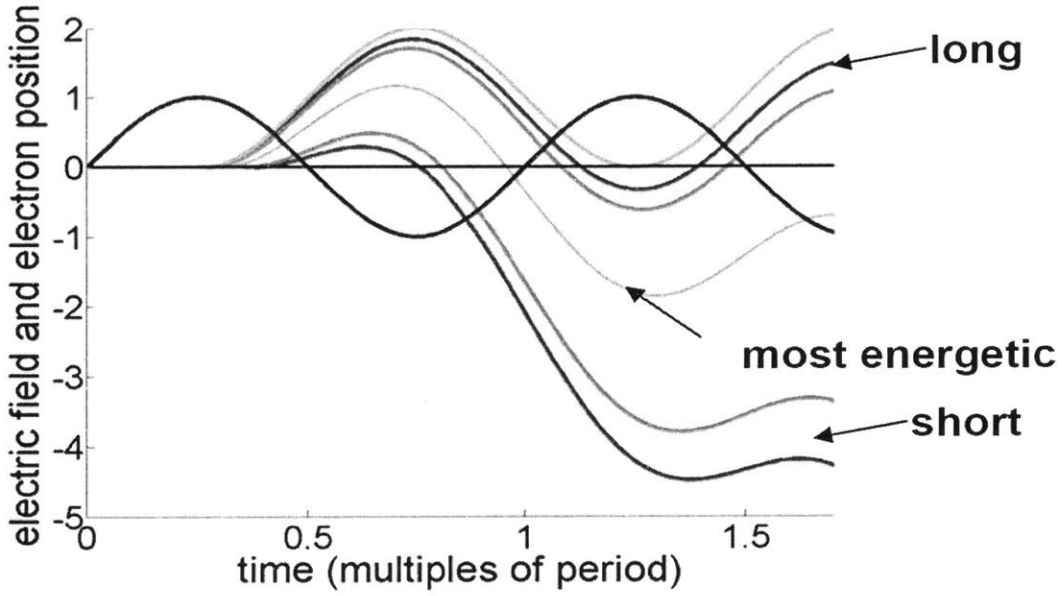

Figure 3-2: Plot of the electron trajectories. A 800 nm driver field (blue sinusoid) ionizes the electron which follow classical trajectories after birth. The most energetic trajectory (cyan) determines the cut off of the HHG spectrum. A pair of trajectories, short and long, return back with the same energy.

Figure 3-3 show the ratio of kinetic energy and ponderomotive energy at the time of return as a function of birth phase with respect to the laser field (dashed line). Except at the cut-off, one can find a pair of trajectories, long and short, that return back with the same energy. However, they have a different phase and therefore one can observe interference at harmonic away from the cut-off.

3.1.3 Recombination

The returning electron can recombine with the parent atom. The difference between the kinetic energy of return and the energy of the final state is emitted as a photon. The recombination step will be discussed in detail in Chapter 4.

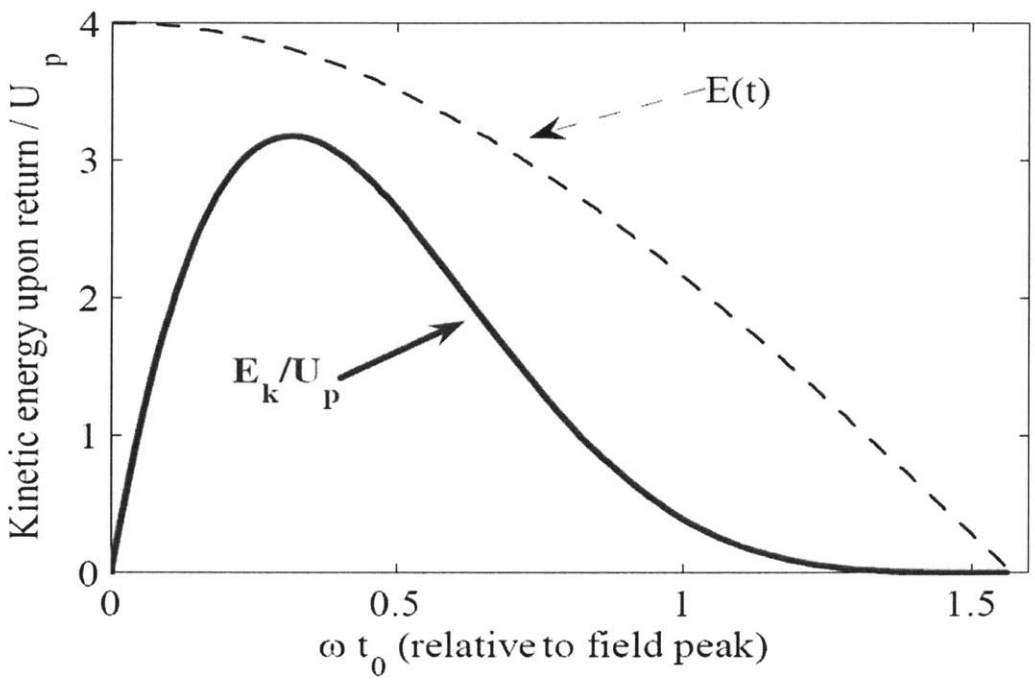

Figure 3-3: Ratio of the kinetic energy of return and the ponderomotive energy (solid red) has been plotted against the phase of the electric field (blue dashed). The most energetic trajectory is born about 0.38 radian after the peak of the electric field

3.1.4 Derivation of the three step model

The single electron wavefunction can be divided into the ground state and the continuum state:

$$|\psi(t)\rangle = a_g(t)e^{-iI_p t}|g\rangle + |\varphi(t)\rangle \tag{3.10}$$

Here, $|a_g(t)|^2$ is the groundstate population that decays due to ionization. It can be calculate by using the ionization models presented in Equation 3.2 and Equation 3.5.The part of the wavefunction in the continuum state can be written as a superposition of volkov states:

$$|\varphi(t)\rangle = \int a_k(t)|k + A(t)\rangle \tag{3.11}$$

By applying the volkov propagator on the ground state, the expression of the continuum state becomes:

$$|\varphi(t)\rangle = -i \int_0^t dt' U_V(t,t') E(t') z a_g(t') e^{-iI_p t'} |g\rangle \tag{3.12}$$

The amplitude of each volkov state can be calculating by projecting the continuum state on the corresponding volkov state: $a_k(t) = \langle k+A(t)|\varphi(t)\rangle$. As a result, Equation 3.12 becomes

$$a_k(t) = -i \int_0^t dt' e^{-iS(k,t,t')} E(t') a_g(t') \langle k + A(t')|z|g\rangle \tag{3.13}$$

Equation 3.12 can be thought of in terms of Feynman paths. At the time t' the ground state makes a transition to the vokov state $|k + A(t')\rangle$ due to the electric field $E(t')$. Once in the volkov state, the electron evolves like a free electron in an electric field (SFA). Since the interaction can take place at all times, one needs to integrate over all the interaction times t' (also referred to as birth time). The quantum mechanical phase is given by the action term $S(k,t,t')$

$$S(k,t,t') = \int_{t'}^t dt'' \frac{(k_z + A(t''))^2}{2} + \frac{\eta^2}{2}(t - t') \tag{3.14}$$

where $\eta = \sqrt{2I_p + k_\perp^2}$ and the momentum can be separated into a part parallel to the electric field and a part perpendicular to it ($k^2 = k_z^2 + k_\perp^2$).

Due to fast oscillating action term, Equation 3.13 can be solved by integrating around the saddle point t_{sp} where the first derivative of the action is zero. The action term (Equation 3.14) can be expanded around the saddle point:

$$S(k,t,t') \approx S(k,t,t_{sp}) + \left.\frac{\partial^2 S}{\partial t'^2}\right|_{t_{sp}} (t' - t_{sp})^2 \tag{3.15}$$

The saddle point is calculated by

$$\left.\frac{\partial S}{\partial t'}\right|_{t_{sp}} = -\frac{(k + A(t_{sp}))^2}{2} - I_p = 0 \tag{3.16}$$

which gives

$$k_z + A(t_{sp}) = -i\eta \tag{3.17}$$

The next step is to expand Equation 3.17 around the real part (t^r_{sp}) of the saddle point ($t_{sp} = t^r_{sp} + it^i_{sp}$). By fourier expansion to the first order term, Equation 3.17 becomes:

$$k_z + A(t^r_{sp}) - iE(t^r_{sp})(t^i_{sp}) = -i\eta \tag{3.18}$$

The real and the imaginary part of Equation 3.18

$$k_z + A(t^r_{sp}) \approx 0 \tag{3.19a}$$

$$t^i_{sp} \approx \frac{\eta}{E(t^r_{sp})} \tag{3.19b}$$

Equation 3.19a means that the velocity of the ionized electron in the direction of laser polarization at the time of birth is zero. Next, each term in the right hand side of Equation 3.15 can be expanded around t^r_{sp}. The expansion of the zeroth order term is:

$$S(k,t,t_{sp}) = S(k,t,t^r_{sp}) + \left.\frac{\partial S}{\partial t_{sp}}\right|_{t^r_{sp}} (it^i_{sp}) + \frac{1}{2!}\left.\frac{\partial^2 S}{\partial t^2_{sp}}\right|_{t^r_{sp}} (it^i_{sp})^2 + \frac{1}{3!}\left.\frac{\partial^3 S}{\partial t^3_{sp}}\right|_{t^r_{sp}} (it^i_{sp})^3 \tag{3.20}$$

Due to Equation 3.19a, the first and the second order can be approximated to zero. Equation 3.20 then reduces to

$$S(k,t,t_{sp}) = \int_{t^r_{sp}}^{t} dt'' \frac{(k_z + A(t''))^2}{2} + \frac{\eta^2}{2}(t - t^r_{sp}) - i\frac{\eta^3}{3E(t^r_{sp})} \tag{3.21}$$

Expansion of the second order term in the right hand side of Equation 3.15 gives

$$\left.\frac{\partial^2 S}{\partial t'^2}\right|_{t_{sp}} (t' - t_{sp})^2 = -(k_z + A(t_{sp})E(t_{sp})(t' - t_{sp})^2 \tag{3.22}$$

which when expanded around the real time t_{sp}^r becomes

$$\left.\frac{\partial^2 S}{\partial t'^2}\right|_{t_{sp}} (t' - t_{sp})^2 \approx -i\frac{\eta}{E(t_{sp}^r)}\big(E(t_{sp}^r)(t' - t_{sp}^r) - i\eta\big) \tag{3.23}$$

Next, we handle the non-exponential prefactors of Equation 3.13. The dipole matrix element for $1s$ orbital of Hydrogen is given by

$$\langle k|z|g\rangle = -i\frac{2^{7/2}(2I_p)^{5/4}}{\pi}\frac{k_z}{\left(\eta^2 + k^2\right)^3} \tag{3.24}$$

Equation 3.24 is expanded around the real part of the saddle point t_{sp}^r. We get,

$$\langle k + A(t')|z|g\rangle \approx -i\frac{2^{7/2}(2I_p)^{5/4}}{\pi}\frac{k_z + A(t_{sp}^r) - E(t_{sp}^r)(t' - t_{sp}^r)}{\left(\eta^2 + \left(k_z + A(t_{sp}^r) - E(t_{sp})^r(t' - t_{sp}^r)\right)^2\right)^3} \tag{3.25}$$

Making the transformation $\theta = E(t_{sp})^r(t' - t_{sp}^r)$, and by using $k_z + A(t_{sp}^r) \approx 0$,

$$\begin{aligned} a_k(t) = &- i\int_0^t d\theta i\frac{2^{7/2}(2I_p)^{5/4}}{\pi}a_g(t_{sp}^r)\frac{\theta}{\left(\eta^2 + \theta^2\right)^3}\times \\ &exp\left(i\int_{t_{sp}^r}^t dt''\frac{(k_z + A(t''))^2}{2} + \frac{\eta^2}{2}(t - t_{sp}^r) - i\frac{\eta^3}{3E(t_{sp}^r)} - i\frac{\eta\big(\theta - i\eta\big)^2}{2E(t_{sp}^r)}\right) \end{aligned} \tag{3.26}$$

Evaluating the following integration using Cauchy integral theorem:

$$\int_{-\infty}^{\infty} d\theta\frac{\theta}{\left(\eta^2 + \theta^2\right)^3}exp\left(\frac{\eta\big(\theta - i\eta\big)^2}{2E(t_{sp}^r)}\right) = i\pi\frac{1}{8E(t_{sp}^r)\eta}, \tag{3.27}$$

Equation 3.26 is reduced to

$$a_k(t) = a(t_{sp}^r)\mathrm{f}(E,\eta)e^{-iS\left(k,t,t_{sp}^r\right)} \tag{3.28}$$

where

$$\mathrm{f}(E,\eta) = -i\frac{2^{1/2}(2I_p)^{5/4}}{|E(t_{sp}^r)|\eta}\exp\left(-\frac{\eta^{3/2}}{3|E(t_{sp}^r)|}\right) \tag{3.29}$$

By integrating Equation 3.29 over the perpendicular momenta, it can be expressed in terms of ADK ionization rates. The details of this derivation can be seen in Appendix B of [38].

$$\mathrm{f}(E, I_p) = -i\frac{(2I_p)^2}{|E(t^r_{sp}|}\sqrt{\frac{w(E(t^r_{sp}))}{\pi}} \tag{3.30}$$

Using $a_k(t)$, the continuum wavepacket in Equation 3.11 can be calculated. Next, the atomic dipole acceleration is calculated by either first calculating the dipole moment and then taking double derivative with respect to time or by directly calculating the dipole acceleration by using the Ehrenfest theorem:

$$\zeta(t) = a^*(t)\langle g|z|\varphi(t)\rangle \tag{3.31a}$$

$$\ddot{\zeta}(t) = a^*(t)\langle g| - \partial_z V(r)|\varphi(t)\rangle \tag{3.31b}$$

Here V is the atomic potential. The detail of calculating Equation 3.31a and Equation 3.31b, will be presented in detail in Chapter 4. To solve Equation 3.31b, we first expand it in the momentum basis,

$$\ddot{\zeta}(t) = a^*(t)\int d^3k\langle g| - \partial_z V(r)|k + A(t)\rangle\langle k + A(t)|\varphi(t)\rangle \tag{3.32a}$$

$$\ddot{\zeta}(t) = a^*(t)\int d^3k\langle g| - \partial_z V(r)|k + A(t)\rangle a(t^r_{sp})\mathrm{f}(E,\eta)e^{-iS\left(k,t,t^r_{sp}\right)} \tag{3.32b}$$

which can then be evaluated by taking the saddlepoint approximation with respect to momentum

$$S(k, t, t^r_{sp}) = S(k_{sp}, t, t^r_{sp}) + \nabla^2_p S(k_{sp}, t, t^r_{sp})\frac{(k - k_{sp})^2}{2} \tag{3.33}$$

where $\nabla^2_p S(k_{sp}, t, t^r_{sp}) = (t - t^r_{sp})$. Finally, calculating Equation 3.32b by integrating around the saddle point, we get:

$$\ddot{\zeta}(t) = 2^{3/2}\pi(2I_p)^{1/4}e^{i\pi/4}\sum_n \frac{a^*(t)a(t^r_{n\_sp})\sqrt{w\big(E(t^r_{n\_sp})\big)}}{|E(t^r_{n\_sp})|(t-t^r_{n\_sp})^{3/2}} \tag{3.34}$$

The the expression for dipole acceleration in Equation 3.34 can be thought of in terms of electron trajectories. The dipole acceleration at time t is due to trajectories born at $t^r_{n\_sp}$ and returning back to the electron at t; $a(t^r_{n\_sp})$ and $w\big(E(t^r_{n\_sp})\big)$ are the ground state amplitude and the ionization rate at the time of birth; $a^*(t)$ is the ground state amplitude at the time of return; and $(t-t^r_{n\_sp})^{3/2}$ is the quantum diffusion term.

3.2 Numerical Time Dependent Schrödinger equation

We can solve the Time Dependent Schrödinger Equation of the atom-laser interaction numerically. Since the wavelength of the electric field is much longer than the trajectory of the electron, dipole approximation ($E(\mathbf{r},t) \approx E(t)$) can be made. This means that magnetic field $\left(\nabla \times E = -\frac{\partial B}{\partial t}\right)$ is ignored. Then the Schrödinger Equation in length gauge for the wave function and coulomb gauge for the electromagnetic field can be written as

$$i\frac{\partial \Psi(\mathbf{r},t)}{\partial t} = \left(-\frac{\nabla^2}{2} + V_{eff}(\mathbf{r}) - \mathbf{E}(t)\cdot\mathbf{r}\right)\Psi(\mathbf{r},t) \tag{3.35}$$

$\Psi(\mathbf{r},t)$ is the ground state wavefunction, $V_{eff}(\mathbf{r})$ is the effective potential as defined in Equation 2.5. Solving Equation 3.35 involves discretizing the Schrödinger equation in space and then propagating it in time. Let us look at each of these steps separately.

3.2.1 Discretization in Space

The presence of coulomb singularity can make the discretization of space in our problem a tricky affair. Smoothing the singularity is commonly used to circumvent this problem. This involves replacing the singularity at $r = 0$, which is proportional to $1/r$, by either $Z/(r+a)$ [39] or $Z/\sqrt{r^2+a^2}$ [40] . However, smoothing the singular-

ity can give incorrect photon yield by orders of magnitude. This is because of the different analytic behavior of the potential close to the origin is critical to the calculation of recombination amplitude [41]. According to the TSM, the amplitude of the emitted radiation is proportional to double derivative in time of the recombination amplitude [42]. If the returning electron is assumed to be defined by a plane wave, then calculation of the recombination amplitude is equivalent to finding the Fourier transform of the first excited state (first excite state $\sim r\psi_g(\mathbf{r})$) [41].

$$a_{rec}(k) = \langle g|z|e^{ikz}\rangle = \frac{1}{(2\pi)^{3/2}} \int d^3\mathbf{r}\psi_g^*(\mathbf{r})ze^{ikz} \tag{3.36}$$

The Fourier transform of a function is sensitive to the discontinuities in the derivative of the function. In the absence of any derivative discontinuity, the transform decays exponentially for large k . If a discontinuity is present, the transform decays like a power law whose exponent is determined by the order of the derivative of the discontinuity [41]. Since the coulomb singularity is responsible for the discontinuity in the first derivative of the wave function, it is important that we treat it carefully.

Singularity in our problem can be handled using Asymptotic Behavior Correspondence (ABC) [43]. Cylindrical co-ordinate system is used as symmetry considerations can help reduce the three dimensional problem to a two dimensional problem. In cylindrical co-ordinate system laplacian operator is

$$\Delta f = \frac{\partial^2 f}{\partial^2 \rho} + \frac{1}{\rho^2}\frac{\partial^2 f}{\partial^2 \theta} + \frac{1}{\rho}\frac{\partial f}{\partial \rho} + \frac{\partial^2 f}{\partial^2 z} \tag{3.37}$$

Substituting $f = \frac{g}{\sqrt{\rho}}$ the laplacian becomes

$$\Delta g = \frac{\partial^2 g}{\partial^2 \rho} + \frac{1}{\rho^2}\frac{\partial^2 f}{\partial^2 \theta} + \frac{\partial^2 g}{\partial^2 z} + \frac{g}{4\rho^2} \tag{3.38}$$

It should be noted that the cylindrical symmetry breaks down if the laser field is not linearly polarized or the ground state does not have cylindrical symmetry.

3.2.2 Calculation of ground state

Once we have set up the discrete Hamiltonian, the next step is to find the ground state. Ground state is found using the Imaginary Time Propagation (ITP) method [44]. We map time $t \rightarrow i\tau$ and propagate a random guess for ground state using the Schrödinger equation in imaginary time:

$$\frac{\Psi(\mathbf{r},\tau)}{d\tau} = -H\Psi(\mathbf{r},\tau) \tag{3.39}$$

A random guess of the initial state $\Psi(\mathbf{r},0)$ can be written as a superposition of the eigenstates of the hamiltonian

$$\Psi(\mathbf{r},0) = \sum c_i\psi_i \tag{3.40}$$

Inserting Equation 3.40 in Equation 3.39, the time evolution of each eigenstate is

$$\psi_i(\tau) = e^{-\tau E_i}\psi_i(0) \tag{3.41}$$

Ground state has the smallest energy and therefore the more energetic eigenstates decay exponentially faster

$$\frac{\psi_i(\tau)}{\psi_g(\tau)} = e^{-\tau(E_i - E_g)} \tag{3.42}$$

3.2.3 Propagation in time

Once we have found the discrete ground state, the next step is to propagate this state in time in the presence of the perturbative electromagnetic field. The Schrödinger equation is a parabolic partial differential equation. There are several techniques to march the solution of a parabolic PDE in time. They can be divided into two broad categories

Implicit Schemes: These schemes are unconditionally stable but can be numerically expensive because they involve matrix inversion. Examples of Implicit schemes are Crank Nicolson and Backward Euler.

Explicit Schemes: These schemes have conditional stability and are relatively inexpensive numerically. However, due to conditional stability, time and space discretization has to be carefully chosen to prevent the simulation from becoming unstable. Examples of Explicit schemes are Forward Euler and Leapfrog method. For our numerical simulation we use the latter. Expanding the wave function in the eigenstates of the atomic hamiltonian ($\Psi(\mathbf{r},t) = \sum c_i(t)\psi_i(\mathbf{r})$), the Schrödinger equation for each state becomes:

$$\frac{c^{n+1} - c^{n-1}}{2\Delta t} = -iEc^n \tag{3.43}$$

Superscript n represents the time step. To calculate the time step $n+1$, hamiltonian needs to be applied on the time step n . To find the stability of the numerical scheme, the time evolution operator S , such that $c^{n+1} = Sc^n$. So the characteristic equation for Equation 3.43 is

$$\left(S^2 + 2i\Delta t E S - 1\right)c^n = 0 \tag{3.44}$$

with solutions $\sigma_{1/2} = -iE\Delta t \pm \sqrt{1 - (E\Delta t)^2}$. Of the two solutions, only σ_2 is stable provided $|\sigma_2| < 1$. In other words, $E\Delta t < 1$. Therefore the largest eigenenergy in the simulation determines the largest time-step in the simulation. Since we know from TSM, the largest energy in our simulation is the cut-off energy, we can choose the right time-step accordingly.

To get a rough idea of the stability condition in our problem, we neglect the atomic potential. Then the Hamiltonian reduces to a laplacian or the kinetic energy operator. In the matrix formalism, it is a tri-diagonal matrix A (which has 2 as the diagonal and 1 as the the off-diagonal term.) The discretized Schrödinger equation is

$$\Psi^{n+1} - \Psi^{n-1} = -i\frac{2\Delta t}{\Delta x^2}A\Psi^n \tag{3.45}$$

Eigenvalues of tri-diagonal matrix with diagonal b and off-diagonal a is given by $E_j = b + 2a\cos(\frac{j\pi}{N})$. The above equation along with $E\Delta t < 1$ gives the stability condition

$$\frac{4\Delta t}{\Delta x^2} < 1 \tag{3.46}$$

In our code we use a stronger stability condition of $\Delta t = 0.05\Delta x^2$. Reflection from the boundaries is prevented by using absorbing boundary conditions [45]. Once the wavefunction is calculated as a function of time, dipole moment can be calculated using the Ehrenfest theorem.

3.3 Results

3.3.1 Study of ionization rates

Two analytical expressions of describing the ionization of Hydrogen by a 800 nm IR field have been discussed. The first is the ADK method (Equation 3.2) and the second is the Non-adiabatic (NA) ionization (Equation 3.5). The ground state amplitude can also be numerically calculated by projecting the time dependent wavefunction on the numerically calculated ground state:

$$a_{NTDSE}(t) = \left|\langle\psi_g|\Psi(t)\rangle\right|^2 \tag{3.47}$$

We compare the analytical ionization rates with Equation 3.47 in two regimes: (a) tunneling regime ($\gamma = 0.5$), Figure 3-4 and (b) multiphoton ionization regime ($\gamma = 1$) Figure 3-5. In the tunneling regime, the ADK formula overestimates the ionization while the NA and NTDSE models predict almost the same ionization rates. In the multiphoton ionization regime, both the NA and the ADK theories predict a higher ionization rate than the NTDSE.

3.3.2 Effect of the interplay of multiphoton and tunneling ionization on HHG spectrum

In this section, the effect of the choice of the ionization model on the HHG spectrum is investigated. As it was evident from the comparison of ionization models in the

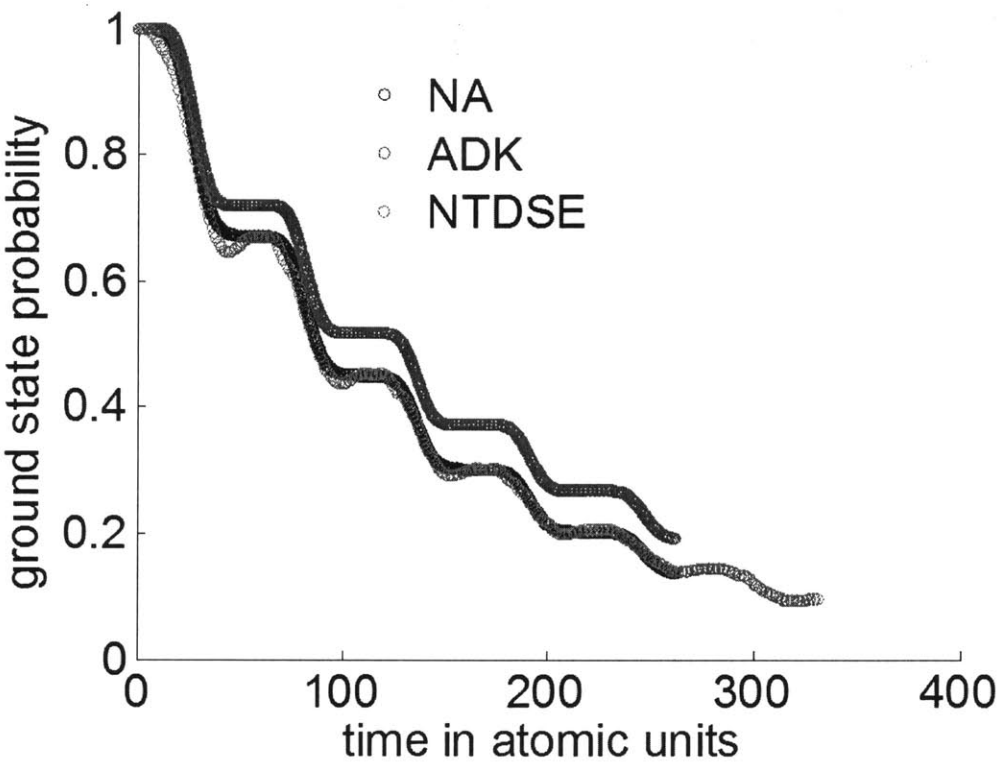

Figure 3-4: Ionization from Hydrogen by 800 nm IR pulse with electric field E = 0.104 au. This corresponds to a keldysh parameter of $\gamma = 0.5$.

previous section, the two ionization models used in the three step model greatly differ from each other in the regime where multiphoton ionization becomes important ($\gamma \sim 1$). At the wings of the driver pulse, the electric field is small and as a result, γ becomes large. Similarly, as the wavelength of the driver pulse decreases, γ increases. In Figure 3-6, the ionization rate calculated using the ADK and the non-adiabatic model (here referred to as YI) are compared for a 400 nm driver pulse with $\gamma \sim 1$ (Panel a). In Panel (b), the respective HHG spectra are compared. Similar comparison is made in Figure 3-7, for 800 nm driver pulse with $\gamma \sim 0.52$. Once again, we find that the NA ionization model predicts greater ionization rates than the ADK model and this effect is strong when $\gamma \sim 1$ (for shorter wavelength driver and at the wings of the IR pulse.) Due to the difference in ionization rates, the HHG spectra also differ from each other. To further illustrate the dependence of the HHG spectrum on the ionization model, the spectrograms of HHG spectrum generated by 400 nm and 800 nm driver pulses

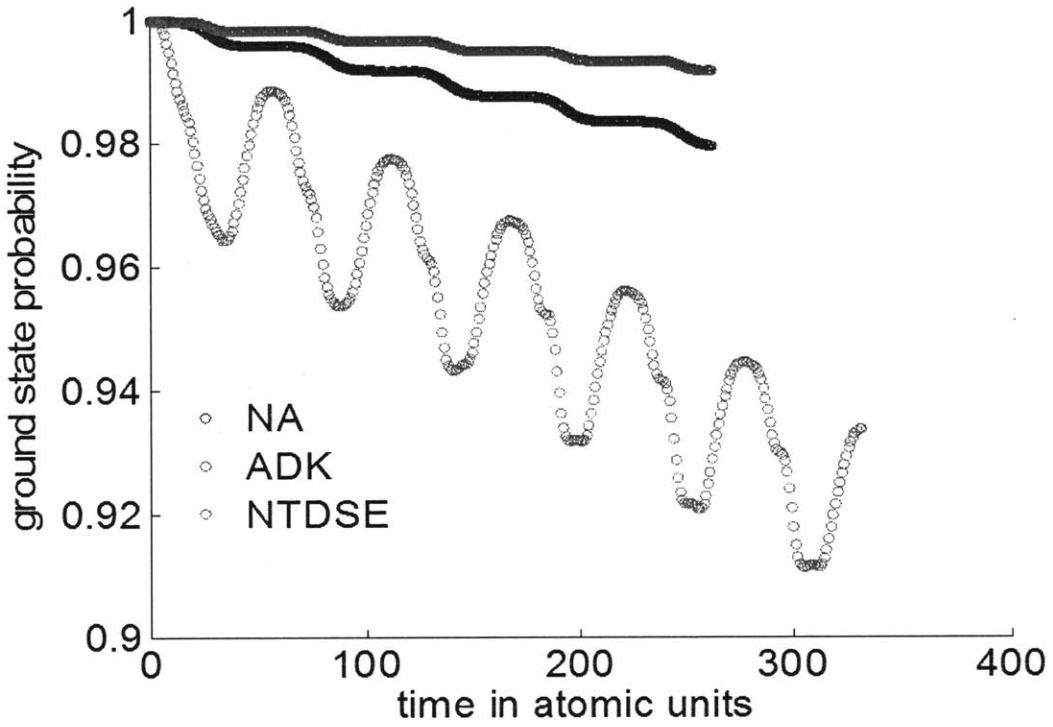

Figure 3-5: Ionization from Hydrogen by 800 nm IR pulse with electric field E = 0.057 au. This corresponds to a keldysh parameter of $\gamma = 1$

are calculated and compared. The spectrograms are calculated using a short-time Fourier transform with a Gaussian window function which has a FWHM of 58 as. As we can see in Figure 3-8, the spectrograms generated by 800 nm are insensitive to the choice of the ionization model. However, for 400 nm driver pulse, the difference between the two model is evident, particularly in the wings of the driver pulse.

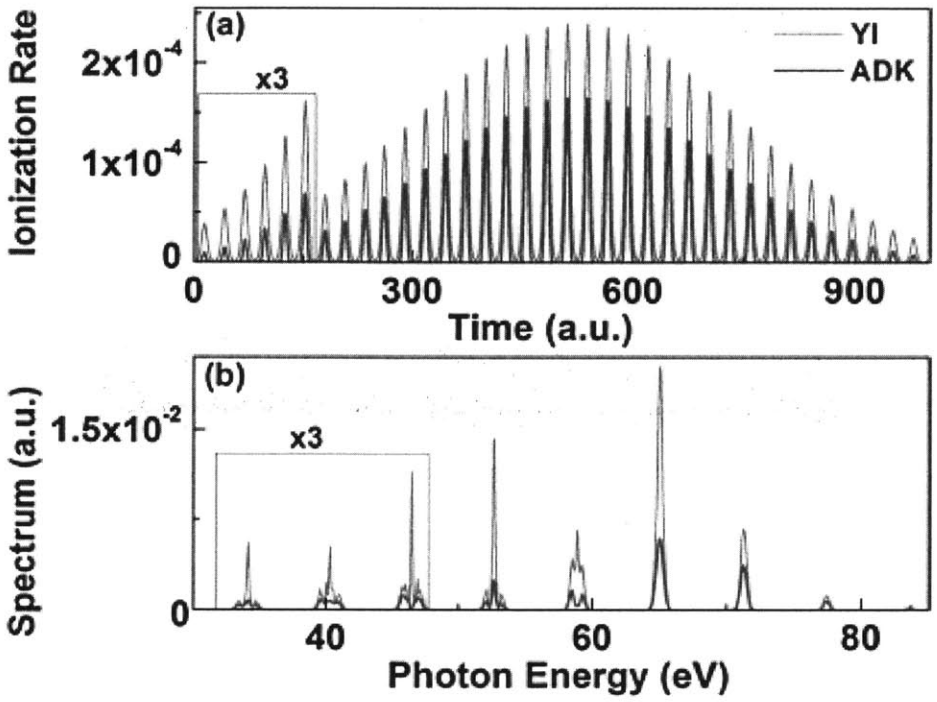

Figure 3-6: Ionization rates and spectral intensities of single-atom response of He when using the YI (gray) and ADK (red) theory for 400 nm, 26 fs, 1 mJ driver pulses with a beam waist of 30 micrometers. This corresponds to ($\gamma \sim 1$). The insets show the ionization rates for the wings of the fields and the spectral intensities for the low-order harmonics pronounced three times This figure is taken from [3]

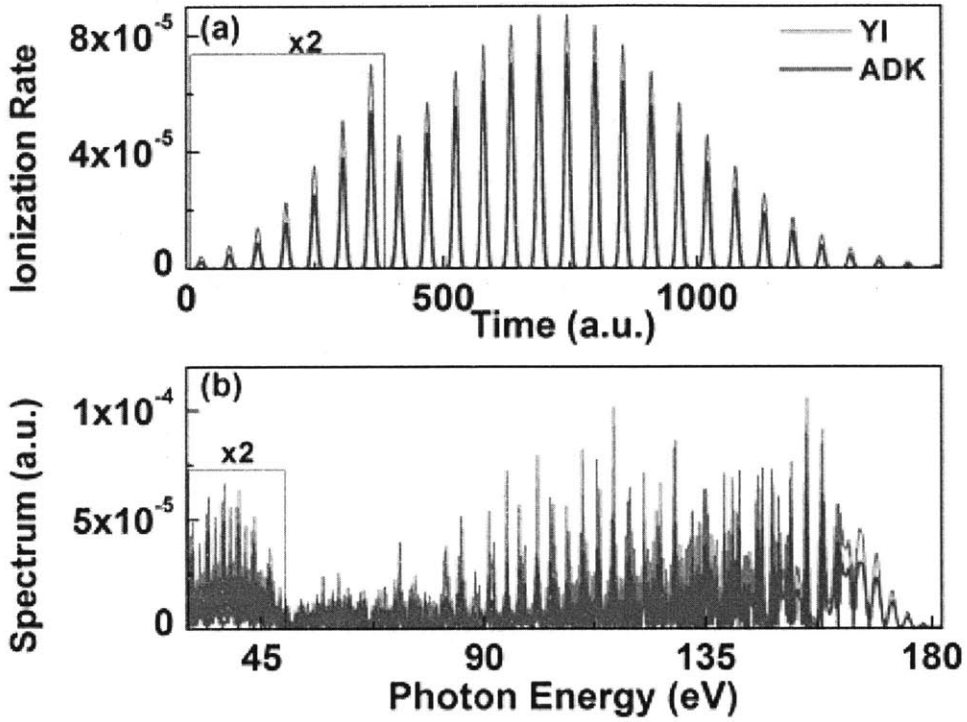

Figure 3-7: Ionization rates and spectral intensities of single-atom response of He when using the YI (gray) and ADK (red) theory for 800 nm, 35 fs, 2 mJ driver pulses with beam waist of 40 micrometers. This corresponds to ($\gamma \sim 0.52$). The insets show the ionization rates for the wings of the fields and the spectral intensities for the low-order harmonics pronounced two times. This figure is taken from [3]

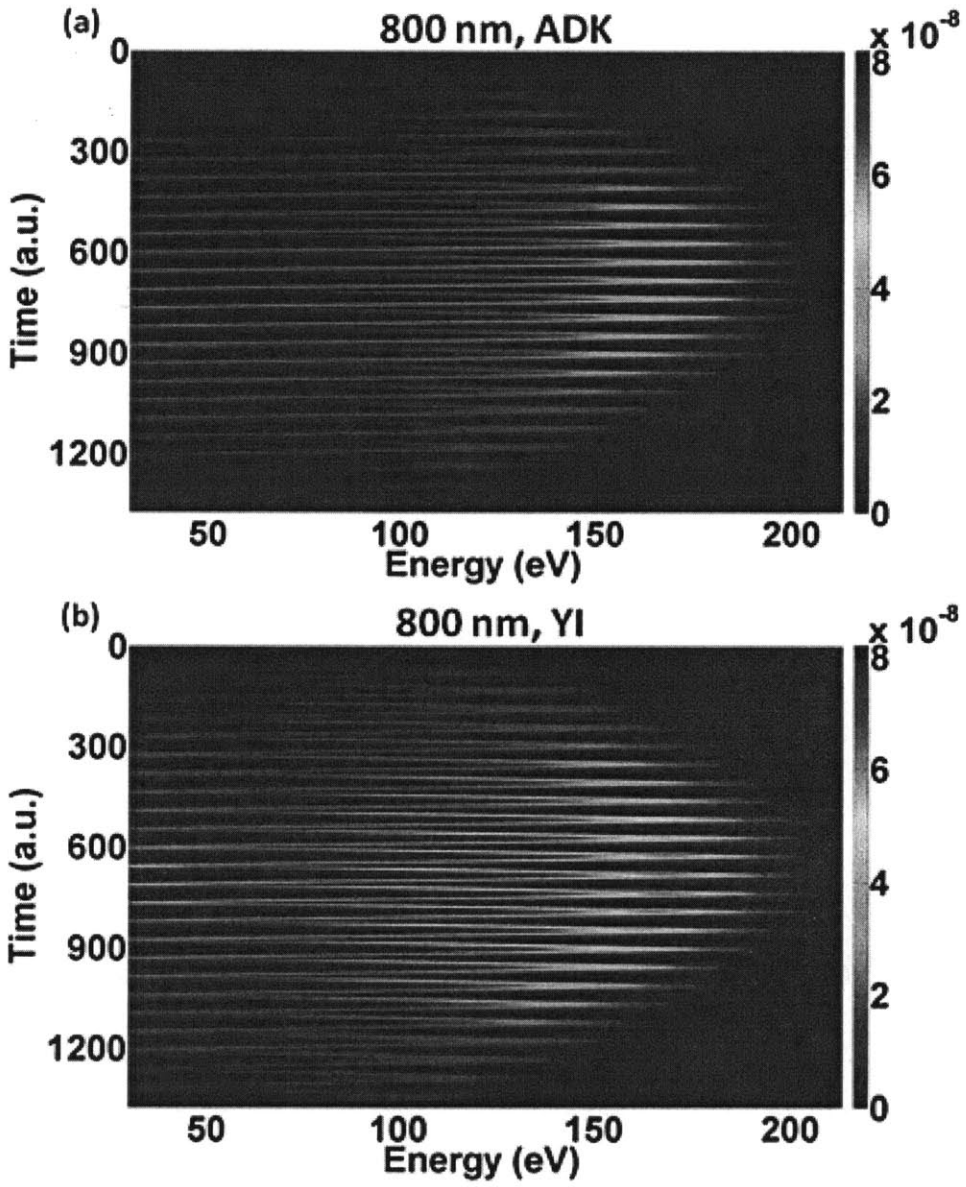

Figure 3-8: Spectrogram of the HHG spectrum from 800 nm driver pulse using (a) ADK and (b) YI ionization rates, respectively. Both models (YI and ADK) predict similar low-frequency photon intensity in the wings of the driver pulse. This figure is taken from [3]

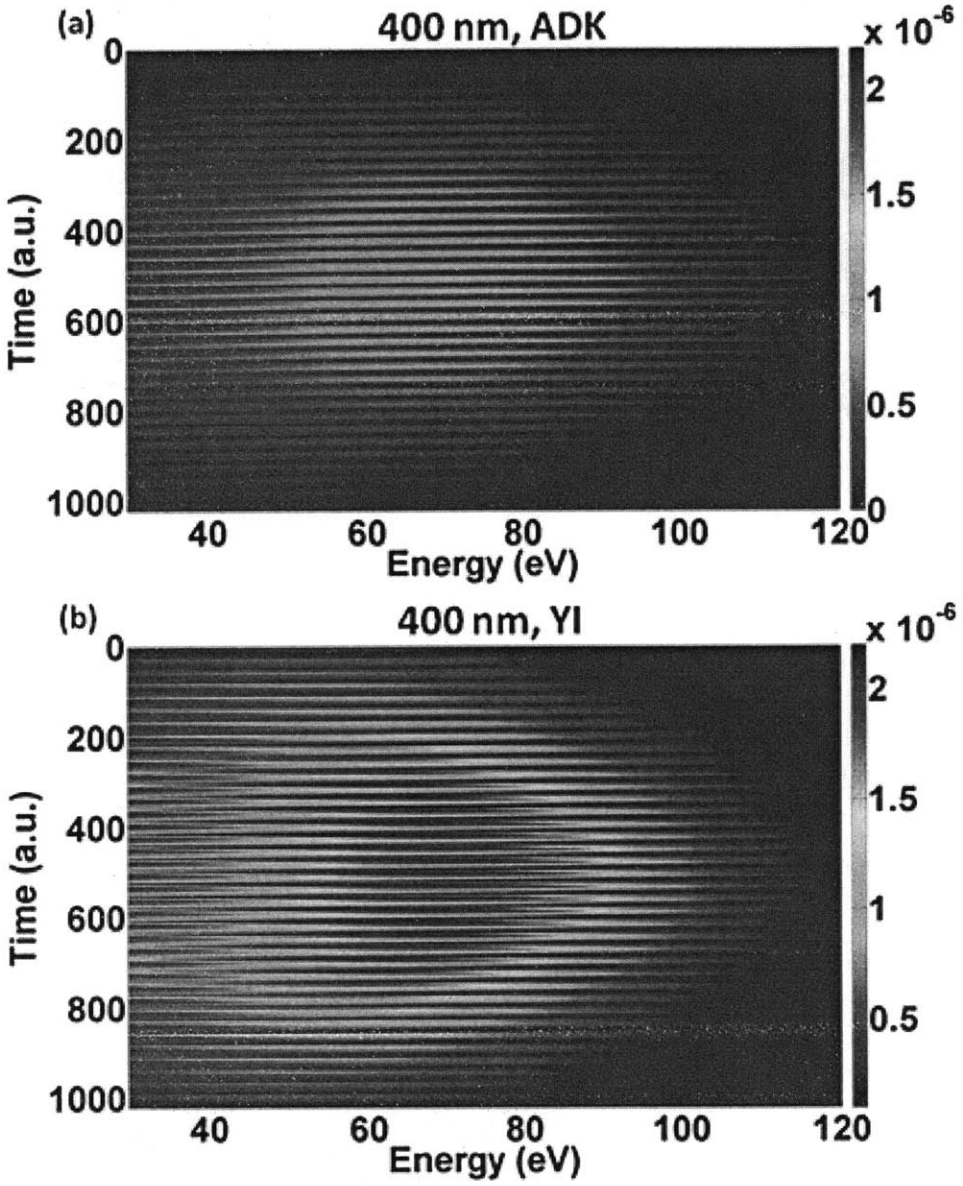

Figure 3-9: Spectrogram of the HHG spectrum with 400 nm driver pulse using (a) ADK and (b) YI ionization rates, respectively. The YI model predicts a much higher low-frequency photon intensity in the wings of the driver pulse than does the ADK model. This figure is taken from [3]

3.3.3 Isolated attosecond pulse generation

The pulse synthesizer developed in our lab can generate unique sub-cycle driver pulses. The intensity profile of these sub-cycle pulse lasts for less than a cycle. As a result, ionization can occur only at a few peaks and therefore, it is possible to generate isolated attosecond pulses. In order to demonstrate this, we numerically solve the TDSE of the interaction between the subcycle waveform (shown in panel (a) of Figure 3-10) with peak intensity of 6×10^{14} W/cm^2. From the time dependent wavefunction, dipole acceleration is calculated using the Ehrenfest theorem. The spectrogram (Figure 3-10b) is calculated using a short-time fourier transform with a gaussian windowing function of 58 as FWHM.

To gain more insights into the results given by the 3D TDSE simulation, we also calculated the ionization dynamics using the ADK formula (the red curve in Figure 3-10a) and the classical electron trajectories (overlaid on top of the spectrogram in Figure 3-10b). Electron trajectories from three ionization events, which are labeled in numbers, are calculated and those trajectories that return to the ionized atom are shown in Figure 3-10b. For visualization purpose, electrons ionized by the electric field with strength weaker than half of the maximum peak are neglected since they have negligible contribution to the HHG emission, as confirmed by the TDSE simulation.

In HHG, quantum diffusion and ionization rate are two competing factors in determining the ratio between radiation from long and short electron trajectories. While quantum diffusion always favors the short trajectories, when the HHG process is driven by conventional sinusoidal electric-field waveforms, stronger ionization rate for the long trajectories results in significant radiation from electrons of both trajectories. For the example shown in Figure 3-10b, where a sub-cycle waveform is used, the difference in travel time between long and short trajectories is increased. In addition, the ionization contribution to short trajectory radiation is boosted. Overall, quantum diffusion dominates and effectively eliminates the radiation from long trajectories, resulting in isolated soft x-ray pulse generation solely from short trajectories.

The peak intensity (6×10^{14} W/cm^2) is chosen such that the total ionization is

below the critical ionization level in helium. This intensity can be reached with a beam diameter of 27 micrometers ($1/e^2$). The transmission and dispersion of the Sn filter used for Figure 3-10c are taken from [REF See REF 4 of supplement]

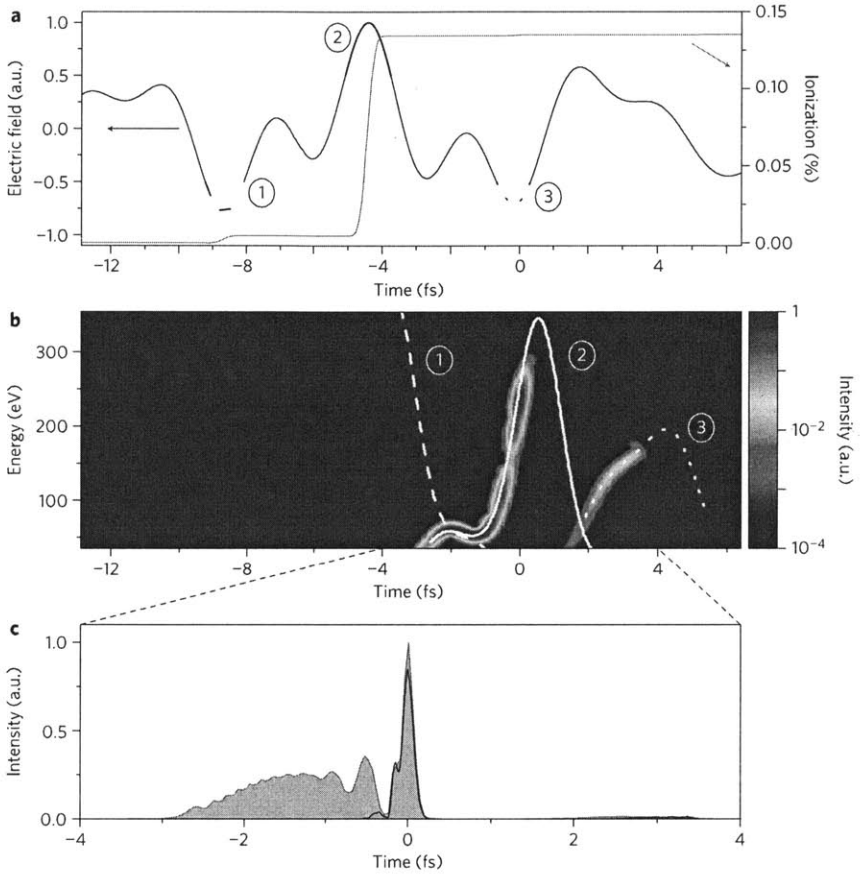

Figure 3-10: TDSE simulation results of interaction between sub-cycle driver with helium. (a) Ionization dynamics (red) induced in helium by a linearly polarized electric-field waveform (black) assuming a peak intensity of 6×10^{14} W/cm^2. (b) Spectrogram of the HHG superimposed with the calculated classical trajectories. Returning trajectories from three ionization events (2: main pulse; 1,3: satellite pulses) are shown for clear interpretation of the spectrogram. The synthesized pulse isolates the ionization process to a half optical cycle, and a continuum spectrum spanning more than 250 eV can be achieved. The isolated soft X-ray pulse has the same sign of chirp over 80% of the spectrum so the compression setup can be simplified. (c) Isolated sof X-ray pulse plotted in the time domain before (pink) and after (black line) a $100 - \text{nm}$ thick Sn filter. The Sn filter is chosen for its ability to block the strong IR driving field and the nonlinearly chirped low-photon-energy spectral content, and its good transmission in the soft X-ray range. The filtered isolated soft X-ray pulse has a FWHM duration of 150 as. This figure is taken from [46]

3.3.4 Carrier envelop phase dependence of high-order harmonic spectrum

Recently, coherent synthesis of multi-color broadband spectra has enabled the generation of phase controlled sub-cycle pulses [46, 47]. The capability of optimizing the shape of the electric-field waveform of non-sinusoidal pulses, through modification of its carrier and envelope, most notably the carrier-envelope phase (CEP) relationship, enables control of strong field laser-atom interaction for XUV spectroscopy and attosecond pulse generation. Although HHG from few-cycle to two-cycle pulses as well as periodic trains of non-sinusoidal pulses has been amply explored [48, 49, 50, 51], the case of sub-cycle pulses has so far only received limited attention. In this section, we compare calculations for HHG driven by sub-cycle and 1.5-cycle pulses that illuminate extreme carrier-envelope phase (CEP) sensitivity of the cut-off energy and provide enhanced control for generation of attosecond pulses.

It has been theoretically shown that the electron recollision energy can by controlled by shaping the electric field waveform within an oscillation period [51]. As the FWHM driver pulse approaches the sub-cycle regime, the electric field envelope varies rapidly from one half cycle to another and thereby facilitates strong CEP dependence within a single optical cycle. Fingerprints of CEP dependence such as frequency shifting of the harmonics close to cut-off and change in the shape of the cut-off itself have been observed only for few cycle pulses. As we move towards sub-cycle pulses ($2-3$ fs, 800 nm), the CEP effects are more dramatic. In this section, we identify and explore two of these effects: change in the cut-off shape and energy and implementation of ground-state depletion gating for isolated attosecond pulse generation. The discussion is based on the single atom response using the Three Step Model in the single active electron approximation [38]. To keep the dynamics simple, we used a Gaussian shaped pulse ensuring that there is no unphysical dc component.

The CEP dependent harmonic spectrum of Argon for a 2 fs (Figure 3-11 a) and a 4 fs (Figure 3-11 b) driver pulse at 800 nm and a peak intensity of 8.9×10^{14} W/cm^2 are shown. For the 4 fs pulse, the cut-off is made up of discrete harmonics for only

a small range of CEP values from 0.2π to 0.5π. For other CEP values a smooth continuum is observed at the cut-off, indicating an isolated attosecond pulse when properly filtered. The cut-off is a continuum when the CEP dependent electric field waveform creates the most energetic photons in a single optical half-cycle. For the 2 fs pulse, a broad continuum at the cut-off is always observed. Additionally, the energy of the cut-off drops sharply by about 100 eV as we sweep the CEP form 0.2π to π. Conversely, now one can uniquely infer the CEP of a sub-cycle pulse by looking at the cut-off of the harmonic spectrum. This is qualitatively different from the method employed in [48], where the shape of the cut-off was used to determine the CEP. Since there is only a single ionization event, harmonics are not observed rather we see an interference pattern between the long and short quantum trajectories. Figure 3-11c and Figure 3-11d show the electric field waveforms of the 2 fs sub-cycle pulse for CEP values of 0.4π and 0.8π, respectively. The green curve shows the energy versus time plot of the returning trajectories and the electric field values where they are born is highlighted in red. When the CEP value changes from 0.4π to 0.8π, the electric field following the ionization event gets suppressed and therefore the electron trajectories return back with lower kinetic energy resulting in a red-shifted HHG spectrum.

The aforementioned behavior of the cut-off changes dramatically once again, when the electric field becomes strong enough to deplete the ground-state (Figure 3-12). For the sub-cycle pulse of peak intensity 2×10^{15} W/cm^2 and zero CEP (Figure 3-12a) a smooth continuum centered at 45 eV is observed while at 0.5π CEP, harmonic radiation is suppressed due to ground-state depletion (Figure 3-12d). For the 4 fs pulse (Figure 3-12b), the harmonics between 40 eV and 80 eV show only a weak CEP dependence. The drop in cut-off energy for both cases is due to ground-state depletion before the most energetic electrons return to the atom. For the sub-cycle pulse (Figure 3-12a), there is an additional effect: interference between short and long trajectories within a single half cycle has disappeared because the ground-state is completely depleted by the time the long trajectories return. Importantly, this intra-cycle ground-state depletion allows for shaping of the isolated attosecond burst spectrum and temporal duration. In contrast to the 2-cycle case where ground-

state depletion has been used to generate isolated attosecond pulses [REF8] where depending on CEP one or two attosecond bursts of XUV photons are generated, with sub-cycle pulses, isolation of a single pulse takes place uniformly, and the CEP can be used to control attosecond pulse properties. Most notably, pulse emission is completely suppressed for CEP around 0.5π.

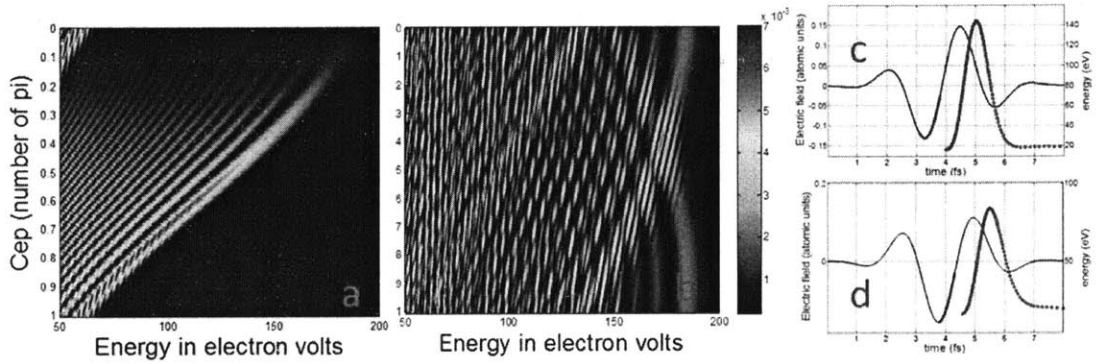

Figure 3-11: CEP dependent harmonic spectrum at 800 nm for a laser pulse of duration (a) 2 fs pulse and (b) 4 fs pulse at peak electric field 8×10^{14} W/cm^2. (c) and (d) show the electric field waveform (blue) and the kinetic energy versus time plots of the trajectories (green) for CEP of 0.4π and 0.8π respectively. The electric field corresponding to the birth of the trajectories is marked in red

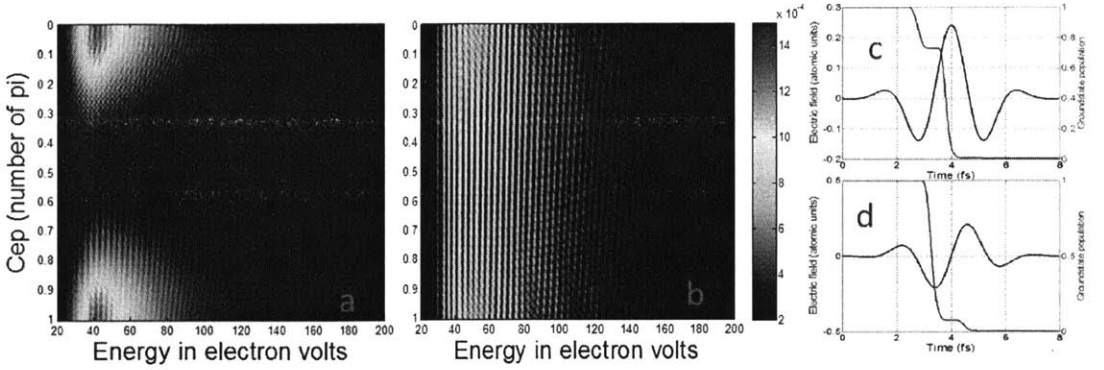

Figure 3-12: CEP dependent harmonic spectrum at 800 nm for a laser pulse of duration (a) 2 fs pulse and (b) 4 fs pulse for peak electric field I 2×10^{15} W/cm^2. In (c) and (d) the 2 fs electric field waveform (blue) and ground- state population (green) for CEP values of 0 and 0.5π respectively

Chapter 4

Recombination Amplitude

4.1 Introduction

The three step model (TSM) is commonly used to describe the dynamics of an electron in the strong field regime, which is responsible for generation of high-order harmonics [13] . In this semiclassical description, the dynamics of a single electron is simplified into three distinct steps: ionization, propagation and recombination (back to the orbital of origin in the parent atom or molecule). The amplitude of the harmonic dipole is determined by a product of the amplitudes of each of the three steps [42]. In the TSM, it is assumed that while the first two steps are affected by the strong IR field; the recombination step, which leads to the generation of high-order harmonics, is not affected by the strong IR field. It has been shown that the qualitative shape of the plateau in the HHG spectrum almost exclusively depends on the recombination amplitude [52, 19, 53]. Additionally, the recombination step serves as a probe that imprints information about electronic orbital [15], atomic attosecond dynamics [17, 54] and molecular motion [55] onto the harmonic spectrum. The central role that the recombination step plays in the aforementioned experiments serves as a strong motivation for a systematic study of the recombination amplitude of noble gases commonly used in HHG.

The recombination amplitude describes the transition of the returning electron back into the atomic orbital from where it originated. The strength of this transition

is given by a dipole transition matrix element that depends on the wavefunction used to describe the returning electron. Since, it is not possible to calculate the exact many-body eigenstates of the electrons in the atom, one needs to resort to various approximations to describe the electronic wavefunction. A key assumption made in the TSM is that only a single electron participates in the HHG process while the ion core remains frozen. In this picture, the electron from the outermost valence orbital aligned along the laser polarization tunnel ionizes and upon return recombines to the same orbital. This is called the single active electron approximation (SAEA) (See Equation 2.5). In this chapter, we use an effective atomic potential (V_{HFS}) to calculate the bound and continuum eigenstates. The effective atomic potential is obtained from the Hartree Fock Slater (HFS) model which employs a local density approximation for the exact exchange interaction [25]. An important consequence of approximating the exact manybody eigenstate with the eigenstates of V_{HFS} while using the exact hamiltonian in the acceleration form, is that the form invariance of the dipole operator is lost, i.e., the recombination amplitude depends upon whether the dipole operator is in the length, or in the acceleration form [56].

Another important assumption made in the TSM is that after ionization the electron moves only under the influence of the laser field without any interaction with the Coulomb potential of the ion core. The rationale behind this assumption, often referred to as the strong field approximation (SFA), is that in strong-field processes like HHG, the ionized electron can travel hundreds of Bohr radii away from the atom. Therefore, its trajectory, for the most part, is that of a free electron in an external electric field which can be described by Volkov states (plane waves with timedependent momentum) [57]. The basic assumptions of SFA are: (a) neglect the laser field for the calculation of bound states and (b) neglect the core Coulomb potential for the calculation of the continuum states [58]. A recently measured HHG spectrum of Ar is shown to have a deep minimum (related to the Cooper minimum of its photoelectron spectrum) that is independent of the laser intensity or wavelength [4, 59]. See Figure 4-1. This Cooper minimum of the HHG spectrum can be theoretically reproduced if the ionized electron is defined by outgoing scattering eigenstates [60]

(which are the continuum eigenstates of the effective potential V_{HFS}) rather than plane waves while keeping the bound states as eigenstates of fieldfree Coulomb potential [4]. This indicates that while the first assumption of SFA appears to be valid, the second assumption is not accurate. Hence we are motivated to use the outgoing scattering eigenstates rather than the plane (Volkov) waves in the calculation of the recombination amplitudes of all noble gases used in HHG.

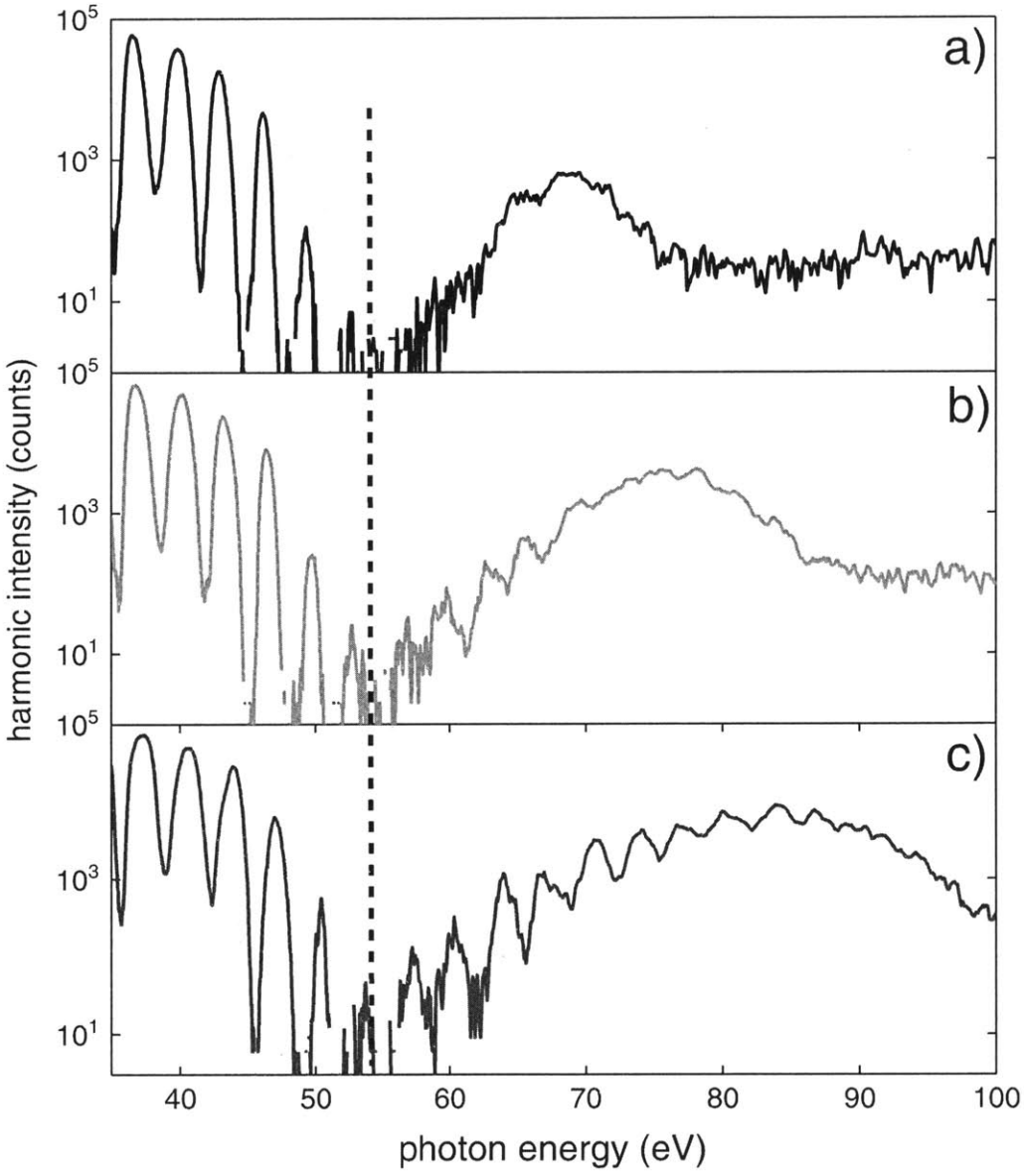

Figure 4-1: Experimentally observed HHG spectrum of Argon for different IR intensities: (a) $2.5 \times 10^{14}\mathrm{W/cm^2}$, (b) $2.9 \times 10^{14}\mathrm{W/cm^2}$ and (c) $3.5 \times 10^{14}\mathrm{W/cm^2}$. The position of the minimum is independent of the IR intensity. This figure is taken from [4]

Since photorecombination and photoionization cross sections have the same dipole transition matrix element, the recombination amplitude can be compared with the extensively studied photoionization cross section (PICS). Like the cooper minimum in the HHG spectrum, a cooper minimum has also been observed in the total photoionization cross section of argon. See Figure 4-2. Interestingly, the positions of the two minima are almost energetically identical. This suggests that the theoretical techniques applied to calculate photoionization from an atom can be applied to calculate the recombination process inspite of the presence of a strong IR field in the latter case. The mathematical relation between the recombination amplitude and the PICS will be discussed in detail in this chapter. The central potential model with a single active electron has also been used to calculate the PICSs in the extreme ultraviolet regime ($0 - 100$eV) [22] and xray regime [61] which are in qualitative agreement with experimental results. However, this simple model does not take into account interchannel coupling needed to explain the PICS of 3p shell in Ar and 4d shell in Xe [62]. Techniques such as Rmatrix theory [63], random phase approximation with exchange (RPAE) [64] incorporate interchannel coupling as a perturbation, while the relativistic random phase approximation (RRPA)[65, 66], in addition, also includes the relativistic effects. PICSs calculated using the RRPA match very well with the experimental measurements [67]. As we will see, it is possible to calculate the photorecombination cross section (PRCS) from PICS. In principle, by comparing the PRCS obtained from RRPA with the PRCS obtained from our recombination amplitude calculation, one can discuss the limitations of the central potential model with a single active electron. However, due to lack of m_J resolved PICS data from RRPA, we compare the differential photoionization cross section from our theory with that from RRPA.

In this chapter, we extensively investigate the recombination amplitudes of the commonly used noble gases in HHG. We show that the recombination amplitude versus emitted photon energy critically depends upon the choice of the wavefunction used to describe the returning electron as well as the form of the dipole operator. In some cases, the square of the absolute value of the recombination amplitude can differ

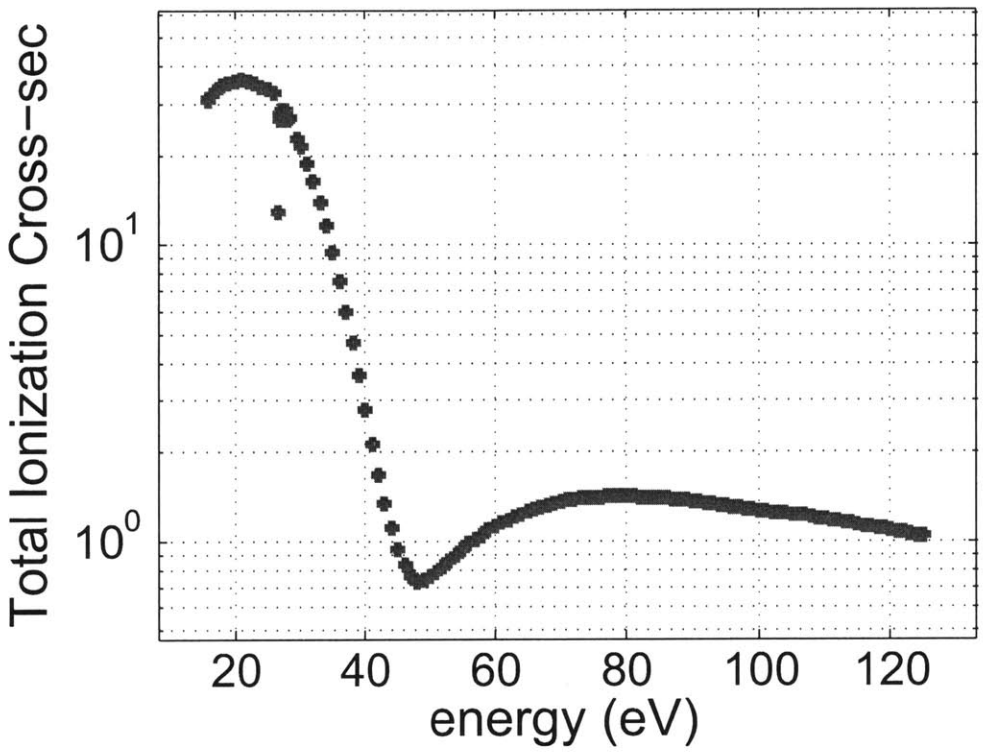

Figure 4-2: Experimentally observed total photoionization cross section for argon. The photoionization cross section has a minimum at $\approx$ 49eV. The data for this figure is taken from [5]

by two orders of magnitude because the Cooper minima are located at different energies. This is critical when predicting the efficiency of HHG process and in attosecond pulse generation at certain photon energies. In order to show the limitation of the central potential model, we compare the PICSs calculated using our recombination amplitudes with PICS obtained from the RRPA. This chapter is structured as follows: first we derive the recombination amplitude and show how to calculate PRCS from PICS. Then, the results are discussed and compared with the PICS data calculated using RRPA [68].

4.2 Derivation of the Recombination Amplitude

In the TSM formalism, the expression for the dipole moment and dipole acceleration of an atom interacting with intense IR field are:

$$\xi(t) = 2^{\frac{3}{2}}\pi(2I_p)^{\frac{1}{4}}e^{i\frac{\pi}{4}}\sum_n \frac{b(t_{nb}(t))b(t)\sqrt{w(E(t_{nb}(t)))}}{E(t_{nb}(t)(t-t_{nb})^{\frac{3}{2}}}a_{len}e^{-iS_n(t)} \tag{4.1}$$

$$\ddot{\xi}(t) = 2^{\frac{3}{2}}\pi(2I_p)^{\frac{1}{4}}e^{i\frac{\pi}{4}}\sum_n \frac{b(t_{nb}(t))b(t)\sqrt{w(E(t_{nb}(t)))}}{E(t_{nb}(t)(t-t_{nb})^{\frac{3}{2}}}a_{acn}e^{-iS_n(t)} \tag{4.2}$$

We briefly review the terms in this expression: $\zeta(t)$ and $\ddot{\zeta}(t)$ are the dipole moment and the dipole acceleration terms respectively; $E(t_{nb})$ is the electric field of the IR field at the time of birth of the n^{th} trajectory; w is the ionization rate that depends on the electric field at the time of birth; $b(t)$ and $b(t_{nb}(t))$ are the ground state amplitude at the time of birth and at the time of return of the trajectory; $S_n(t)$ is the action; I_p is the ionization potential of the atom. The expressions for dipole moment (Equations 4.1) and dipole acceleration (Equation 4.2) differ only by the form of the recombination amplitude: the length form a_{len} gives the dipole moment while a_{acn} gives the dipole acceleration. We would expect that due to form invariance, taking the second derivative of Equations 4.1 would reproduce Equations 4.2. However, due to the various approximation made (single active electron approximation, strong field approximation, saddle point approximation) in order to obtain the three step model, the form variance is lost.

The recombination amplitude or the dipole matrix element of transition from a momentum normalized free state $|\Psi_k\rangle$to the bound state $|\Psi_g\rangle$ can be written in the length and the acceleration form:

$$a_{len}(k) = \langle\Psi_g|z|\Psi_k\rangle \tag{4.3}$$

$$a_{acn}(k) = \langle\Psi_g| - \partial V_z|\Psi_k\rangle \tag{4.4}$$

When used in the TSM, Equation 4.3 gives the dipole moment and Equation 4.4 gives the dipole acceleration [20].The recombination amplitude in the length and the acceleration form are related by:

$$\langle \Psi_g | - \partial V_z | \Psi_k \rangle = \omega_{gk}^2 \langle \Psi_g | z | \Psi_k \rangle \tag{4.5}$$

where

$$\omega_{gk}^2 = \frac{k^2}{2} + I_p \tag{4.6}$$

is the energy of the photon emitted after recombination, k is the momentum of the ejected electron and I_p is the ionization potential. Although we use an effective Hartree-Fock-Slater potential V_{HFS} to calculate the electronic eigenstates, for the calculation of the recombination amplitude in the acceleration form, the exact multi-electron potential used in Equation 2.3 is used. Since the electron-electron interaction term cancels out, we get

$$\langle \Psi_g | - \partial V_z | \Psi_k \rangle = -Z_N \langle \Psi_g | \frac{z}{r^3} | \Psi_k \rangle \tag{4.7}$$

where Z_N is the atomic number. Validity of Equation 4.5 is predicated upon the usage of exact many-electron wavefunction for bound and free states.

We begin the calculation of the recombination amplitude by expanding the plane wave in the spherical co-ordinate system as an infinite sum of free spherical waves. For simplicity, it is assumed that the ionized electron moves along the z-direction. This allows us to limit the expansion to spherical waves with $m_l = 0$. Then the momentum-normalized plane wave and the ground state, projected on the r space become :

$$\langle \mathbf{r} | \Psi_k^{pl} \rangle = \sum_{l=0}^{\infty} a_l \frac{u_{kl}^{pl}(r)}{r} Y_{l0}(\Omega_r); a_l = \frac{i^l}{2k} \sqrt{\frac{2l+1}{\pi}} \tag{4.8}$$

$$\langle \mathbf{r} | \Psi_g \rangle = \frac{u_g(r)}{r} Y_{l0}(\Omega_r); \tag{4.9}$$

The radial part $u_{kl}^{pl}$is proportional to the momentum-normalized spherical Bessel function of the first kind:

$$u_{kl}^{pl} = \sqrt{\frac{2}{\pi}} j_l(kr) \tag{4.10}$$

$Y_{10}(\Omega_r)$is the spherical harmonic with zero magnetic quantum number. The radial part of the ground state orbital is calculated by solving the Hartree-Fock-Slater eigenvalue problem using a generalized pseudospectral method [69, 70] on a non-uniform grid. Recombination amplitudes for the plane waves are calculated by inserting Equation 4.8 and Equation 4.9 in Equation 4.3 for the length form, and Equation 4.4 for the acceleration form. The calculation is simplified because the summation over all angular momenta is reduced to the terms that satisfy the dipole selection rule $\Delta l = \pm 1$. Then, the recombination amplitude of a plane wave into the outermost orbital of He $|l = 0, m_l = 0\rangle$ in the length and acceleration form are given by Equation 4.11a and Equation 4.11b respectively. For other noble gases where the outermost orbital is $|l = 1, m_l = 0\rangle$, the recombination amplitude of the plane wave in the length and the acceleration form are given by Equation 4.11c and Equation 4.11d respectively.

$$a_{len}^{pl}(k) = a_1 c_1 \langle u_g | r | u_{k1}^{pl} \rangle \tag{4.11a}$$

$$a_{acn}^{pl}(k) = -a_1 c_1 Z_N \langle u_g | \frac{1}{r^2} | u_{k1}^{pl} \rangle \tag{4.11b}$$

$$a_{len}^{pl}(k) = a_0 c_0 \langle u_g | r | u_{k0}^{pl} \rangle + a_2 c_2 \langle u_g | r | u_{k2}^{pl} \rangle \tag{4.11c}$$

$$a_{acn}^{pl}(k) = -a_0 c_0 Z_N \langle u_g | \frac{1}{r^2} | u_{k0}^{pl} \rangle - a_2 c_2 Z_N \langle u_g | \frac{1}{r^2} | u_{k2}^{pl} \rangle \tag{4.11d}$$

Here, a_l is the coefficient of expansion as shown in Equation 4.8 , $c_l = \langle Y_{l_g}^{m=0} | \cos\theta | Y_l^{m=0} \rangle$ is the angular part of the integral and $u_g(r)$ is the radial part of the ground state orbital. Using $\cos\theta = \sqrt{\frac{4\pi}{3}} Y_{l0}$, we can express c_l in terms of Wigner 3j symbol [27]:

$$\int Y_{l_1 m_1}(\theta,\phi) Y_{l_2 m_2}(\theta,\phi) Y_{l_3 m_3}(\theta,\phi) \sin\theta d\theta d\phi$$
$$= \sqrt{\frac{(2l_1+1)(2l_2+1)(2l_3+1)}{4\pi}} \begin{pmatrix} l_1 & l_2 & l_3 \\ 0 & 0 & 0 \end{pmatrix} \begin{pmatrix} l_1 & l_2 & l_3 \\ m_1 & m_2 & m_3 \end{pmatrix} \tag{4.12}$$

For a spherically symmetric potential, the outgoing scattering eigenstate can be obtained by replacing the radial part of the free spherical wave u_{kl}^{pl} in Equation 4.11 by the radial part of the corresponding partial wave $e^{(\delta_l+\sigma_l)}u_{kl}^{sc}$ [34]. The radial part of the continuum states is solved by the fourth-order Runge-Kutta method on a uniform grid [22, 71] using the Hartree-Fock-Slater potential to calculate the ground state. Similar to the case of the plane wave, the recombination amplitude in the length and the acceleration form of the outgoing scattering eigenstate for He (Equation 4.13a and Equation 4.13b) and other noble gases (Equation 4.13c and Equation 4.13d) are:

$$a_{len}^{sc}(k) = a_1 c_1 e^{i(\delta_1+\sigma_1)} \langle u_g | r | u_{k1}^{sc} \rangle \tag{4.13a}$$

$$a_{acn}^{sc}(k) = -a_1 c_1 Z_N e^{i(\delta_1+\sigma_1)} \langle u_g | \frac{1}{r^2} | u_{k1}^{sc} \rangle \tag{4.13b}$$

$$a_{len}^{sc}(k) = a_0 c_0 e^{i(\delta_0+\sigma_0)} \langle u_g | r | u_{k0}^{sc} \rangle + a_2 c_2 e^{i(\delta_2+\sigma_2)} \langle u_g | r | u_{k2}^{sc} \rangle \tag{4.13c}$$

$$a_{acn}^{sc}(k) = -a_0 c_0 Z_N e^{i(\delta_0+\sigma_0)} \langle u_g | \frac{1}{r^2} | u_{k0}^{sc} \rangle - a_2 c_2 Z_N e^{i(\delta_2+\sigma_2)} \langle u_g | \frac{1}{r^2} | u_{k2}^{sc} \rangle. \tag{4.13d}$$

In the asymptotic limit, the radial part of the partial wave and the free spherical waves become:

$$u_{kl}^{sc} \xrightarrow[r\to\infty]{} \sqrt{\frac{2}{\pi}} \sin(kr - \frac{l\pi}{2} - \eta ln 2kr + \sigma_l + \delta_l) \tag{4.14}$$

$$u_{kl}^{pl} \xrightarrow[r\to\infty]{} \sqrt{\frac{2}{\pi}} \sin(kr - \frac{l\pi}{2}) \tag{4.15}$$

In the asymptotic limit, the radial part of the partial wave (Equation 4.14) and the radial part of the free spherical wave (Equation 4.15) differ by a phase shift which is

composed of three terms: the r dependent phase term is due to the long-range nature of the Coulomb potential, σ_l is the Coulomb phase shift and δ_l is the phase shift against the regular coulomb wave (due to the short-range part of the HFS potential V_{HFS}) [28]. The two terms in Equation 4.13c and Equation 4.13d correspond to s and d partial waves that satisfy the dipole transition rule for the bound p orbital. In Figure 4-3, the length form radial transition matrix element of the s wave ($\langle u_g|r|u^{sc}_{k0}\rangle$) and d wave ($\langle u_g|r|u^{sc}_{k2}\rangle$) are plotted. Interplay between the two terms determines the minimum in the recombination amplitude, which manifests itself in the commonly observed Cooper minimum in Ar [4, 59, 72].

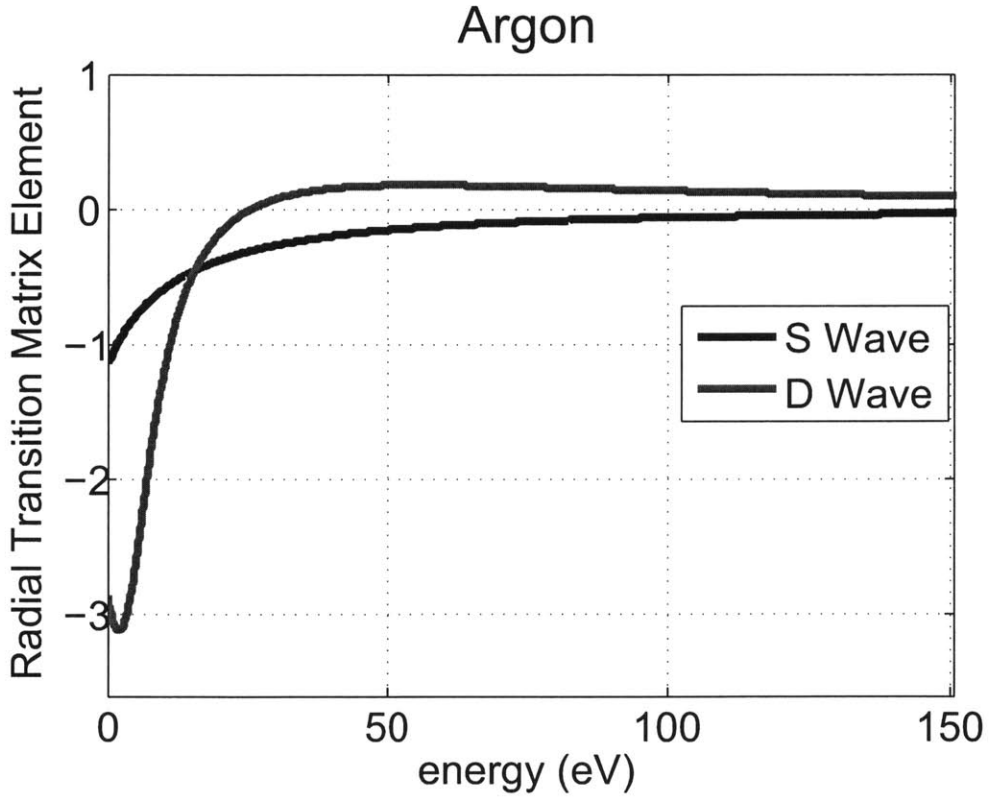

Figure 4-3: The radial dipole transition matrix elements for the s wave and the d wave. After 26eV, the s- and the d-wave have opposite sign. This leads to a minimum in the recombination amplitude and therefore a minimum in the HHG spectrum.

4.3 Results and Discussion

In Figure 4-4, the square of the absolute values of the recombination amplitude - calculated using plane waves and outgoing scattering eigenstates and dipole moment in both the length form and the acceleration form - have been plotted for Ar and Kr. In order to compare the length and the acceleration forms, the former has been multiplied by a pre-factor as shown in Equation 4.5. Calculations using the plane waves and the outgoing scattering eigenstates differ by almost two orders of magnitude around the experimentally measured Cooper minima ($\sim 50eV$ for Ar and $\sim 85eV$ for Kr) because the locations of the minima predicted by the plane wave are way off from the experimentally measured values. The results are also dependent on the form of the dipole operator: for outgoing scattering eigenstates, the minima for the length and the acceleration forms are located at 44 eV and 86 eV respectively for Argon, and 68 eV and 235 eV respectively for Krypton. The plane wave fails to reproduce the experimentally observed minima irrespective of the form of the dipole operator. This suggests that using a plane wave to describe the returning electron is a poor approximation which has also been demonstrated in the calculation of HHG spectra from molecules using quantum rescattering theory [27]. Hence, for the rest of the paper, we will only focus on outgoing scattering eigenstates.

For outgoing scattering eigenstates, we have compared the square of the absolute values of the recombination amplitude of various noble gases. In Figure 4-5 and Figure 4-6 these comparisons are shown for the length form and for the acceleration form respectively. The plots of different gases vary significantly as a function of the emitted photon energy. This information is crucial in determining the choice of gas for HHG in a particular energy range. The effect of the choice of the dipole form on the recombination amplitude of a given gas can be observed by comparing the plots in Figure 4-5 and Figure 4-6. For He and Ne, the results are quantitatively similar. As we move to heavier gases, the effect of the choice of the dipole form on the recombination amplitude becomes evident due to form-dependent minima. Therefore, we need to determine which form of the dipole moment is more suitable

in the modeling of HHG.

In modeling of HHG using the TSM, the acceleration form is often preferred because in the calculation of macroscopic propagation of HHG, the dipole acceleration is proportional to the polarization term in Maxwell's Equation. Usage of the length form would require taking a double time derivative which can become numerically cumbersome in 3-D modeling of the HHG process . Two reasons have been put forth in favor of the acceleration form. First, it has been shown that the high harmonic spectrum of hydrogen obtained from TSM is in better agreement with exact time dependent Schrödinger equation when the recombination amplitude in the acceleration form is used [20]. Second, experimentally observed scaling of HHG intensity with the atomic number of the noble gas has been explained using acceleration form in its exact form as shown in Equation 4.5 [21]. Due to the presence of atomic number Z_N in Equation 4.5, heavier atoms will have a higher recombination amplitude and therefore a stronger HHG radiation.

In both of the aforementioned studies (ref [20] and [21]), preference for the acceleration form stems from the fact that the returning electron is described by a plane wave rather than an outgoing scattering eigenstate. For hydrogen, when an outgoing scattering eigenstate is used to describe the returning electron, the recombination amplitude is form invariant. Similarly, PICS calculated using outgoing scattering eigenstate (of the effective central potential) and length form, increases for heavier gases [22]. Since PRCS is proportional to PICS (Equation 4.22), the former should also increase for heavier gases which explains the increase in HHG yield with atomic number. Hence, it is unclear if the acceleration form is inherently better than the length form. As discussed in the introduction, the lack of form invariance is due to the limitations of the SAE model based on a central potential. Since this approximation is extensively used to model HHG, it is important to know which of the two dipole forms can better reproduce the experimental results and in which energy regimes. In order to do so we will compare the total PICS obtained from our HFS model with the total PICS obtained using RRPA.

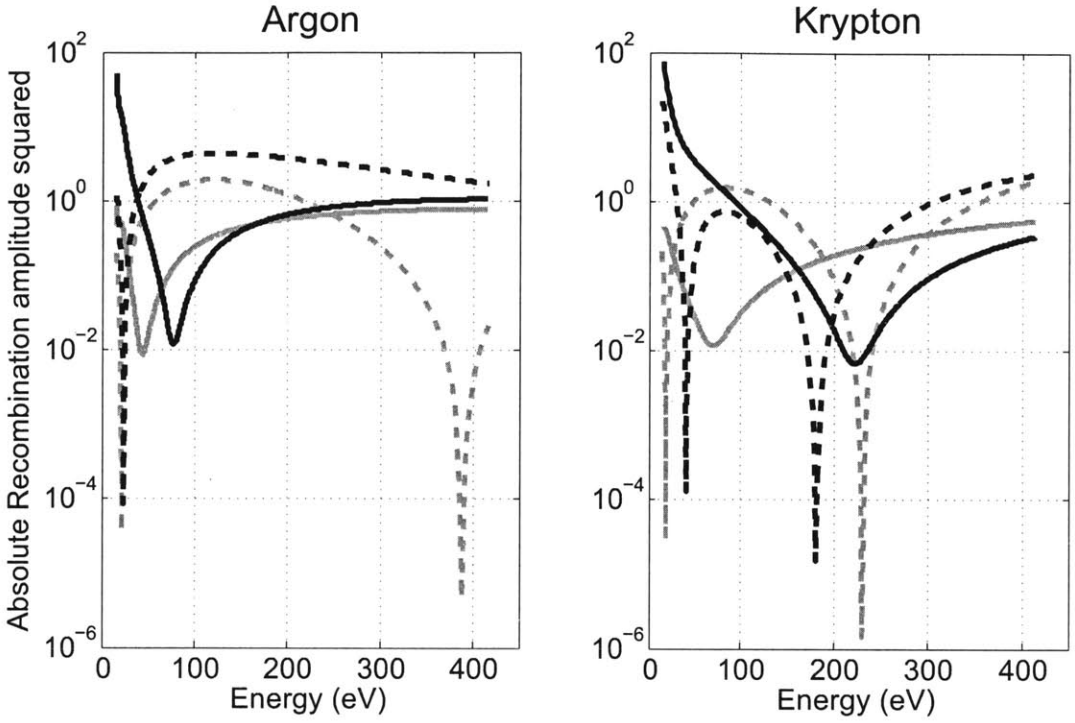

Figure 4-4: Square of absolute values of the Recombination Amplitude of Argon and Krypton for Plane Wave (PW) and Scattering Eigenstate (SC) in Length Form (LF) and Acceleration Form (AF): green dashed (PW-LF), black dashed (PW-AF), green solid (SC-LF) and black solid (SC-AF). In order to compare the length and the acceleration form, the former has been multiplied by w_{gk}^4 (See Equation 4.6)

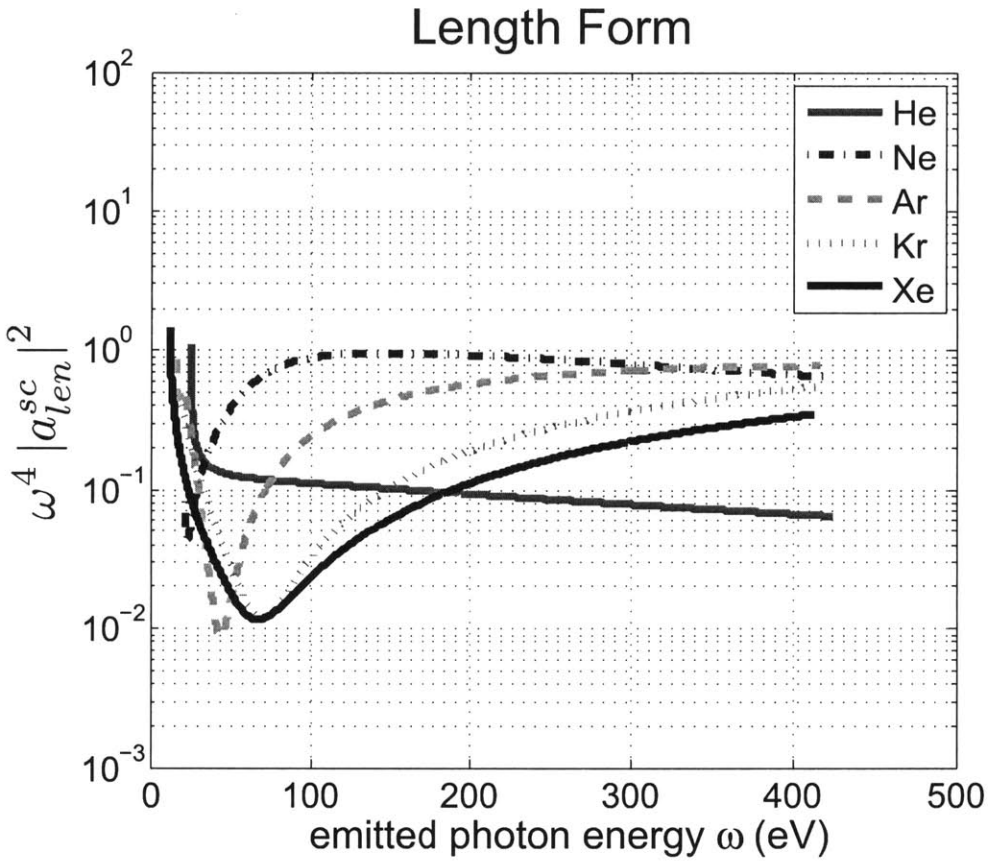

Figure 4-5: Square of the absolute value of the recombination amplitude for outgoing scattering eigenstates in the length form.

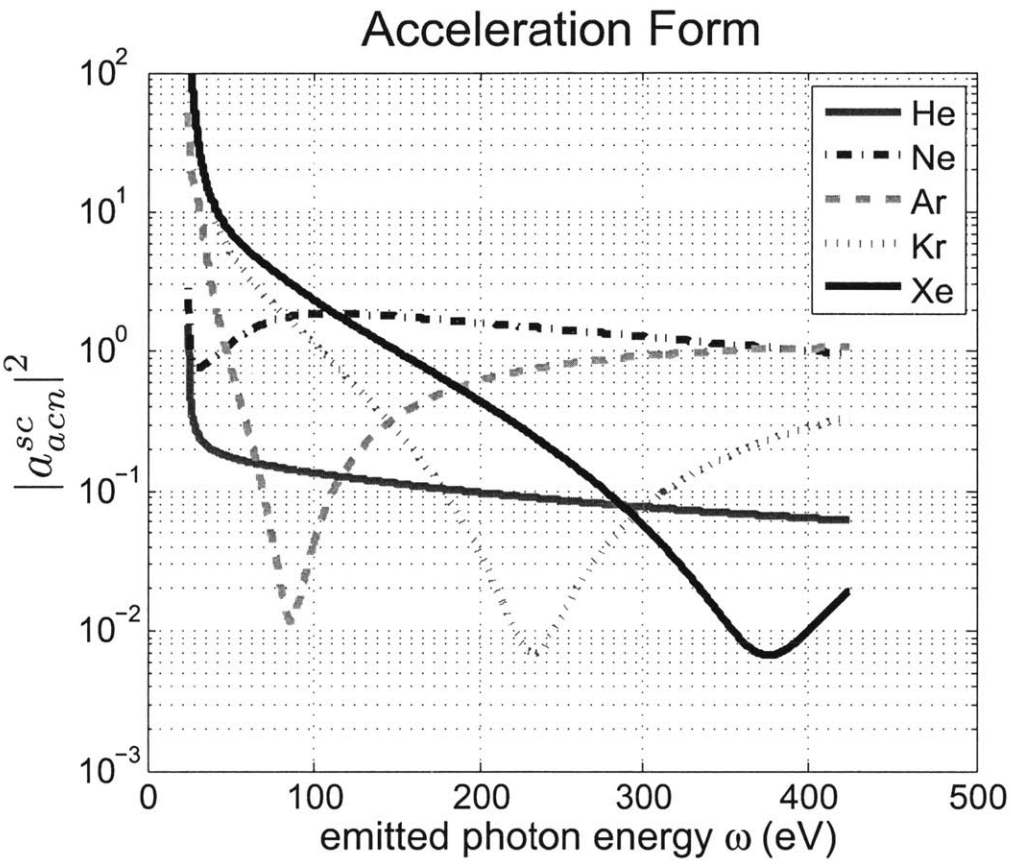

Figure 4-6: Square of the absolute value of the recombination amplitude for outgoing scattering eigenstate in the acceleration form.

4.4 Accuracy of recombination amplitude calculation

In this section, we want to check the accuracy of our calculation of the dipole transition matrix element as shown in Equation 4.13. We want to ensure that the radial wavefunctions u_k^{sc} and u_g; and the partial wave phase shifts δ_l and σ_l have been accurately calculated. In order to do so, we need to compare our results with other single active electron studies in the literature. Since the recombination matrix element is the complex conjugate of the ionization matrix element, our results will be used to calculate photoionization cross section which will be compared with those available in the literature.

Data for *total* photoionization cross section of various elements for selected photon energies is provided in [6]. The *total* photoionization cross section is obtained by integrating the differential photoionization cross section (Equation 2.36) over all solid angles. It is given by [22]

$$\sigma_l^I = \frac{4\pi^2\omega k}{3c(2l+1)} N_{el}\left(l\alpha_{l-1}^2 + (l+1)\alpha_{l+1}^2\right) \tag{4.16}$$

where σ_l^I is the total photoionizaton cross section of the l^{th} orbital, $\alpha_{l+1} = \langle u_g|r|u_{k,l+1}^{sc}\rangle$, $\alpha_{l-1} = \langle u_g|r|u_{k,l-1}^{sc}\rangle$, N_{el} is the total number of electrons in the l^{th} orbital, ω is the photon energy and k is the ionized electron's momentum. It is independent of the azimuthal quantum number m_l because total photoionization is calculated by averaging over all the possible initial states [28]. For $l = 1$ (p orbital), the initial states are $|l = 1, m_l = 0\rangle$, $|l = 1, m_l = 1\rangle$, and $|l = 1, m_l = -1\rangle$. The 3 in the denominator of the prefactor is due to averaging over these three states. The *total* photoionization cross section is independent of the partial wave phase shifts.

The total photionization cross section is the cross section of absorbing a photon and emitting an electron in *any* direction. The *differential* photoionization cross section, which is the cross section of absorbing a photon and emitting an electron in a solid angle Ω_k, is given by:

$$\frac{d\sigma^I_{lm_l}}{d\Omega_k} = \frac{4\pi^2\omega k}{c}\left|c_{l+1}\alpha_{l+1}Y^*_{lm_l}(\Omega_k) + c_{l-1}\alpha_{l-1}Y^*_{lm_l}(\Omega_k)\right|^2 \tag{4.17}$$

where $c_{l\pm1} = \langle Y_{lm_l}|\cos\theta|Y_{l\pm1,m_l}\rangle$ and $Y^*_{lm_l}(\Omega_k)$ is the spherical harmonic. The *total* and the *differential* cross section are related by:

$$\frac{d\sigma^I_{lm_l}}{d\Omega_k} = \frac{\sigma^I_l}{4\pi}(1 + \beta_{lm_l}(\varepsilon)P_2(\cos(\theta_k))) \tag{4.18}$$

where, β_{lm_l} is the energy dependent asymmetry parameter and $P_2(\cos(\theta_k))$ is the second-order Legendre polynomial. The polar angle θ_k is the angle between the laser polarization and the direction of the ejected electron. Due to the dipole approximation Equation 4.18 is independent of the azimuthal angle ϕ. Since we are interested in ionization along the laser polarization, θ_k is set to zero. The asymmetry parameter β_{lm_l}, which depends on the partial wave phase shifts, is given by [73].

$$\beta = \frac{l(l-1)\alpha^2_{l-1} + (l+1)(l+2)\alpha^2_{l+1} - 6l(l+1)\alpha_{l+1}\alpha_{l-1}\cos(\Delta)}{(2l+1)[l\alpha^2_{l-1} + (l+1)\alpha^2_{l+1}]} \tag{4.19}$$

where $\Delta = (\sigma_{l+1} + \delta_{l+1}) - (\sigma_{l-1} + \delta_{l-1})$ is the difference between the partial wave phase shifts. Note that Equation (2) of Ref [cooper zaire] has a an erroneous factor of 3 in the denominator. In order to verify of our recombination amplitude calculation (within single active electron approximation), we need to compare *both* the total photoionization cross section and the asymmetry parameter obtained from our calculation and that provided in [73]. The comparisons are showed for argon, krypton and xenon in Figures 4-7 to 4-12

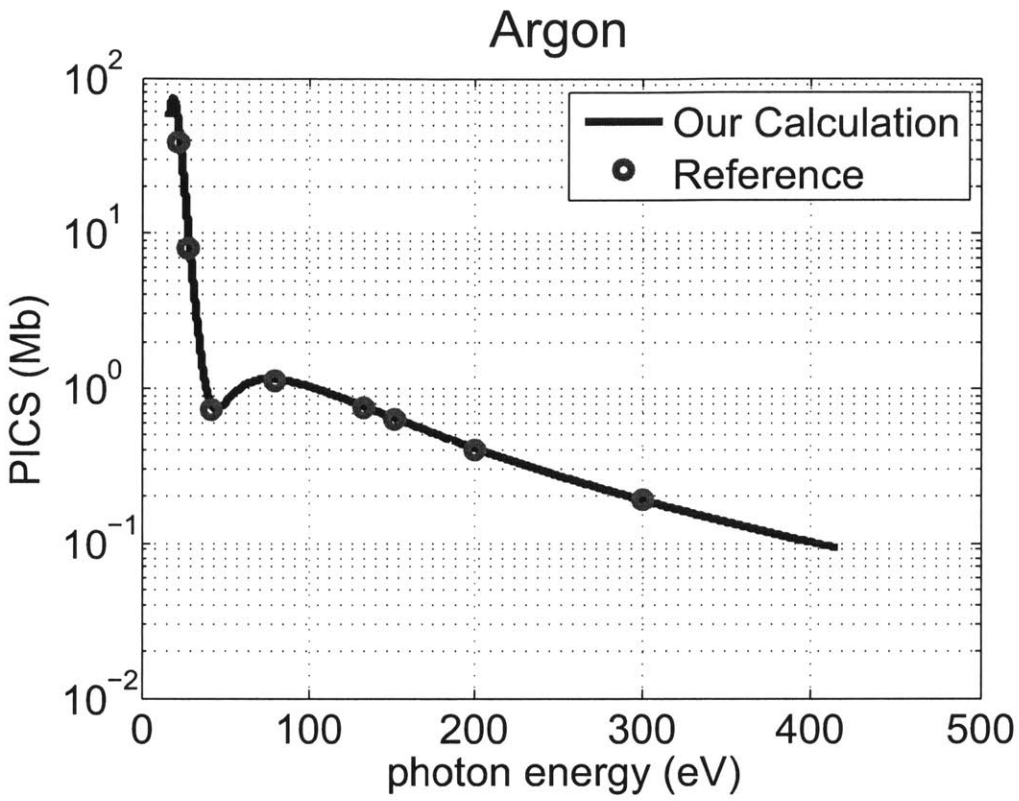

Figure 4-7: The total photoionization cross section of the outermost $l = 1$ orbital of argon. Data from [6] is represented by red circles; our calculation is plotted in a blue line. We get an excellent match. This suggests that our calculations for the radial wavefunctions (u_k^{sc} and u_g) are consistent with [6] (Mb: Megabarns)

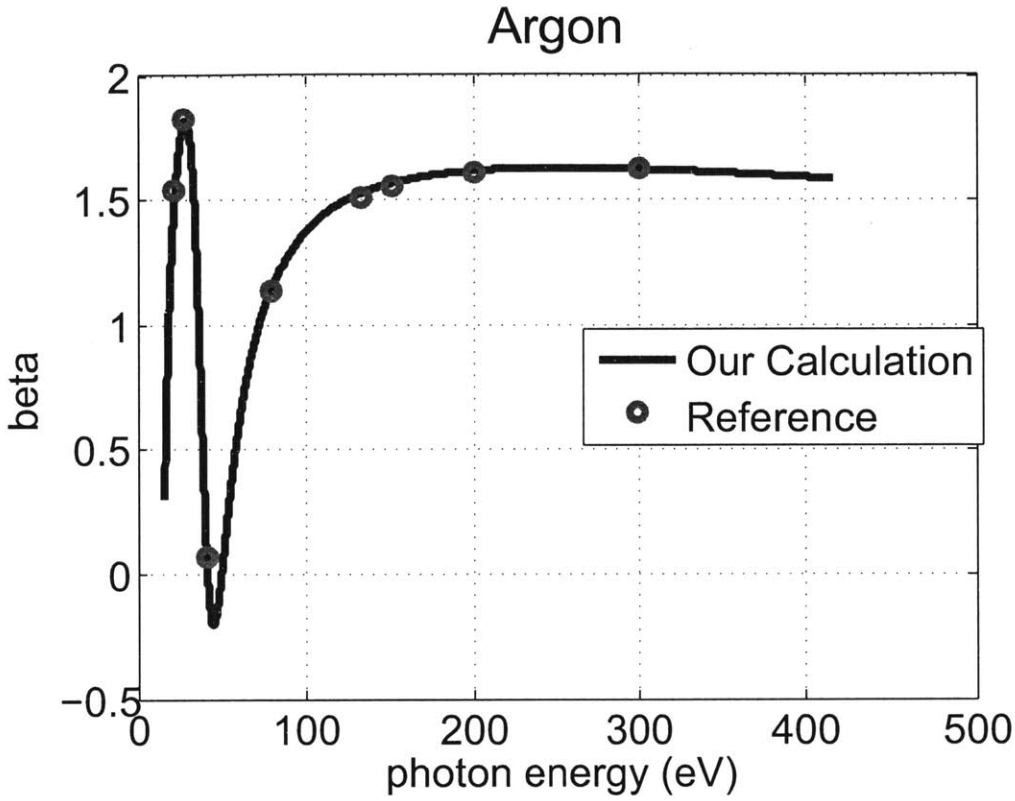

Figure 4-8: The asymmetry parameter (beta) for argon is plotted using the data in [6] (red circles) and compared with our data (a blue line). A very good match is obtained. This suggests that the partial wave phase shift $(\delta_l + \sigma_l)$ is accurately calculated.

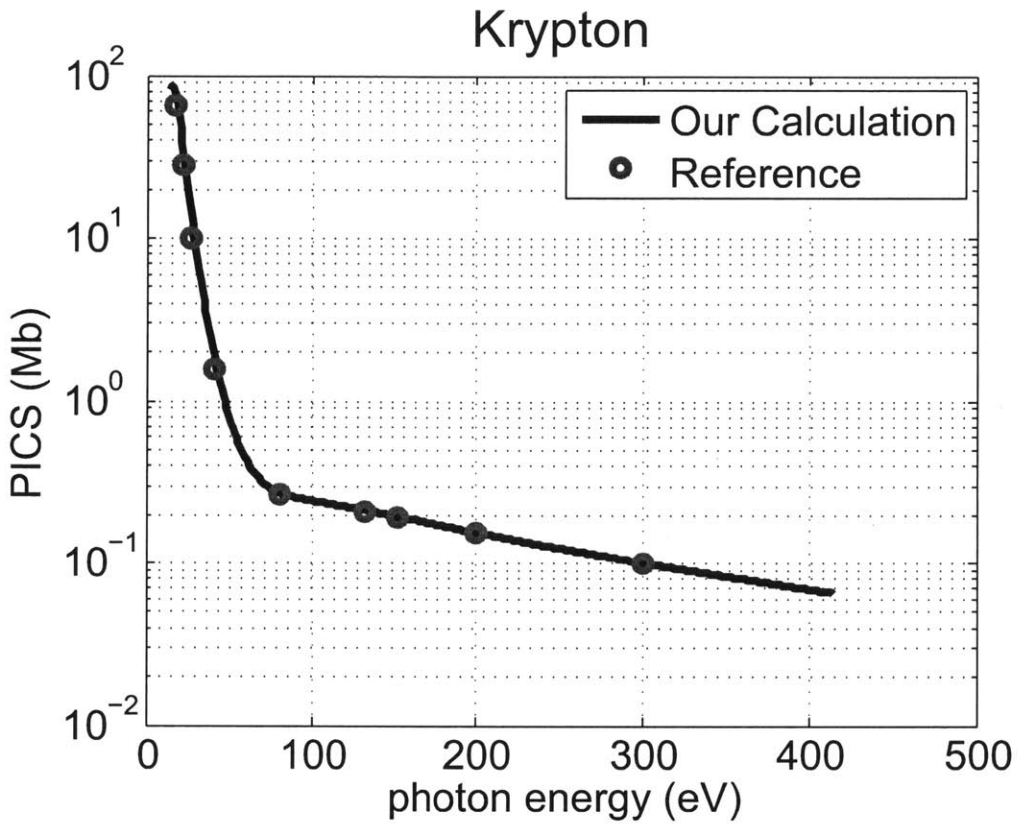

Figure 4-9: The total photoionization cross section of the outermost $l = 1$ orbital of krypton. Data from [6] is represented by red circles; our calculation is plotted in a blue line. We get an excellent match. This suggests that our calculations for radial wavefunctions (u_k^{sc} and u_g) are consistent with [6] (Mb: Megabarns)

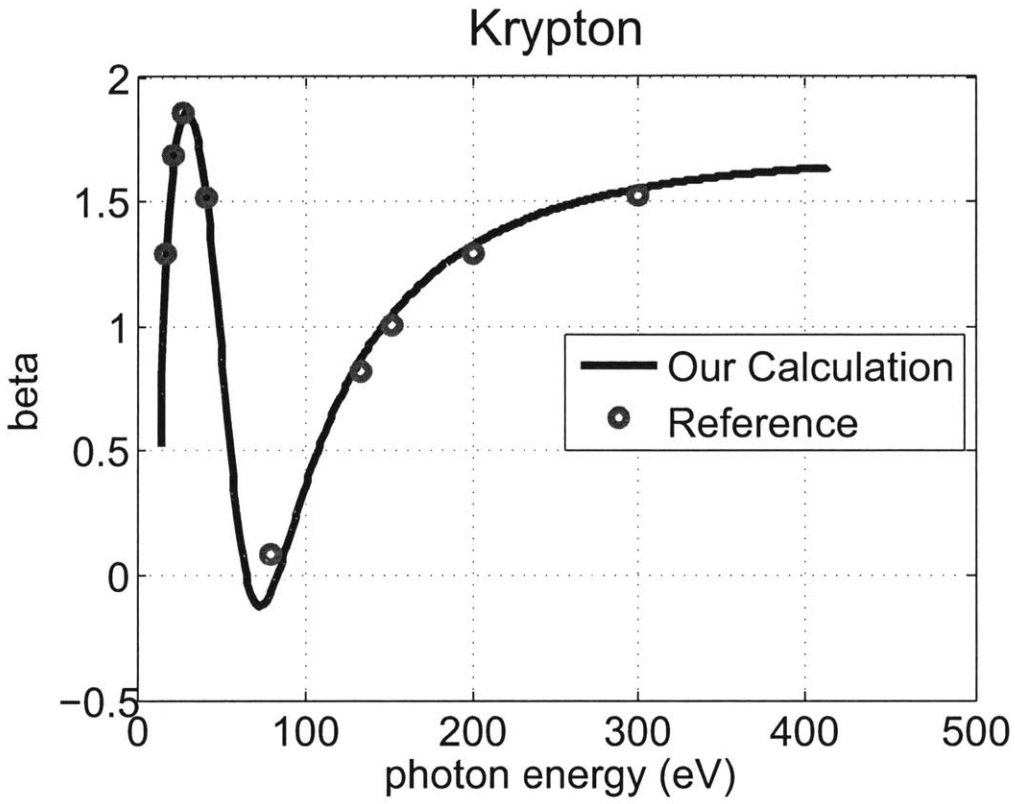

Figure 4-10: The asymmetry parameter (beta) for krypton is plotted (using the data in [6] (red circles) and compared with our data (a blue line). A very good match is obtained. This suggests that the partial wave phase shift $(\delta_l + \sigma_l)$ is accurately calculated.

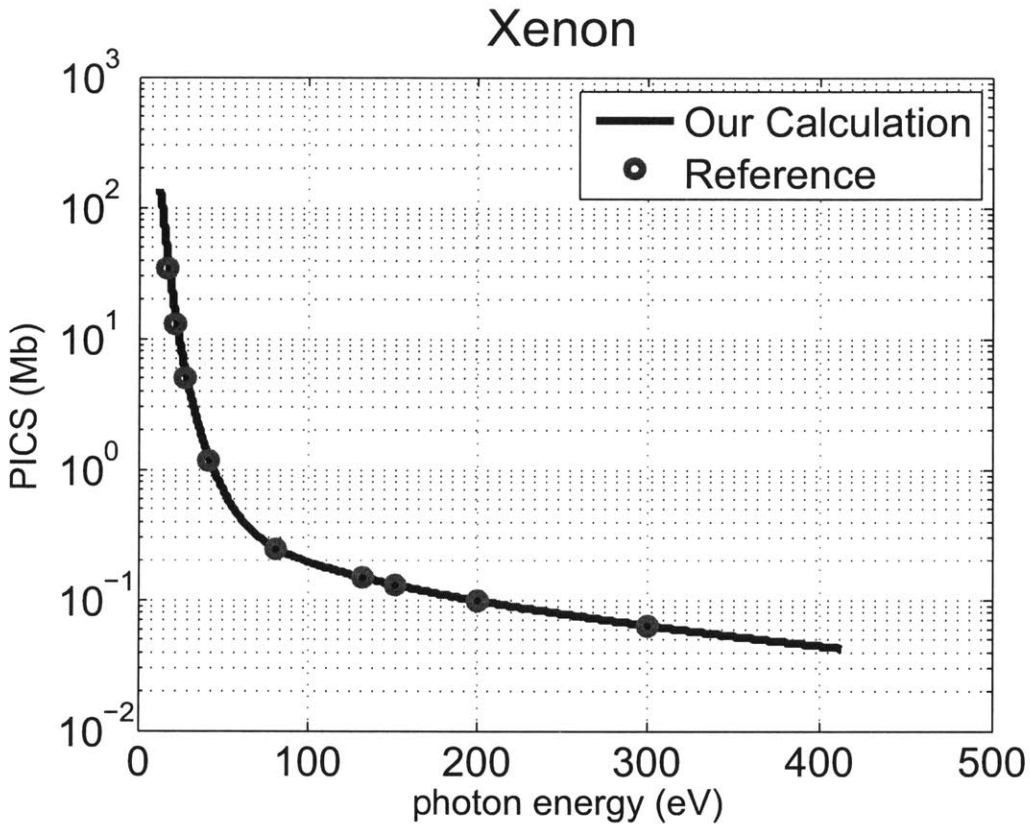

Figure 4-11: The total photoionization cross section of the outermost $l = 1$ orbital of xenon. Data from [6] is represented by red circles; our calculation is plotted in a blue line. We get an excellent match. This suggests that our calculations for radial wavefunctions (u_k^{sc} and u_g) are consistent with [6] (Mb: Megabarns)

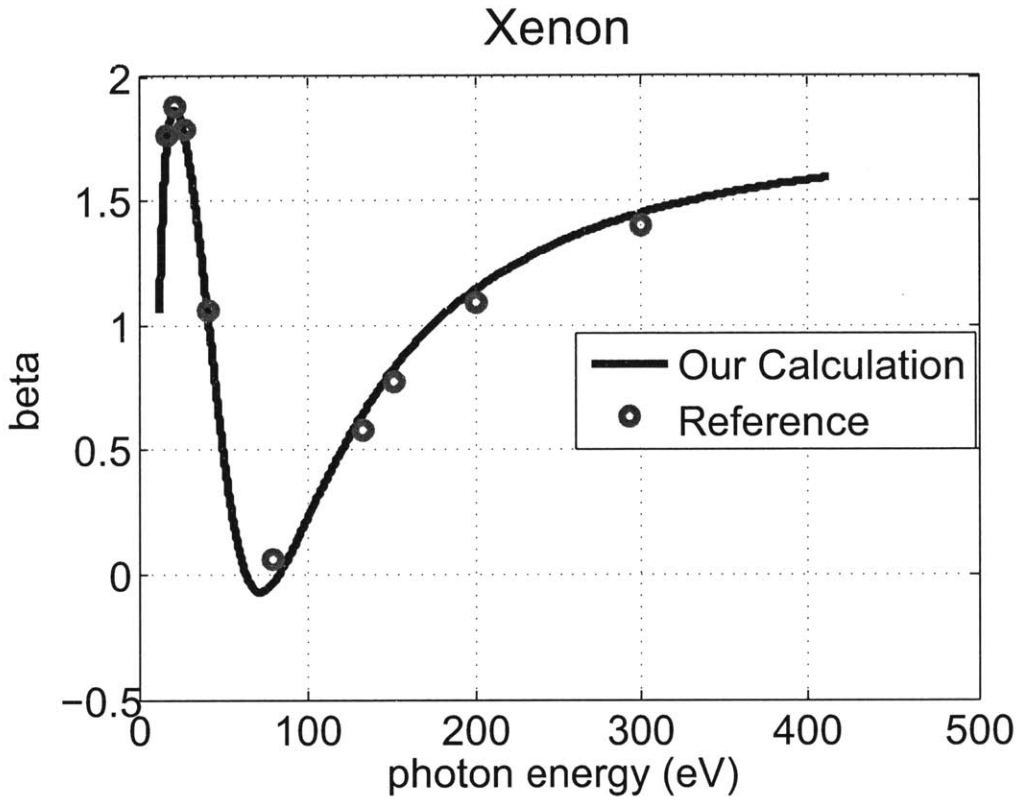

Figure 4-12: The asymmetry parameter (beta) for xenon is plotted using the data in [6] (red circles) and compared with our data (a blue line). A very good match is obtained. This suggests that the partial wave phase shift $(\delta_l + \sigma_l)$ is accurately calculated.

4.5 Validity of the active electron approximation

Since the accuracy of our calculation within the SAEA formalism is established, we next want to investigate the limitations of the SAEA itself. Experimentally, the total PICS of noble gases has been extensively studied [74, 5]. The differential and total PICS has also been measured for 2s and 2p orbitals of Ne [75], and 3s and 3p orbitals of Ar [76]. Theoretical calculation of the total PICS and the asymmetry parameter has been done using non-relativistic random phase approximation (RPA) and RRPA [68]. While RPA is quite successful in the calculation of total PICS, it fails to accurately calculate the partial cross section and the asymmetry parameter where the relativistic effects are important [66]. RRPA, on the other hand, includes correlation effects and relativistic spin-orbit coupling and reproduces the experimentally measured asymmetry parameters [77]. Moreover, it also exhibits form invariance [68]. Therefore, we compare the total photoionization cross section from our theory with that obtained from RRPA [68].

In [68], partial PICS σ_J^I of Ar, Kr and Xe have been calculated, where J is the total angular momentum is a constant of motion in the presence of spin-orbit coupling. Partial PICS calculated using SAEA $\sigma_{lm_l}^I$ are in the $|l, m_l\rangle$ basis where l is the orbital angular momentum and m_l its component along momentum direction. For our purposes, we need to compare, the differential PICS (along the $\theta_k = 0$ direction) in σ_{l,m_l}^I basis $[\partial_{\theta_k=0}(2\sigma_{l=1,m_l=-1}^I + 2\sigma_{l=1,m_l=0}^I + 2\sigma_{l=1,m_l=1}^I)]$ with the differential PICS in σ_J^I basis $[\partial_{\theta_k=0}(\sigma_{J=3/2}^I + \sigma_{J=1/2}^I)]$

The differential PICSs calculated from our model have been compared to the differential PICSs obtained from RRPA in Figure 4-13, Figure 4-14 and Figure 4-15 for Ar, Kr and Xe respectively. PICS calculated using the length form and the RRPA results agree fairly well for Ar and Kr. In the case of Xe, the RRPA predicts the experimentally observed "giant resonance" [19]. Our model, based on SAE and dipole moment in the length and acceleration forms, cannot capture this effects because it does not take into account the inter-channel coupling where the conventional TSM breaks down. This tells us that the TSM with a single active electron, which has

served so well in predicting the qualitative shape of the HHG spectrum, cannot be used in high-harmonic spectroscopy when multi-electron effects become important.

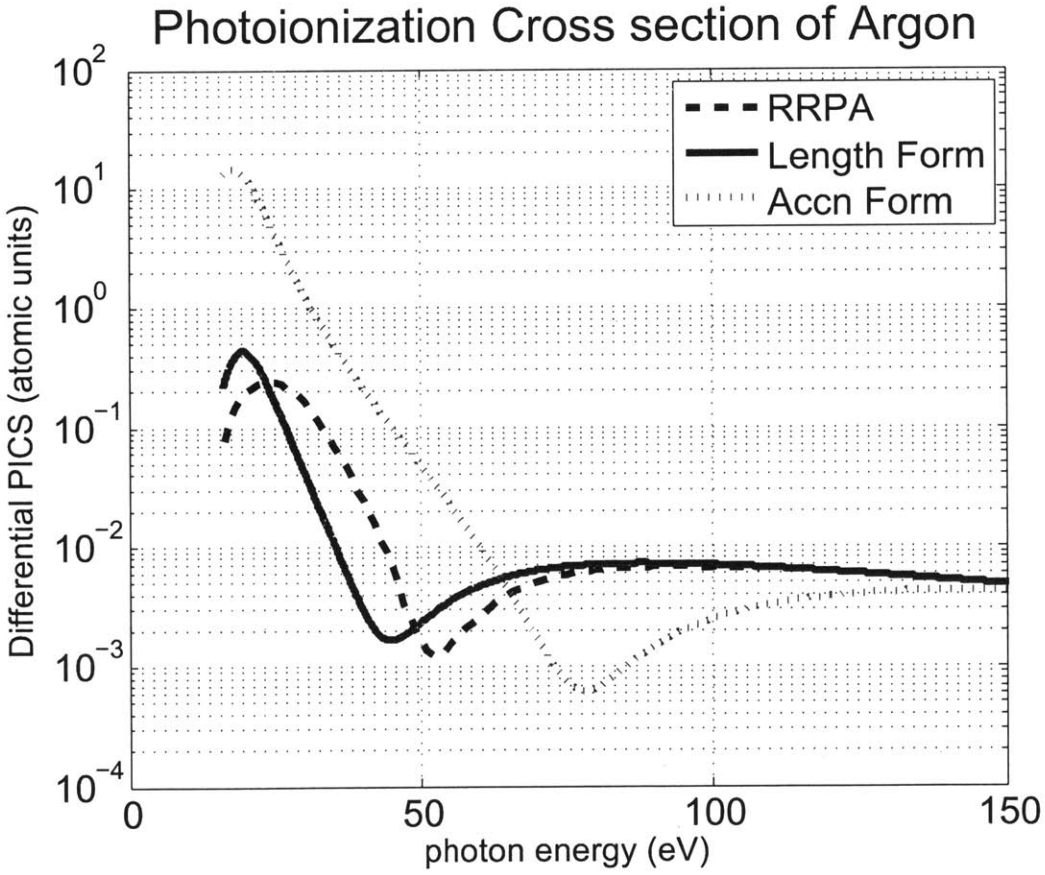

Figure 4-13: Argon's differential Photoionization cross sections (PICSs) calculated using outgoing scattering eigenstates with dipole moment in the length form (solid blue) and the acceleration form (dotted red); and RRPA (dashed black). PICS obtained from the length form is in better agreement with the RRPA calculation ($1a.u^2 = 28Mb$)

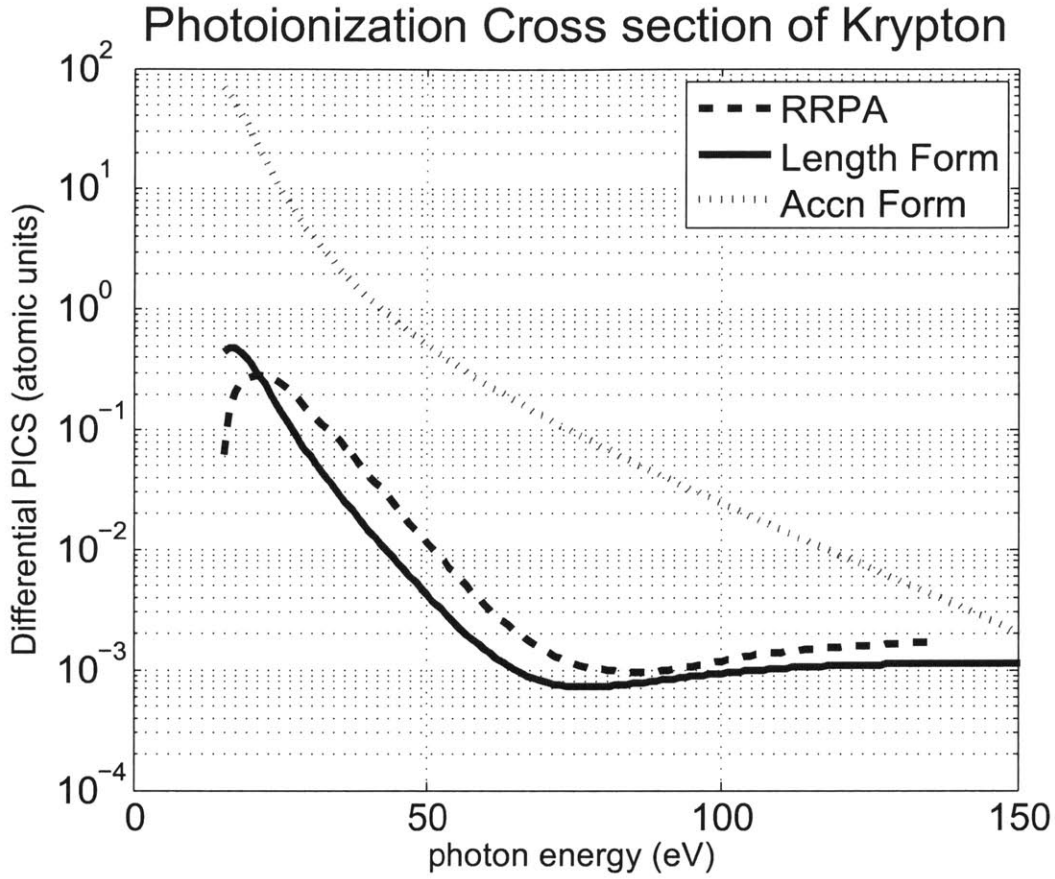

Figure 4-14: Krypton's differential Photoionization cross sections (PICSs) calculated using outgoing scattering eigenstates with dipole moment in the length form (solid blue) and the accelaration form (dotted red); and RRPA (dashed black). PICS obtained from the length form is in good agreement with RRPA calculation in 30 eV to 80 eV range. In the same range, the acceleration form is off by about 4 orders of magnitude ($1a.u^2 = 28Mb$)

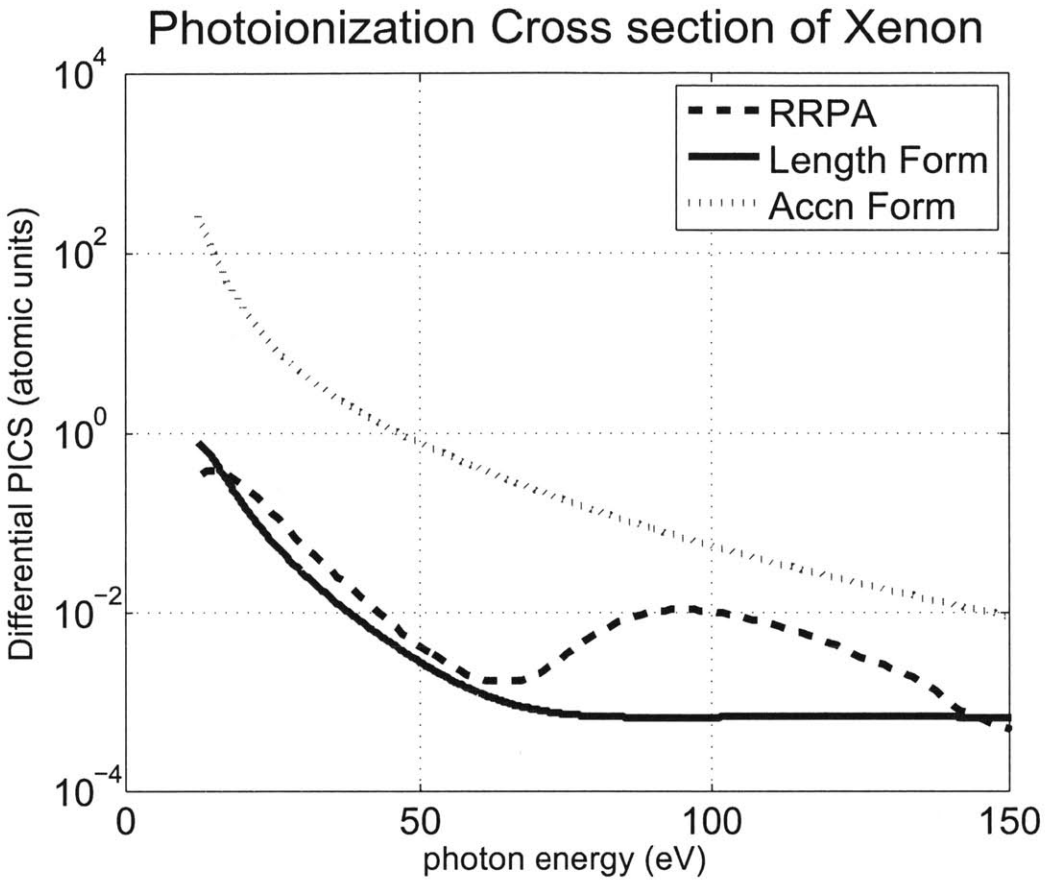

Figure 4-15: Xenon's differential Photoionization cross sections (PICSs) calculated using outgoing scattering eigenstates with dipole moment in the length form (solid blue) and the accelaration form (dotted red); and RRPA (dashed black). PICS obtained from the dipole form is in good agreement with RRPA calculation. In the same range, the acceleration form is off by about 4 orders of magnitude ($1a.u^2 = 28Mb$)

4.6 Photorecombination cross sections

From the recombination amplitude, the photorecombination cross section (PRCS) for recombining into the orbital $|l = 1, m_l = 0\rangle$ ($|l = 0, m_l = 0\rangle$ for He) can be calculated by [27]

$$\frac{\partial \sigma^R_{len}}{\partial \Omega_k \partial \Omega_n} = \frac{4\pi^2 \omega^3}{c^3 k} |a^{sc}_{len}(k)|^2 \tag{4.20}$$

$$\frac{\partial \sigma^R_{acn}}{\partial \Omega_k \partial \Omega_n} = \frac{4\pi^2 \omega}{c^3 k} |a^{sc}_{acn}(k)|^2 \tag{4.21}$$

Here, c is the speed of light, k is the momentum of the returning electron, and ω is the angular frequency of the released photon. Ω_n and Ω_k are solid angles in the direction of polarization of emitted photon and electron momentum respectively. The reverse of the recombination step described in the previous section is the process where a photon with polarization along a solid angle Ω_n ionizes an electron in the polarization direction from the outermost orbital ($|l = 0, m_l = 0\rangle$for He, $|l = 1, m_l = 0\rangle$ for other noble gases). Due to this symmetry, the cross sections of the two processes are related by principle of detailed balancing [34]:

$$\frac{\partial \sigma^R}{\omega^2 \partial \Omega_k \partial \Omega_n} = \frac{\partial \sigma^I}{k^2 c^2 \partial \Omega_k \partial \Omega_n} \tag{4.22}$$

where ω is the photon frequency, and k is the electron momentum and σ^R is the photorecombination cross section and σ^I is the photoionization cross sections respectively. In order to apply the above relation to calculate the PRCS from the total PICS we need (a) the total PICS which is the contribution of the polarization-aligned outermost orbital, and (b) the differential PICS which is the photoionization cross section of emitting an electron in a given solid angle. The differential PICS can be calculated using [19]

4.7 Conclusion

We have calculated the recombination amplitude, in the length and the acceleration form of the dipole operator, for both plane waves and outgoing scattering eigenstates of atomic HFS potential. We have shown that the plane wave approximation fails to predict the Cooper minima of Ar and Kr. However, these features can be reproduced when the outgoing scattering eigenstates with the dipole moment in the length form are used. We have also shown that the dipole moment in the length form is better than the acceleration form in the calculation of recombination amplitude for certain energies depending upon the noble gas. The comparison with the PICS obtained from existing RRPA calculations reveals that the SAE model has its limitations and more sophisticated theoretical tools are needed to explain the HHG spectrum over all energy range.

Chapter 5

Attosecond Pulse Characterization

5.1 Introduction

The development of mode-locking techniques [78] led to the generation of picosecond pulses. Over the years, the pulse duration has been reduced from picoseconds to attoseconds. See Figure 1-1. Advent of ultrashort pulses has enabled the study of ultrafast process that were not accessible before. In these applications, it is important to measure the temporal duration of the pulses. Unlike nanosecond pulses, which can be resolved using photodetectors or oscilloscopes, characterization of ultrashort pulsed requires novel metrology techniques in which the ultrashort pulse - which is the shortest known event - is used to measure itself. Ultrashort pulse metrology can be performed in the time domain where the intensity profile is retrieved [79], or in the time-frequency domain where both the intensity and the phase profile are retrieved [80, 81] [82]

5.2 Ultrashort Pulse Characterization Techniques

The time-domain pulse characterization techniques are based on taking an autocorrelation trace of the optical pulse. This involves splitting the pulse, delaying one with respect to the other and recombining them in a nonlinear crystal to generate second harmonics. By measuring the second harmonic signal on a photodetector as a func-

tion of the delay, and by guessing the shape of the pulse, the optical pulse duration can be retrieved. Development of ultrabroadband sources led to the generation of few-cycle pulses, with pulse duration of less than 5 fs [83]. For such short pulses it is important to know not only the intensity profile but also the electric field. In order to fully characterize optical pulses, i.e., measure both the intensity and the phase profile and therefore reconstruct the electric field, time-frequency retrieval techniques have been developed [80, 81] [82].

The time-frequency retrieval techniques are based on the idea that characterization of a pulse in the frequency domain is equivalent to that in the time domain. Therefore, by measuring both the spectral intensity and the spectral phase, the electric field of the optical pulse can be reconstructed. The time-frequency retrieval techniques can be divided into two broad categories: a)Frequency resolved optical gating (FROG) techniques and b) spectral interferometry technique like SPIDER and 2DSI.

5.2.1 Frequency Resolved Optical Gating

The FROG is an autocorrelation measurement in which the output signal is spectrally resolved by replacing the photodetector by a spectrometer. As a result, instead of an autocorrelation trace a spectrogram is obtained. The expression of the spectrogram is given by:

$$S(\omega,\tau) = \left| \int_{-\infty}^{\infty} P(t)G(t-\tau)e^{-i\omega t}dt \right|^2 \tag{5.1}$$

where $P(t)$ is the optical pulse and $G(t-\tau)$ is the gate function delayed by τ. Since in autocorrelation and FROG, the pulse and the gate function are the electric pulse to be characterized, $P(t)$ is replaced by $E(t)$ and $G(t-\tau)$is replaced by $E(t-\tau)$. Notice that the spectrogram is simply the modulus square of the fourier transform of the product of pulse and gate function $(P(t)G(t-\tau))$. This is crucial, as we will later see, in the efficient implementation of retrieval algorithms. Since the spectrometer measures the intensity spectrum of the second harmonics, Equation 5.1 can be rewritten as:

$$I_{FROG}^{SHG}(\omega,\tau) = \Big| \int_{-\infty}^{\infty} E(t)E(t-\tau)e^{-i\omega t}dt \Big|^2 \tag{5.2}$$

Several variants of FROG that utilize a different nonlinear process, (like third harmonic generation) or geometry exist. In each of these variants, the pulse and the gate function are different, i.e., $E(t)E(t-\tau)$ is replaced by $E(t)|E(t-\tau)|^2$ in polarization gating FROG, $E(t)^2E^*(t-\tau)$ in self-diffraction FROG, and $E(t)^2E(t-\tau)$ in third harmonic generation FROG [84].

From the intensity spectrogram, the pulse and the gate pulse can be retrieved using the principle components generalized projections algorithm (PCGPA) [85] or the standard least square generalized projection algorithm (LSGPA) [7]. These are iterative-fourier-transform based algorithms that involve guessing the pulse and the gate functions in the time domain, generating a spectrogram by numerical integration of Equation 5.2, forcing the intensity of the spectrogram to be that of the experimentally measured spectrogram and retrieving the new pulse and gate function using the least squares method (for LSGPA) or the power method (for PCGPA). These iterations are continued until the solutions of the pulse and the gate functions converge. A summary of the retrieval algorithm is shown in Figure 5.3. Since the expression of the spectrogram (Equation 5.1) looks like a fourier transform, fast FFT methods can be applied at every iterative step. This helps in significantly speeding up the retrieval algorithm.

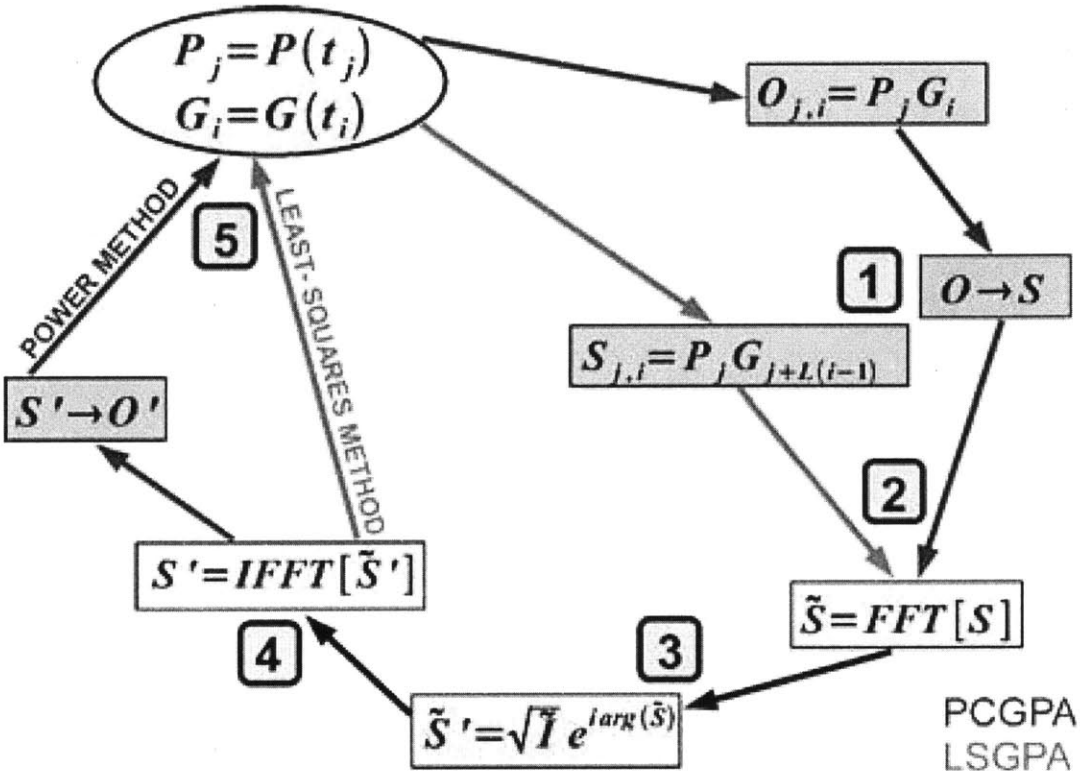

Figure 5-1: LSGPA and PCGPA retrieval algorithm. *Step 1*: Guess the pulse and the gate in the time domain and multiply the two for various delays. *Step 2*: Generate a spectrogram by taking a fast fourier transform of the result from Step (1). *Step 3*: Force the magnitude of the spectrogram to match that either the measured spectrogram or the spectrogram obtained through numerical integration. *Step 4*: Take the inverse fourier transform of the spectrogram. *Step 5*: Use the Least Square method for LSGPA or Power method for PCGPA to obtain the pulse and the gate terms. Repeat *Steps 1-5* till convergence is achieved. This figure is taken from [7]

5.2.2 Spectral Interferometric techniques

The spectral interferometric techniques like spectral phase interferometry for direct electric-field reconstruction (SPIDER) [80] and two-dimensional spectral shearing interference [82] determine the spectral phase by the interference of spectral components separated by a shearing frequency. Spectral interferometric techniques do not require the generation of a spectrogram and the retrieval algorithm is non-iterative and therefore fast. On the flip side, spectral interferometric techniques require a very well characterized reference pulse.

SPIDER is a self-referencing technique where the optical pulse is split into three copies: one copy is chirped and therefore stretched; the other two copies are delayed by τ with respect to each other and then recombined with the stretched pulse. It is important for the chirped pulse to be long enough so as to overlap both the two delayed pulses. The superposition of the three pulses is sent through a nonlinear crystal. See Figure 5.2.2. The delayed pulses overlap with different frequencies of the chirped pulse, and therefore different frequency shifts due to the interaction with the crystal. The frequency shift of the spectrum of one pulse with respect to the other is referred to as spectral shearing. For a delay τ and a spectral shearing Ω, the intensity profile is

$$I^{SP}(\omega, \tau) = \left|\mathcal{E}(\omega) + \mathcal{E}(\omega + \Omega)e^{i\omega\tau}\right|^2. \tag{5.3}$$

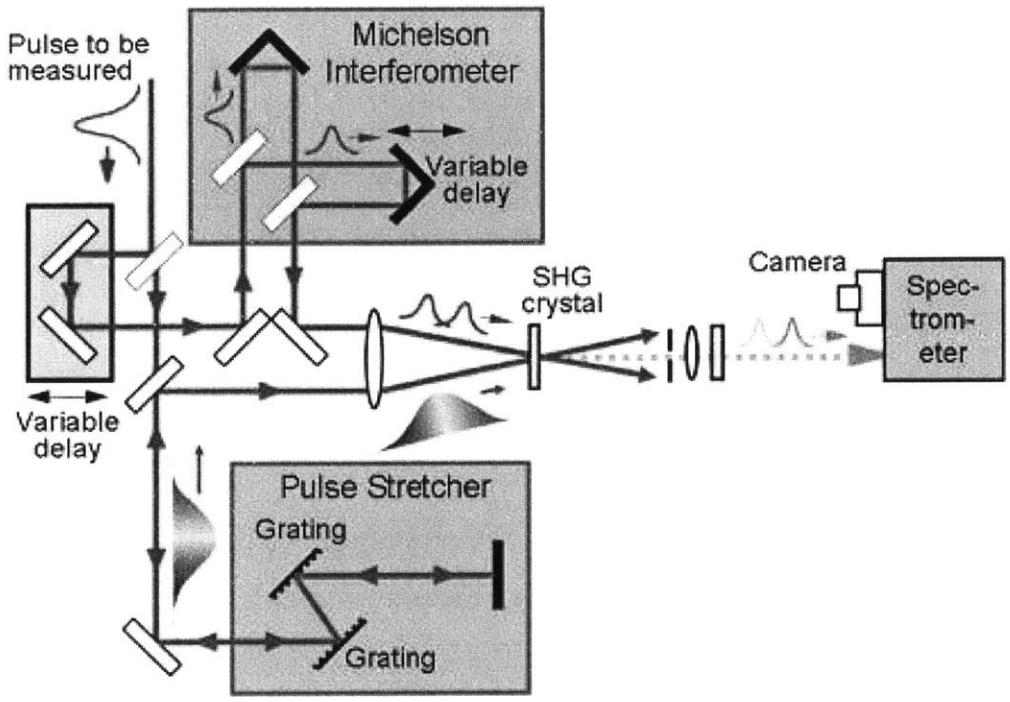

Figure 5-2: Experimental setup of SPIDER. The pulse to be measured is split in two copies. The first copy is chirped by sending it through a pulse stretcher. The second copy is split into two pulses which are delayed with respect to each other. The three copies are combined in a SHG crystal. The second harmonic spectrum is measured using a spectrometer The figure is taken from *http* : *//www.swampoptics.com*

5.3 Attosecond Pulse Characterization techniques

The advent of high-order harmonic generation led to the generation of extreme ultraviolet (EUV) pulses with attosecond pulse duration [86]. The pulse retrieval techniques, which worked well for femtosecond pulses, could not be used for attosecond pulses. The reason being that unlike femtosecond pulses, whose intensities are strong enough to produce second harmonics , intensities of attosecond pulses are very low. Therefore, attosecond pulse characterization needs to rely on the interaction of low intensity EUV radiation with matter. The natural candidate for such an interaction is the photoionization process which had been studied for decades [71, 22]. Like FROG, where the amplitude and phase information of the optical pulse is transferred to the intensity spectrogram of the second harmonic, the amplitude and phase information of the attosecond pulse is transferred to the photoelectron spectrum. The photoionization step occurs in the presence of an IR which acts like a phase modulator: the phase of the photoelectron wavepacket oscillates as the delay between the two pulses is varied. A spectrogram is constructed by measuring the photoelectron energy spectrum as a function of the delay. From the spectrogram, the attosecond pulse is retrieved by fitting the experimental data with a model function of the ionization and the streaking processes [87, 88, 89, 90, 7].

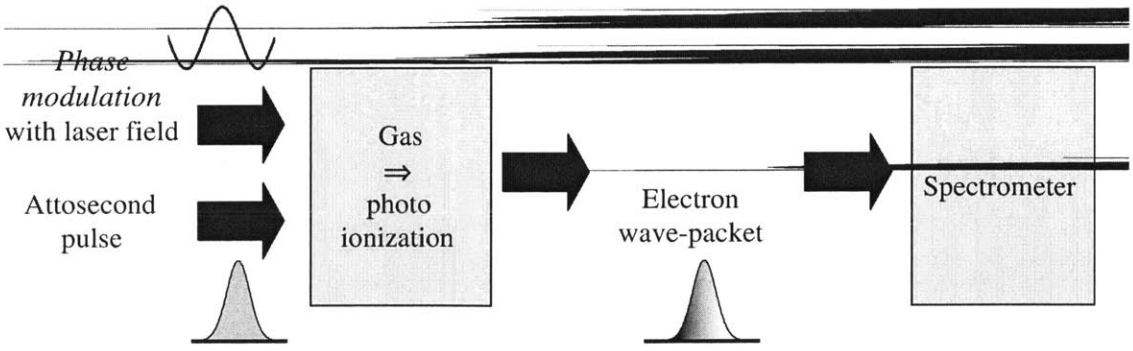

Figure 5-3: General scheme of attosecond metrology experiment. A superposition of attosecond pulse and IR pulse generates an electron wavepacket by photoionizing gas atoms. The energy distribution of the electron wavepacket is measured by a time of flight spectrometer. Figure is taken from [8]

The EUV attosecond pulse characterization is a two step process: a) generation of a spectrogram and (b) retrieval of the EUV pulse (and the IR in some cases) from the spectrogram. The spectrogram is experimentally obtained by splitting the IR pulse; the first copy (called the drive) generates the attosecond pulse; the second copy is delayed using a time delay stage; finally the attosecond pulse and the delayed IR pulse are combined. The drive pulse is blocked using a filter. See Figure 5.3.

For the purpose of analysis, the spectrogram can also be numerically generated either by solving the time-dependent schrödinger equation of the interaction of an atom by a superposition of an attosecond and an IR pulse, or by integrating a simplified model function such as the one given in Equation 5.4. The spectrogram is then used in a retrieval algorithm to obtain the attosecond pulse (and sometimes the IR pulse). A good way to test the accuracy of a retrieval algorithm is to retrieve the EUV pulse from a numerically generated spectrogram and then compare it with the EUV pulse used to generate the spectrogram.

Several attosecond pulse characterization techniques have been developed [87, 88, 89, 90]. Attosecond pulse characterization techniques can broadly be divided into two categories: (a) streaking techniques like frequency resolved optical gating for complete reconstruction of attosecond bursts (FROG-CRAB); b) perturbative techniques like Reconstruction of attosecond harmonic beating by interference of two-photon transitions (RABBITT) [88], phase retrieval by omega oscillation filtering (PROOF) [89] and the improved-PROOF (iPROOF) [90]. These techniques are an extension of the femtosecond pulse characterization techniques. In fact, as we will see in this chapter, a concerted effort has been made - sometimes at the cost of accuracy of the retrieval algorithm - to ensure that the expression for photoelectron distribution in the FROG-CRAB resembled the expression for the intensity of second harmonics in FROG. The streaking and perturbative attosecond characterization techniques differ only by the IR intensity and the model function used in the retrieval algorithm.

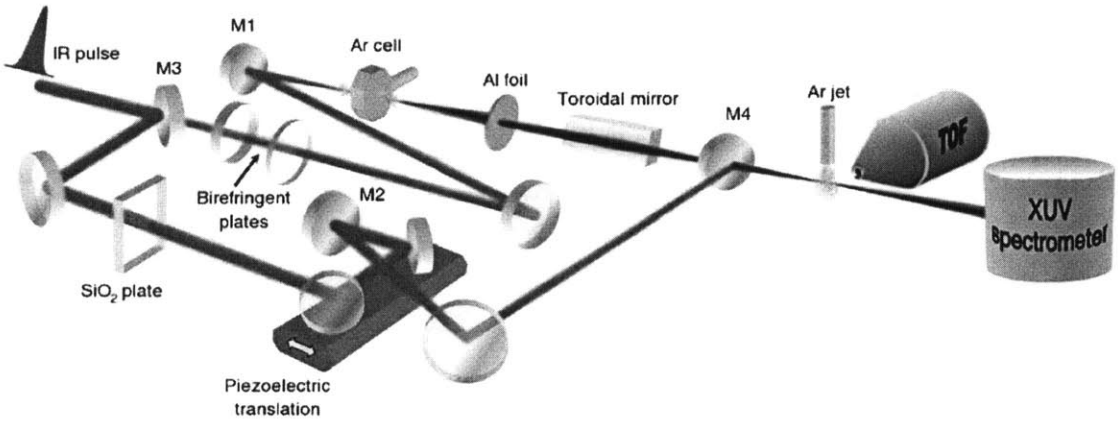

Figure 5-4: Experimental setup for attosecond pulse characterization. The IR pulse is split into two parts. One part, called the drive is used to produce the attosecond pulse through high-order harmonic generation process in argon. The aluminum foil selectively blocks the drive pulse. The second part, called the streak pulse is delayed using a piezoelectronic translation stage and then recombined with the attosecond pulse using a drilled mirror. The superposition of the streak pulse and the attosecond pulse is shone on a jet of argon atoms. The energy distribution of the photoelectrons generated through this interaction is measured by the time of flight (TOF) spectrometer.

5.3.1 FROG-CRAB

The FROG-CRAB characterization is based on the *simplified* version of the strong field approximation (SFA) where the photoelectron and the attosecond pulse spectra are related by only an energy shift equal to the ionization potential of the gas. In other words, the photoionization process acts like a filter which downshifts the spectrum of the attosecond pulse by the ionization potential of the atom The bound state of the electron is a field-free atomic eigenstate and the continuum state is a Volkov state. (A volkov state is the eigenstate of a free electron in an electric field.) In spite of being several orders of magnitude weaker than the IR pulse, the attosecond pulse photoionizes the bound electrons. The reason being that a single EUV photon can ionize the outermost electron as opposed to several IR photons that are needed for photoionization. For a given delay τ between the EUV pulse and the IR pulse , the probability of detecting an electron with final momentum k is [8]. (The details of

the derivation of Equation 5.4 is provided in Chapter 2)

$$P(k,\tau) = \left| \int_{-\infty}^{\infty} dt e^{-i\varphi(k,t)} d^V_{\mathbf{k}+\mathbf{A}(t)} E_X(t-\tau) e^{i(W+I_p)t} \right|^2. \tag{5.4}$$

Here, $E_X(t-\tau)$ is the delayed EUV pulse and $W = k^2/2$ is the kinetic energy of the photoelectron, and $d^V_{\mathbf{k}+\mathbf{A}(t)} = \langle \mathbf{k}+\mathbf{A}(t)|z|\psi_g\rangle$ is the Volkov transition matrix element . The IR dependent phase modulation term is given by:

$$\varphi(t) = \int_t^{\infty} dt'(kA(t') + \frac{A^2(t')}{2}) \tag{5.5}$$

For an IR laser field $E_L(t) = E_0(t)\cos(\omega_L t)$, $\varphi(t)$ can be written as

$$\varphi(k,t) = \varphi_1(t) + \varphi_2(t) + \varphi_3(t) \tag{5.6}$$

where

$$\varphi_1(t) = \int_t^{\infty} dt' U_p(t') \tag{5.7a}$$

$$\varphi_2(t) = -\frac{2k\sqrt{U_p(t)}}{\omega_L}\cos(\omega_L t) \tag{5.7b}$$

$$\varphi_3(t) = \frac{U_p(t)}{2\omega_L}\sin(2\omega_L t) \tag{5.7c}$$

where

$$U_p(t) = \frac{E_0(t)^2}{4\omega_L^2} \tag{5.8}$$

is the ponderomotive potential.

In the FROG-CRAB retrieval algorithm, two assumption are made to simplify Equation 5.4. First the volkov dipole transition matrix element $d^V_{\mathbf{k}+\mathbf{A}(t)}$ is set to one. Second, the momentum k in the phase modulation term (Equation 5.5) is replaced by k_0, the central momentum of the photoelectron spectrum. This is referred to as the central momentum approximation. These approximations allow the expression of the photoelectron distribution (Equation 5.4) to be written as a fourier transform:

$$P(k,\tau) = \left| \int_{-\infty}^{\infty} dt e^{-i\varphi(k_0,t)} E_X(t-\tau) e^{i(W+I_p)t} \right|^2. \tag{5.9}$$

Equation 5.9 resembles the expression of the FROG spectrogram (see Equation 5.1) where $E_X(t)$ is the pulse and $e^{-i\varphi(k_0,t)}$ is the gate. As a result, the retrieval algorithms that are used in FROG can be used here. Actually, the motivation behind making the approximations was to ensure that the already existing FROG algorithms could be used.

The gate term $e^{-i\varphi(k_0,t)}$ acts like a time-domain phase modulator. To understand the effect of this phase modulation, the phase is expanded around the delay τ:

$$\varphi(k_0,t) = \varphi(k_0,\tau) + \varphi'(k_0,\tau)(t-\tau) + \frac{1}{2}\varphi''(k_0,\tau)(t-\tau)^2 \cdots \tag{5.10}$$

As we know from well known fourier properties, the first-order derivative of the phase modulation term ($\varphi'(k_0,\tau)$) will result in a frequency shift and the second-order derivative ($\varphi''(k_0,\tau)$) will change the width of the photoelectron spectrum. Next, the first- and the second-order effects are analyzed by taking the first and second derivative of Equation 5.6. For simplicity it is assumed that the IR field is sinusoidal and therefore the time-dependence of $E_0(t)$ (and hence the time dependence of the ponderomotive potential) is dropped. The first-order term is

$$\varphi'(k_0,\tau) = U_p + 2k_0\sqrt{U_p}\sin(\omega_L\tau) + U_p\cos(2\omega_L\tau). \tag{5.11}$$

Typically, the U_p term is much smaller than the kinetic energy of the photoelectron. The ponderomotive potentials for 800nm IR fields with intensities 10^{11} W/cm^2, 10^{12} W/cm^2 and 10^{13} W/cm^2, are 0.006 eV, 0.059 eV and 5.329 eV respectively. These are much smaller than the typical photoelectron energies. Therefore

$$\varphi'(k_0,\tau) \approx 2k_0\sqrt{U_p}\sin(\omega_L\tau) \tag{5.12}$$

The spectral shift is a sinusoidal function of delay τ and oscillates with the IR frequency. Now applying the same analysis on the second-order term, we get:

$$\varphi''(k_0, \tau) \approx 2k_0\omega_L\sqrt{U_p}\cos(\omega_L\tau) \tag{5.13}$$

To illustrate the effects of the first- and second-order effects of the phase modulator, photoelectron spectrograms are calculated by integrating Equation 5.4 for Argon. Two transform-limited EUV pulses, centered at 45 eV and 105 eV, generate a photoelectron wavepacket whose central energy is downshifted by 15 eV - the ionization potential of argon . 800 nm IR pulses with peak intensity of 10^{12} W/cm^2 and 10^{14} W/cm^2 are used to streak the electron wavepacket. The volkov dipole transition matrix element is set to 1. Since the spectrograms are generated through numerical integration, the central momentum approximation is *not* used in generating the spectrum.

The modulation of the central energy of the photoelectron pulse (as a function of EUV-IR delay) is proportional to the central energy of the EUV pulse and the streak intensity of the IR pulse. This is in tune with Equation 5.12. Also, as predicted by Equation 5.13, the full width half maximum of the photoelectron spectrum becomes more prominent for higher IR intensity.

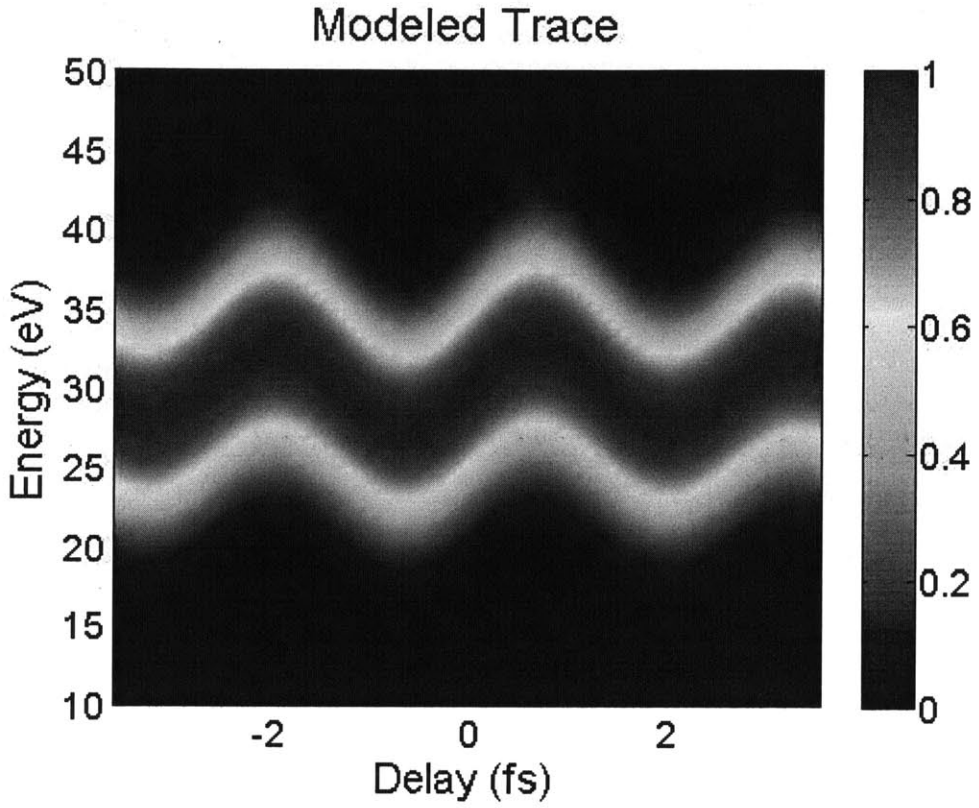

Figure 5-5: Photoelectron spectrogram obtained by numerical integration of Equation 5.4. The gas used is argon ($I_p \approx 15$ eV). The EUV pulse is transform limited, centered at 45 eV with a $\cos^2$ shape and spectral extent of 30 eV. The streaking IR pulse has a duration of 8 fs, is centered at 800 nm and has a peak intensity of 5×10^{11} W/cm^2

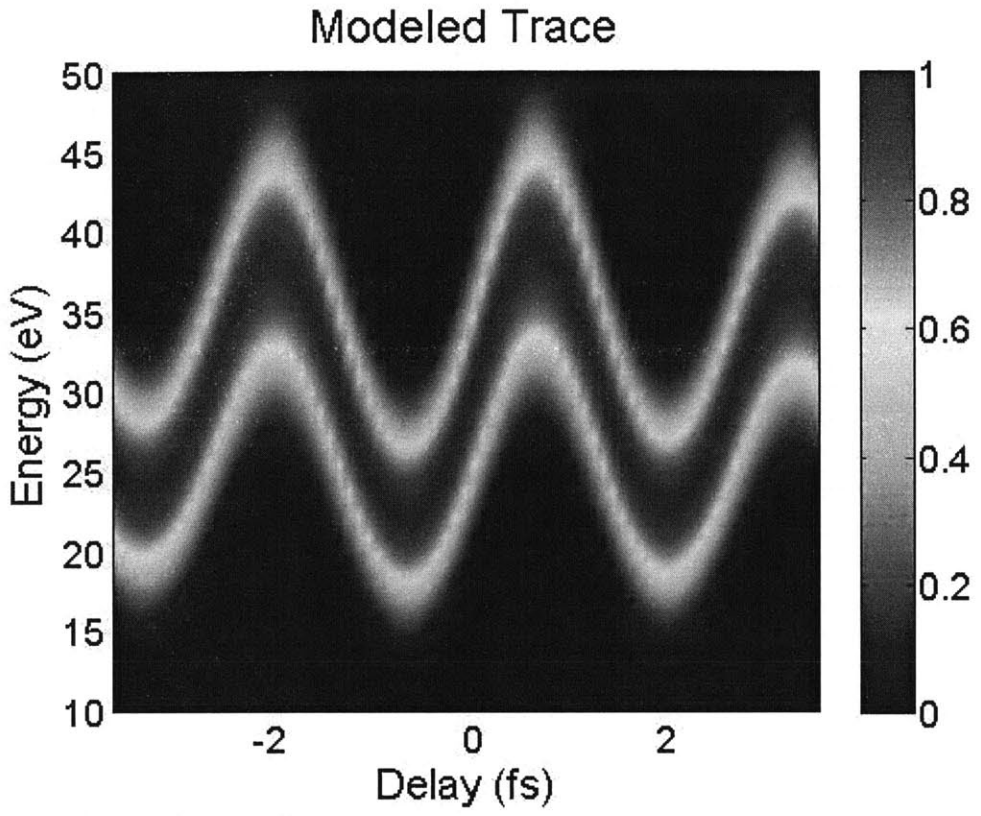

Figure 5-6: Photoelectron spectrogram obtained by numerical integration of Equation 5.4. The gas used is argon ($I_p \approx 15$ eV). The EUV pulse is transform limited, centered at 45 eV with a $\cos^2$ shape and spectral extent of 30 eV. The streaking IR pulse has a duration of 8 fs, is centered at 800 nm and has a peak intensity of 5×10^{12} W/cm^2

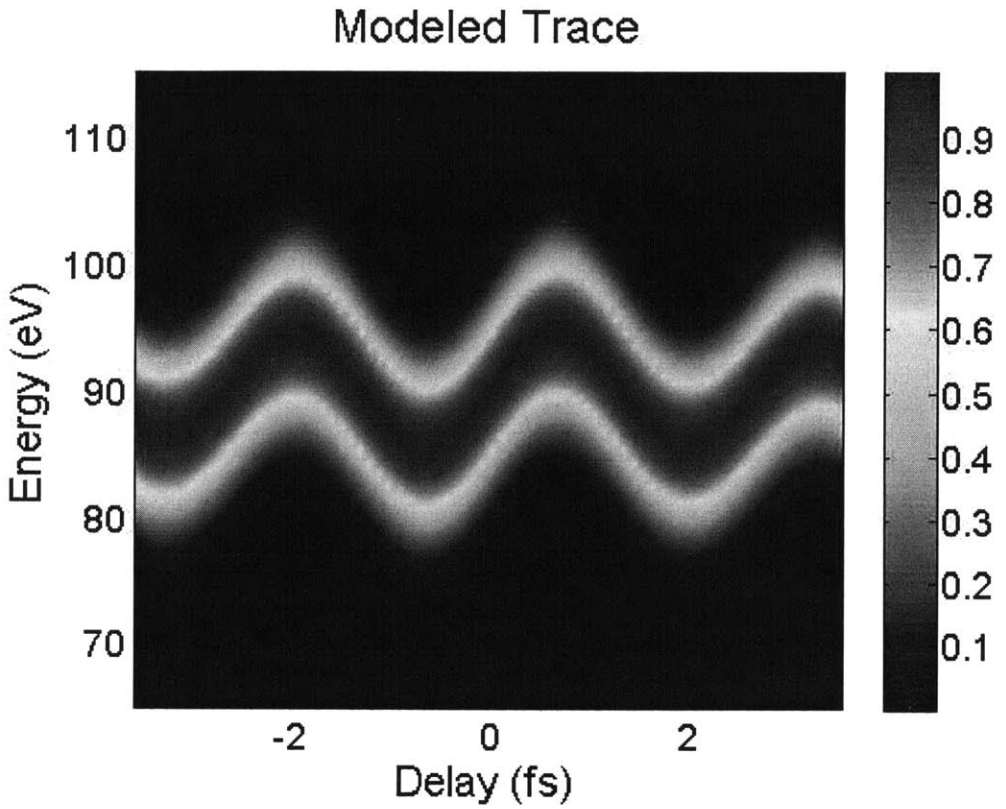

Figure 5-7: Photoelectron spectrogram obtained by numerical integration of Equation 5.4. The gas used is argon ($I_p \approx 15$ eV). The EUV pulse is transform limited, centered at 105 eV with a $\cos^2$ shape and spectral extent of 30 eV. The streaking IR pulse has a duration of 8 fs, is centered at 800 nm and has a peak intensity of 5×10^{11} W/cm^2

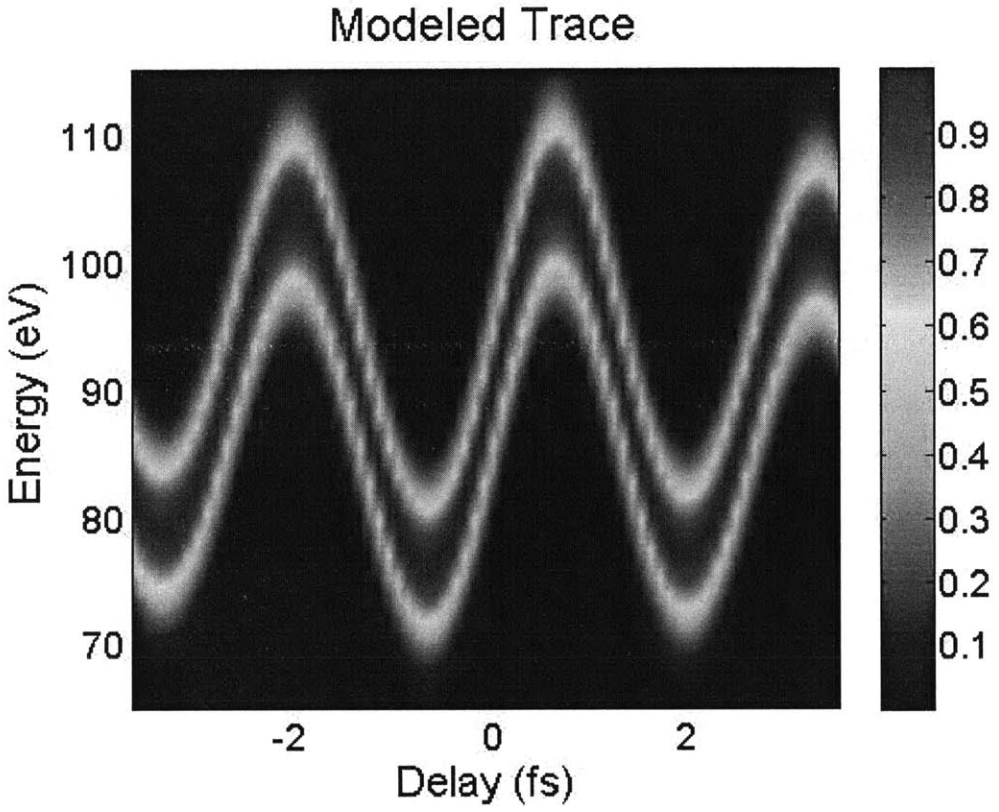

Figure 5-8: Photoelectron spectrogram obtained by numerical integration of Equation 5.4. The gas used is argon ($I_p \approx 15$ eV). The EUV pulse is transform limited, centered at 105 eV with a $\cos^2$ shape and spectral extent of 30 eV. The streaking IR pulse has a duration of 8 fs, is centered at 800 nm and has a peak intensity of 5×10^{12} W/cm^2

5.3.2 PROOF

The pulse duration of shortest attosecond pulses reported has steadily declined and therefore the spectra have become broader. As the ratio of the attosecond pulse bandwidth to the central momentum increases, the central momentum approximation, used in FROG-CRAB, is no longer valid. Phase retrieval by omega oscillation filtering (PROOF) works without the central momentum approximation. If the EUV pulse is centered at high energies then Equation 5.6 is approximated by

$$\varphi(k,t) \approx -\frac{2k\sqrt{U_p}}{\omega_L}\cos(\omega_L t) = -\frac{k\sqrt{U_p}}{\omega_L}\left(e^{i\omega_L t} + e^{-i\omega_L t}\right) \tag{5.14}$$

Additionally, if $k\sqrt{U_p} << \omega_L$ then

$$e^{-i\varphi(k,t)} \approx 1 - i\varphi(k,t) = 1 + i\frac{2k\sqrt{U_p}}{\omega_L}\left(e^{i\omega_L t} + e^{-i\omega_L t}\right) \tag{5.15}$$

When the expression for the approximate phase modulator is inserted in the expression of the photoelectron spectrum (Equation 5.4) we get

$$P(k,\tau) = \left| \int_{-\infty}^{\infty} dt \left(1 + i\frac{k\sqrt{U_p}}{\omega_L}\left(e^{i\omega_L t} + e^{-i\omega_L t}\right)\right) E_X(t-\tau)e^{i(W+I_p)t} \right|^2 . \tag{5.16}$$

Writing the attosecond pulse in the frequency domain $\mathcal{F}(E_X(t)) = \mathcal{E}_X(\omega)$, and using some standard fourier properties:

$$\mathcal{F}(E_X(t-\tau)) = \mathcal{E}_X(\omega)e^{i\omega\tau} \tag{5.17a}$$

$$\mathcal{F}(E_X(t-\tau)e^{i\omega_L t}) = \mathcal{E}_X(\omega+\omega_L)e^{i(\omega+\omega_L)\tau} \tag{5.17b}$$

$$\mathcal{F}(E_X(t-\tau)e^{-i\omega_L t}) = \mathcal{E}_X(\omega-\omega_L)e^{i(\omega-\omega_L)\tau} \tag{5.17c}$$

Equation 5.16 can be written as

$$P(k,\tau) = \left| \mathcal{E}_X(\omega)e^{i\omega\tau} + i\frac{k\sqrt{U_p}}{\omega_L}\left(\mathcal{E}_X(\omega+\omega_L)e^{i(\omega+\omega_L)\tau} + \mathcal{E}_X(\omega-\omega_L)e^{i(\omega-\omega_L)\tau}\right) \right|^2 . \tag{5.18}$$

where $\omega = \frac{k^2}{2} + I_p$. In the frequency domain, the attosecond pulse is complex and can be written as $\mathcal{E}_X(\omega) = |\mathcal{E}_X(\omega)|e^{i\phi(\omega)}$.The photoelectron spectrum (Equation 5.18) varies with the delay τ, and can be written as a sum of three fourier components: a constant term, a term oscillating with frequency ω_L and a term oscillating with the frequency $2\omega_L$:

$$P(k,\tau) = P_0(k,\tau) + P_{\omega_L}(k,\tau) + P_{2\omega_L}(k,\tau) \tag{5.19}$$

where

$$P_0(k,\tau) = |\mathcal{E}_X(\omega)|^2 + \frac{k^2 U_p}{\omega_L^2}\Big(|\mathcal{E}_X(\omega+\omega_L)|^2 + |\mathcal{E}_X(\omega-\omega_L)|^2\Big) \tag{5.20a}$$

$$P_{\omega_L}(k,\tau) = 2\frac{k\sqrt{U_p}}{\omega_L}\mathcal{IM}\Big(\mathcal{E}_X^*(\omega)\mathcal{E}_X(\omega+\omega_L)e^{i\omega\tau} + \mathcal{E}_X^*(\omega)\mathcal{E}_X(\omega-\omega_L)e^{-i\omega\tau}\Big) \tag{5.20b}$$

$$P_{2\omega_L}(k,\tau) = 2\frac{k^2 U_p}{\omega_L^2}\mathcal{RE}\Big(\mathcal{E}_X(\omega-\omega_L)\mathcal{E}_X^*(\omega+\omega_L)e^{-i2\omega\tau}\Big) \tag{5.20c}$$

The $P_{\omega_L}(k,\tau)$ term can be filtered out from $P(k,\tau)$ by using a band pass filter centered at ω_L. Due to interference between the spectral components, $P_{\omega_L}(k,\tau)$ has the following form:

$$P_{\omega_L}(k,\tau) = A(\omega)\sin(\omega\tau+\alpha). \tag{5.21}$$

where α is dependent on the spectral phase $\phi(\omega)$ $\left(\mathcal{E}_X(\omega) = |\mathcal{E}_X(\omega)|e^{i\phi(\omega)}\right)$. Equation 5.21 does not necessarily have an analytical form, so $\phi(\omega)$ can be retrieved by minimizing the least square error function between the measured and guessed phase angle [89]

5.4 Limitations of the existing techniques

Two attosecond pulse characterization techniques have been discussed, both of which are based on the strong field approximation (SFA) in which the ionized electron is described by a volkov wave. However, in order to make the pulse retrieval feasible, the volkov dipole transition matrix element (DTME) has been neglected (i.e. $d^V_{\mathbf{k}+\mathbf{A}(t)}$ has been set to one in Equations 5.4 and 5.16). Even if it *were* included, would the physics of the photoionization process be accurately captured? In the previous chapter on recombination amplitude, we saw the limitations of using plane waves - a volkov state is a plane wave whose momentum can change with time - to describe the

recombination step. It is shown that by replacing the plane wave by the scattering eigenstate of the atomic potential, qualitative features like the cooper-minimum in the high-order harmonic spectrum of Argon could be reproduced. This suggests that the physics of the photoionization process, which is the reverse of the recombination process, will be better captured if the photoelectrons were described using scattering states.

In what follows, we employ a more sophisticated SFA where the photoelectron is described using a coulomb-volkov state. As we will show, this captures the physics of the photoionization process while keeping the expression of the photoelectron spectrum (Equation 5.4) to resemble that of a FROG Spectrogram. We show that without our improvement, characterization of low-energy EUV pulses can have significant error. Finally, we also propose a simple method for reducing the errors for the existing FROG-CRAB algorithm

A technique called improved-PROOF (iPROOF) has been developed that accounts for the dipole transition matrix element (DTME) in the retrieval algorithm by explicitly describing the laser-assisted photoionization process within the first- and second-order perturbation theory [90]. One main advantage of the FROG-CRAB technique over the interferometric techniques like PROOF and iPROOF is that the temporal profile of both the attosecond pulse and the IR field can be retrieved simultaneously. This can be a limitation in pump-probe experiments where both the IR and the EUV pulse need to be characterized.

5.5 Coulomb Volkov improved FROG-CRAB

5.5.1 Improvement in the FROG-CRAB model function

A coulomb volkov state is a mixture between the spatial part of an incoming scattering eigenstate of the atom and the temporal part of a Volkov state: $\Psi_k^{CV}(\mathbf{r},t) = \psi_k^{sc}(\mathbf{r})e^{-iS_k(t)}$ [30]. The incoming scattering state is given by

$$\psi_k(\mathbf{r}) = \frac{1}{\sqrt{k}} \sum_{l=0}^{\infty} \sum_{m=-l}^{m=l} i^l e^{-i(\delta_l+\sigma_l)} \frac{u_{kl}^{sc}(r)}{r} Y_{lm}(\Omega_r) Y_{lm}^*(\Omega_k) \tag{5.22}$$

and the bound atomic state is given by

$$\psi_g(\mathbf{r}) = \frac{u_g(r)}{r} Y_{l0}(\Omega_r); \tag{5.23}$$

Using the dipole selection rule ($\Delta l = \pm 1$ and $\Delta m = 0$), $d_{k+A(t)}^{CV}$ can be calculated in spherical coordinates. For Ne, Ar, Kr, and Xe we get

$$\begin{aligned} d_{\mathbf{k}}^{CV} =& c_0 e^{-i(\delta_0+\sigma_0)} \langle u_g|r|u_{k0}^{sc}\rangle Y_{00}^*(\Omega_k) + \\ & c_2 e^{-i(\delta_2+\sigma_2)} \langle u_g|r|u_{k2}^{sc}\rangle Y_{20}^*(\Omega_k) \end{aligned} \tag{5.24}$$

The two right-hand-side terms of Eq.(3) represent the transition from the bound p orbital to the s and the d orbitals of the continuum state respectively. The coefficient $c_l = \langle Y_{10}|\cos\theta|Y_{l0}\rangle$ is the angular integral. Since only electrons ejected along the z direction are observed in the experiment, Ω_k is set to zero. Inserting Equation 5.24 in the standard photoelectron distribution (Equation 5.4), we get the coulomb volkov modified expression

$$P^{CV}(k,\tau) = \left| \int_{-\infty}^{\infty} dt e^{-i\varphi(k,t)} d_{\mathbf{k}+\mathbf{A}(t)}^{CV} E_X(t-\tau) e^{i(W+I_p)t} \right|^2. \tag{5.25}$$

In Figure 5-9, the magnitude and phase of the CV DTMEs of Ne, Ar, Kr and Xe have been plotted against the photon energy of the EUV pulse. The photoelectron spectrum of an atom, in the absence of an IR field, is obtained by multiplying the EUV spectrum by the DTME and then downshifting the spectrum by the corresponding ionization potential. As shown in Figure 5-9, the atom acts like a filter: for high energies, the response is flat; however, for low energies, the atom behaves like a low pass filter that imparts a nonlinear phase on the photoelectron pulse. Thus, its transfer function causes the amplitude and phase of the photoelectron pulse to differ from that of the EUV pulse.

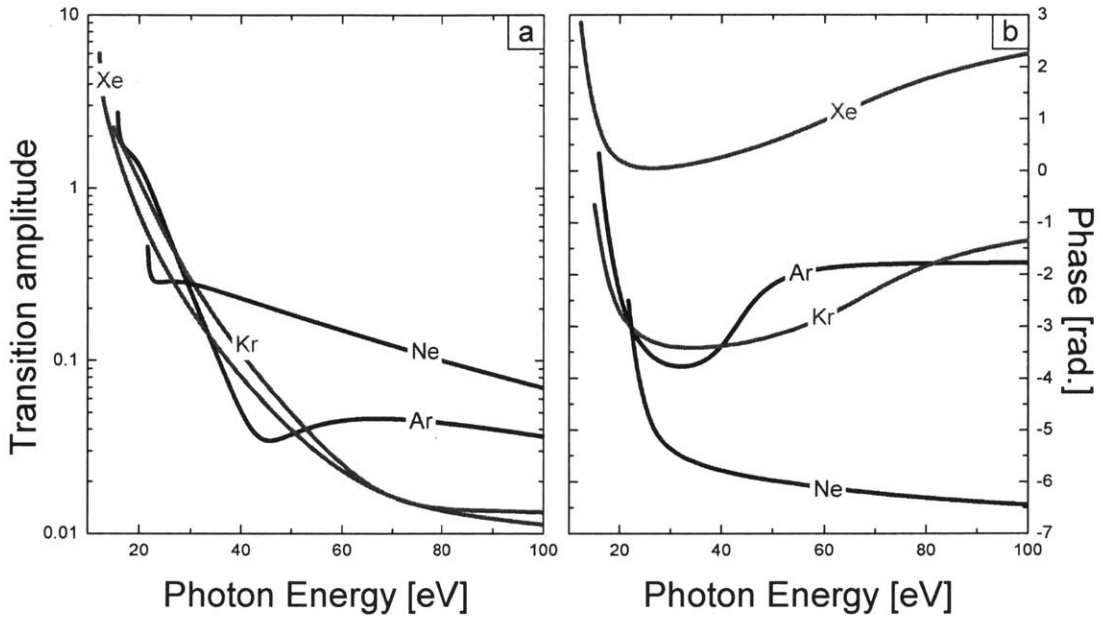

Figure 5-9: The magnitude (a)and phase (b) of dipole transition matrix element $d_{\mathbf{k}}^{CV}$.for a one photon absorption

CV states have been used successfully to model Compton scattering by bound and free electrons [30]. The CV improved SFA has been used to model the Cooper minimum in the HHG spectrum of Ar which is attributed to the minimum in the recombination amplitude [91, 4]. Since the recombination of an electron and ion in the presence of an IR field is the reverse of ionization in the presence of IR field, this motivates our use of the CV improved SFA for FROG-CRAB.

To emphasize this, we have simulated the photoelectron pulse generated from argon by transform-limited (TL) EUV pulses ($\cos^2$ shape with 30eV span) centered at 30eV, 45eV and 60eV. In Figure 5-10(a-c), the magnitude and phase of the DTME is plotted. The spectral range corresponding to each of the three EUV pulses are highlighted. The generated photoelectron pulses is shown in Figure 5-10 (d-f). For comparison, the respective TL photoelectron pulses are shown. In Figure 5-10 (d), due to the second-order dispersion, which is apparent from the parabolic shape of the phase around 30eV, the photoelectron pulse is broadened. The EUV pulse centered

at 45eV experiences first- and third-order phase dispersion, which results in a photoelectron pulse which is time-shifted. A side-lobe is formed due to an interference between the high and low frequencies in the photoelectron wavepacket (Figure 5-10 (e)). Finally, the EUV pulse centered at 60eV sees a nearly flat phase and amplitude response, and, as a result, the photoelectron pulse remains transform-limited (Figure 5-10 (f)).

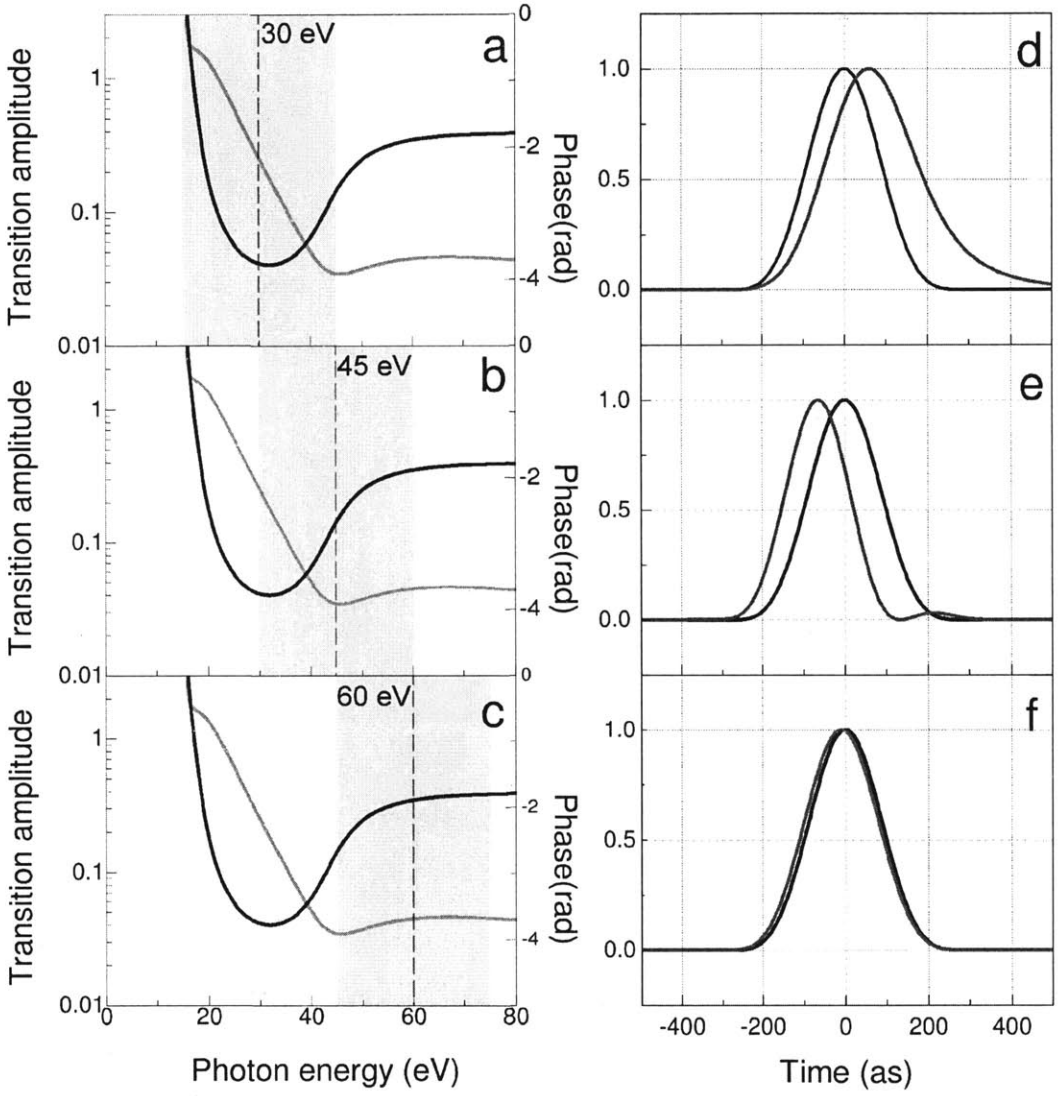

Figure 5-10: In (a), (b) and (c) the EUV spectral bandwidths (yellow) are superimposed on the magnitude (green) and phase (blue) of $d_{\mathbf{k}}^{CV}$ of Ar. In (d),(e)and(f), the corresponding normalized photoelectron pulses (red) and TL photoelectron pulses (black) are shown.

5.5.2 Improvement in the retrieval algorithm

Next, the limitations of the least squares general projection algorithm (LSGPA) [7], which sets the DTME to 1, are studied. The streaking pulse in our simulation is centered at 800nm, has a pulse duration of 8fs FWHM, and a peak intensity of $2.5 \times 10^{12}\text{W/cm}^2$. For the transform limited EUV pulse used in Figure 5-10(a) (200as full width at half maximum (FWHM)), we produce two spectrograms. The first (Figure 5-11a), ignores the DTME dispersion by setting $d^V_{\mathbf{k}+\mathbf{A}(t)} = 1$, while the second (Figure 5-11b) resembles a realistic spectrogram where $d^V_{\mathbf{k}+\mathbf{A}(t)}$ is replaced by $d^{CV}_{\mathbf{k}+\mathbf{A}(t)}$. Two notable differences between the two spectrograms are the presence of spectral breathing as a function of delay, and a broadening of the bandwidth in Figure 5-11b, signifying the chirp and spectral shaping due to the DTME's inclusion. Next, we analyze the EUV pulse retrieved from the realistic spectrogram using the LSGPA. We find that the retrieved EUV pulse in this case (Figure 5-12a, blue circles) differs significantly from the actual EUV pulse (Figure 5-12a, solid line).

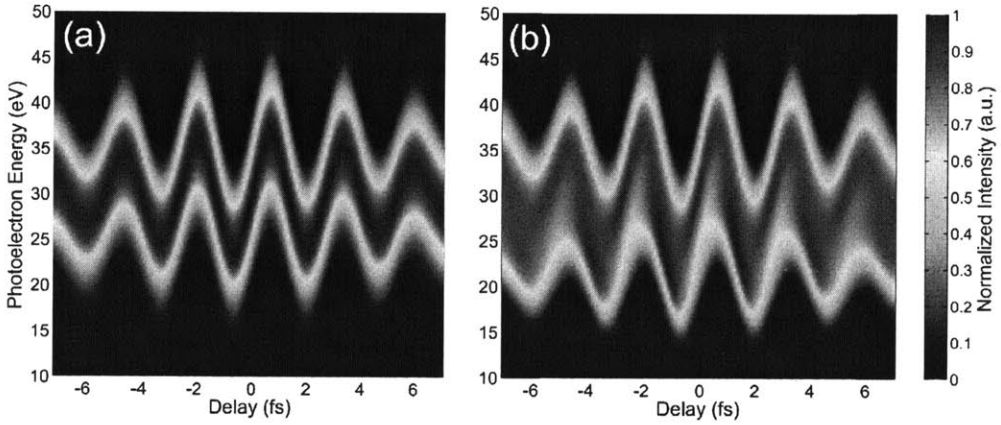

Figure 5-11: Comparison of simulated spectrograms (normalized) by numerical integration of Eq.(1) where $d^V_{\mathbf{k}+\mathbf{A}(t)} = 1$ (a) and where the DTME is set to $d^{CV}_{\mathbf{k}+\mathbf{A}(t)}$ (b).

To improve the retrieval, one would need to include the DTME inside of the LSGPA. However, the LSGPA, being based on Fourier transforms, is not compatible with nonseparable functions of energy and time. It can be shown that, when the EUV pulse is much shorter than one cycle of the IR, the DTME in Eq.(1) can be approxi-

mated by $d^{CV}_{\mathbf{k}+\mathbf{A}(\tau)}$, and the phase modulator term by $\varphi(t,k) \approx \varphi(\tau,k)+\varphi'(\tau,k)(t-\tau)$ where φ' is the derivative of the phase with respect to t. After making these approximations and using a few Fourier transform properties, Equation 5.25 can be rewritten as

$$P(k,\tau) \approx \left| \int_{-\infty}^{\infty} dt \Gamma(t) e^{i(\varphi(\tau,k_0)+\varphi'(\tau,k_0))} e^{iWt} \right|^2 \tag{5.26}$$

where $\Gamma(t) = F^{-1}(d^{CV}_{k(\omega)} E_X(\omega + I_p))$, $E_X(\omega)$ is the frequency domain form of the EUV pulse, and $e^{i(\varphi(\tau,k_0)+\varphi'(\tau,k_0)t)} \approx e^{i\varphi(t+\tau,k_0)}$ is the time-shifted phase-gate. This result is similar to that obtained in [92]. Given this expression, one finds that any FROG retrieval algorithm will retrieve $\Gamma(t)$, i.e. the photoelectron pulse, rather than the EUV pulse. Thus, the EUV pulse can be obtained by simply dividing out the DTME in the frequency domain.

Applying this analysis to the retrieved pulse in Figure 5-12a (blue circles) reduces the root mean squared error (RMSE) from .078 to .0092, nearly an order of magnitude improvement. The qualitative nature of the pulse is also improved (see Figure 5-12a) as the side-lobe seen in the retrieved pulse (due to the third-order phase dispersion of the DTME) does not exist in the corrected pulse (pink triangles). In order to test the effect of the EUV pulse duration on the accuracy of this correction, a pre-chirped EUV pulse with a group delay dispersion (GDD) of $0.043 fs^2$, which stretches the pulse to a duration of $700as$ FWHM (Figure 5-12b), is used to generate a spectrogram (not shown). Despite the attosecond pulse having a duration of more than one quarter of the IR cycle, the RMSE was again significantly reduced from 0.122 to 0.040.

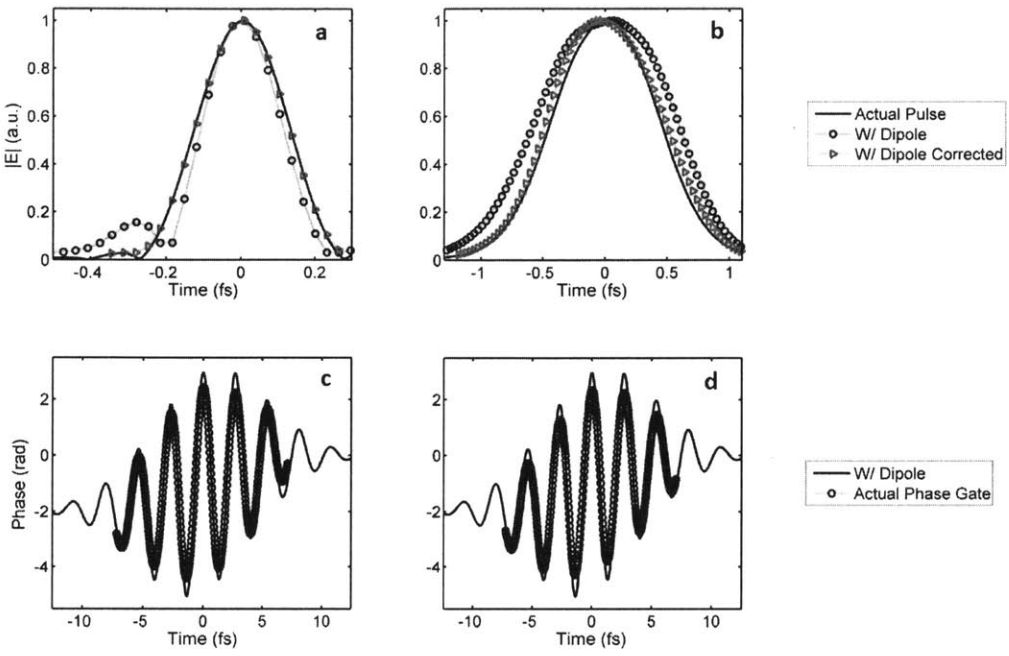

Figure 5-12: Pulse retrieval for a TL and a chirped pulse (GDD of 0.043 fs^2) . The actual pulse (solid black) is compared to that retrieved without DTME correction (blue circles) and with DTME correction (pink triangles).

5.6 Conclusion

In conclusion, an improved FROG-CRAB method has been shown that includes a more accurate model of the physics of the photoionization process. It has been emphasized that the FROG-CRAB method retrieves the amplitude and phase of the photoelectron pulse rather than the EUV pulse, which can be a source of significant error. Therefore, for an accurate retrieval of the EUV pulse, the dispersion of the DTME needs to be included in the retrieval algorithm, especially for EUV pulses with photon energies close to the ionization potential. If the EUV pulse is much shorter than a cycle of the streaking pulse, the former can be retrieved by simply dividing the retrieved photoelectron spectrum by the complex DTME, providing a correction with insignificant computational expense. It should be emphasized that if the accuracy of the DTME is further improved - for instance, by the inclusion of the long-range coupling between the photoelectron pulse and atom [93] - it can easily be

incorporated in our retrieval technique.

Bibliography

[1] P. B. Corkum and Ferenc Krausz. Attosecond science. *Nature Physics*, 3(6):381–387, June 2007.

[2] Paul R. Berman, Ennio Arimondo, and Chun C. Lin. *Advances in Atomic, Molecular, and Optical Physics*. Academic Press, July 2012.

[3] Vasileios-Marios Gkortsas, Siddharth Bhardwaj, Chien-Jen Lai, Kyung-Han Hong, Edilson L. Falco-Filho, and Franz X. Kärtner. Interplay of mulitphoton and tunneling ionization in short-wavelength-driven high-order harmonic generation. *Physical Review A*, 84(1):013427, July 2011.

[4] Hans Jakob Wörner, Hiromichi Niikura, Julien B. Bertrand, P. B. Corkum, and D. M. Villeneuve. Observation of electronic structure minima in high-harmonic generation. *Physical Review Letters*, 102(10):103901, March 2009.

[5] J.A.R. Samson and W.C. Stolte. Precision measurements of the total photoionization cross-sections of he, ne, ar, kr, and xe. *Journal of Electron Spectroscopy and Related Phenomena*, 123(23):265–276, May 2002.

[6] J.J. Yeh and I. Lindau. Atomic subshell photoionization cross sections and asymmetry parameters: 1 z 103. *Atomic Data and Nuclear Data Tables*, 32(1):1–155, January 1985.

[7] J. Gagnon, E. Goulielmakis, and V. S. Yakovlev. The accurate FROG characterization of attosecond pulses from streaking measurements. *Applied Physics B*, 92(1):25–32, July 2008.

[8] F Quéré, Y Mairesse, and J Itatani. Temporal characterization of attosecond XUV fields. *Journal of Modern Optics*, 52(2-3):339360, 2005.

[9] T. H. Maiman. Stimulated optical radiation in ruby. *Nature*, 187(4736):493–494, August 1960.

[10] Gerard A. Mourou, Toshiki Tajima, and Sergei V. Bulanov. Optics in the relativistic regime. *Reviews of Modern Physics*, 78(2):309–371, April 2006.

[11] M. Ferray, A. L'Huillier, X. F. Li, L. A. Lompre, G. Mainfray, and C. Manus. Multiple-harmonic conversion of 1064 nm radiation in rare gases. *Journal of Physics B: Atomic, Molecular and Optical Physics*, 21(3):L31, February 1988.

[12] K. C. Kulander and B. W. Shore. Calculations of multiple-harmonic conversion of 1064-nm radiation in xe. *Physical Review Letters*, 62(5):524–526, January 1989.

[13] M. Lewenstein, Ph. Balcou, M. Yu. Ivanov, Anne LHuillier, and P. B. Corkum. Theory of high-harmonic generation by low-frequency laser fields. *Physical Review A*, 49(3):2117–2132, March 1994.

[14] Ahmed H. Zewail. Femtochemistry: atomic-scale dynamics of the chemical bond. *The Journal of Physical Chemistry A*, 104(24):5660–5694, June 2000.

[15] J Itatani, J Levesque, D Zeidler, Hiromichi Niikura, H Ppin, J-C Kieffer, P B Corkum, and D M Villeneuve. Tomographic imaging of molecular orbitals. *Nature*, 432(7019):867–871, 2004.

[16] Olga Smirnova, Yann Mairesse, Serguei Patchkovskii, Nirit Dudovich, David Villeneuve, Paul Corkum, and Misha Yu Ivanov. High harmonic interferometry of multi-electron dynamics in molecules. *Nature*, 460(7258):972–977, 2009.

[17] Eleftherios Goulielmakis, Zhi-Heng Loh, Adrian Wirth, Robin Santra, Nina Rohringer, Vladislav S. Yakovlev, Sergey Zherebtsov, Thomas Pfeifer, Abdallah M. Azzeer, Matthias F. Kling, Stephen R. Leone, and Ferenc Krausz. Real-time observation of valence electron motion. *Nature*, 466(7307):739–743, August 2010.

[18] C. J. Joachain, N. J. Kylstra, and R. M. Potvliege. *Atoms in Intense Laser Fields*. Cambridge University Press, 2012.

[19] A D Shiner, B E Schmidt, C Trallero-Herrero, H J W¨rner, S Patchkovskii, P B Corkum, J-C Kieffer, F Lgar, and D M Villeneuve. Probing collective multi-electron dynamics in xenon with high-harmonic spectroscopy. *Nature Physics*, 7(6):464–467, 2011.

[20] Ariel Gordon and Franz X. Kärtner. Quantitative modeling of single atom high harmonic generation. *Physical Review Letters*, 95(22):223901, November 2005.

[21] Ariel Gordon, Franz X. Kärtner, Nina Rohringer, and Robin Santra. Role of many-electron dynamics in high harmonic generation. *Physical Review Letters*, 96(22):223902, June 2006.

[22] John W. Cooper. Photoionization from outer atomic subshells. a model study. *Physical Review*, 128(2):681–693, October 1962.

[23] Anthony Starace. Theory of atomic photoionization. pages 1–62, 2012.

[24] Kenneth C. Kulander. Time-dependent hartree-fock theory of multiphoton ionization: Helium. *Physical Review A*, 36(6):2726–2738, September 1987.

[25] Sang-Kil Son, Linda Young, and Robin Santra. Impact of hollow-atom formation on coherent x-ray scattering at high intensity. *Physical Review A*, 83(3):033402, March 2011.

[26] Robert W. Boyd. *Nonlinear Optics.* Academic Press, January 2003.

[27] Anh-Thu Le, R. R. Lucchese, S. Tonzani, T. Morishita, and C. D. Lin. Quantitative rescattering theory for high-order harmonic generation from molecules. *Physical Review A*, 80(1):013401, July 2009.

[28] Harald Friedrich. *Theoretical Atomic Physics.* Springer, 2006.

[29] A. Becker and F. H. M. Faisal. Intense-field many-body s-matrix theory. *Journal of Physics B: Atomic, Molecular and Optical Physics*, 38(3):R1, February 2005.

[30] Manoj Jain and Narkis Tzoar. Compton scattering in the presence of coherent electromagnetic radiation. *Physical Review A*, 18(2):538–545, August 1978.

[31] A. M. Perelomov, V. S. Popov, and M. V. Terent'ev. Ionization of atoms in an alternating electric field. *Soviet Journal of Experimental and Theoretical Physics*, 23:924, November 1966.

[32] A. M. Perelomov, V. S. Popov, and M. V. Terent'ev. Ionization of atoms in an alternating electric field: II. *Soviet Journal of Experimental and Theoretical Physics*, 24:207, January 1967.

[33] A. M. Perelomov and V. S. Popov. Ionization of atoms in an alternating electrical field. III. *Soviet Journal of Experimental and Theoretical Physics*, 25:336, August 1967.

[34] L. Lev Davidovich Landau and E. Evgeni Mikhalovich Lifshits. *Quantum Mechanics: Non-Relativistic Theory.* Butterworth-Heinemann, 1977.

[35] Denys Bondar. Instantaneous multiphoton ionization rate and initial distribution of electron momentum. *Physical Review A*, 78(1), 2008.

[36] Gennady L. Yudin and Misha Yu. Ivanov. Nonadiabatic tunnel ionization: Looking inside a laser cycle. *Physical Review A*, 64(1):013409, June 2001.

[37] Jon P. Davis and Philip Pechukas. Nonadiabatic transitions induced by a timedependent hamiltonian in the semiclassical/adiabatic limit: The twostate case. *The Journal of Chemical Physics*, 64(8):3129–3137, April 1976.

[38] Vasileios-Marios Gkortsas, Siddharth Bhardwaj, Edilson L. Falco-Filho, Kyung-Han Hong, Ariel Gordon, and Franz X. Kärtner. Scaling of high harmonic generation conversion efficiency. *Journal of Physics B: Atomic, Molecular and Optical Physics*, 44(4):045601, February 2011.

[39] Ivan P. Christov, Margaret M. Murnane, and Henry C. Kapteyn. High-harmonic generation of attosecond pulses in the Single-Cycle regime. *Physical Review Letters*, 78(7):1251–1254, February 1997.

[40] S. X. Hu and L. A. Collins. Intense laser-induced recombination: The inverse above-threshold ionization process. *Physical Review A*, 70(1):013407, July 2004.

[41] Ariel Gordon, Robin Santra, and Franz X. Krtner. Role of the coulomb singularity in high-order harmonic generation. *Physical Review A*, 72(6):063411, December 2005.

[42] Misha Yu. Ivanov, Thomas Brabec, and Neal Burnett. Coulomb corrections and polarization effects in high-intensity high-harmonic emission. *Physical Review A*, 54(1):742–745, July 1996.

[43] Ariel Gordon, Christian Jirauschek, and Franz X. Kärtner. Numerical solver of the time-dependent schrdinger equation with coulomb singularities. *Physical Review A*, 73(4):042505, April 2006.

[44] L. Lehtovaara, J. Toivanen, and J. Eloranta. Solution of time-independent schrdinger equation by the imaginary time propagation method. *Journal of Computational Physics*, 221(1):148–157, January 2007.

[45] R Kosloff and D Kosloff. Absorbing boundaries for wave propagation problems. *J. Comput. Phys.*, 63(2):363376, April 1986.

[46] Shu-Wei Huang, Giovanni Cirmi, Jeffrey Moses, Kyung-Han Hong, Siddharth Bhardwaj, Jonathan R Birge, Li-Jin Chen, Enbang Li, Benjamin J Eggleton, Giulio Cerullo, and Franz X Kärtner. High-energy pulse synthesis with sub-cycle waveform control for strong-field physics. *Nature Photonics*, 5(8):475–479, 2011.

[47] A. Wirth, M. Th Hassan, I. Grgura, J. Gagnon, A. Moulet, T. T. Luu, S. Pabst, R. Santra, Z. A. Alahmed, A. M. Azzeer, V. S. Yakovlev, V. Pervak, F. Krausz, and E. Goulielmakis. Synthesized light transients. *Science*, 334(6053):195–200, October 2011. PMID: 21903778.

[48] A. Baltuka, Th Udem, M. Uiberacker, M. Hentschel, E. Goulielmakis, Ch Gohle, R. Holzwarth, V. S. Yakovlev, A. Scrinzi, T. W. Hnsch, and F. Krausz. Attosecond control of electronic processes by intense light fields. *Nature*, 421(6923):611–615, February 2003.

[49] E. Priori, G. Cerullo, M. Nisoli, S. Stagira, S. De Silvestri, P. Villoresi, L. Poletto, P. Ceccherini, C. Altucci, R. Bruzzese, and C. de Lisio. Nonadiabatic three-dimensional model of high-order harmonic generation in the few-optical-cycle regime. *Physical Review A*, 61(6):063801, May 2000.

[50] Armelle de Bohan, Philippe Antoine, Dejan B. Miloevi, and Bernard Piraux. Phase-dependent harmonic emission with ultrashort laser pulses. *Physical Review Letters*, 81(9):1837–1840, August 1998.

[51] L E Chipperfield, J S Robinson, J W G Tisch, and J P Marangos. Ideal waveform to generate the maximum possible electron recollision energy for any given oscillation period. *Physical Review Letters*, 102(6):063003, February 2009. PMID: 19257585.

[52] Kyung-Han Hong, Chien-Jen Lai, Vasileios-Marios Gkortsas, Shu-Wei Huang, Jeffrey Moses, Eduardo Granados, Siddharth Bhardwaj, and Franz X. Kärtner. High-order harmonic generation in xe, kr, and ar driven by a 2.1-m source: High-order harmonic spectroscopy under macroscopic effects. *Physical Review A*, 86(4):043412, October 2012.

[53] J. Levesque, D. Zeidler, J. P. Marangos, P. B. Corkum, and D. M. Villeneuve. High harmonic generation and the role of atomic orbital wave functions. *Physical Review Letters*, 98(18):183903, May 2007.

[54] Stefan Pabst. Atomic and molecular dynamics triggered by ultrashort light pulses on the atto- to picosecond time scale. *The European Physical Journal Special Topics*, 221(1):1–71, April 2013.

[55] H. J Wörner, J. B Bertrand, D. V Kartashov, P. B Corkum, and D. M Villeneuve. Following a chemical reaction using high-harmonic interferometry. *Nature*, 466(7306):604 607, 2010. 632HA Times Cited:12 Cited References Count:30.

[56] Hans A Bethe and Edwin E Salpeter. *Quantum mechanics of one- and two-electron atoms.* Dover Publications, Mineola, N.Y., 2008.

[57] L. V. Keldysh. Ionization in the field of a strong electromagnetic wave. *Sov. Phys. JETP*, 20(5):13071314, 1965.

[58] Olga Smirnova, Michael Spanner, and Misha Ivanov. Coulomb and polarization effects in sub-cycle dynamics of strong-field ionization. *Journal of Physics B: Atomic, Molecular and Optical Physics*, 39(13):S307–S321, 2006.

[59] J. Higuet, H. Ruf, N. Thir, R. Cireasa, E. Constant, E. Cormier, D. Descamps, E. Mvel, S. Petit, B. Pons, Y. Mairesse, and B. Fabre. High-order harmonic spectroscopy of the cooper minimum in argon: Experimental and theoretical study. *Physical Review A*, 83(5):053401, May 2011.

[60] G. Breit and H. A. Bethe. Ingoing waves in final state of scattering problems. *Physical Review*, 93(4):888–890, February 1954.

[61] Frank Herman and Sherwood Skillman. *Atomic structure calculations.* Prentice-Hall, 1963.

[62] U Fano and J Cooper. Spectral distribution of atomic oscillator strengths. *Reviews of Modern Physics*, 40(3):441–507, 1968.

[63] P. G. Burke and K. T. Taylor. R-matrix theory of photoionization. application to neon and argon. *Journal of Physics B: Atomic and Molecular Physics*, 8(16):2620, November 1975.

[64] M Y Amusia. Rearrangement effects in photoionization. *Applied Optics*, 19(23):4042–4050, 1980.

[65] W. R. Johnson, C. D. Lin, K. T. Cheng, and C. M. Lee. Relativistic random-phase approximation. *Physica Scripta*, 21(3-4):409, January 1980.

[66] W. R. Johnson and C. D. Lin. Multichannel relativistic random-phase approximation for the photoionization of atoms. *Physical Review A*, 20(3):964–977, September 1979.

[67] Anthony F Starace. Trends in the theory of atomic photoionization. *Applied Optics*, 19(23):4051, 1980.

[68] K.-N. Huang, W.R. Johnson, and K.T. Cheng. Theoretical photoionization parameters for the noble gases argon, krypton, and xenon. *Atomic Data and Nuclear Data Tables*, 26(1):33–45, January 1981.

[69] Guanhua Yao and Shih-I Chu. Generalized pseudospectral methods with mappings for bound and resonance state problems. *Chemical Physics Letters*, 204(3-4):381–388, 1993.

[70] Xiao-Min Tong and Shih-I Chu. Theoretical study of multiple high-order harmonic generation by intense ultrashort pulsed laser fields: A new generalized pseudospectral time-dependent method. *Chemical Physics*, 217(2-3):119–130, 1997.

[71] Steven Manson and John Cooper. Photo-ionization in the soft x-ray range: 1Z dependence in a central-potential model. *Physical Review*, 165(1):126–138, 1968.

[72] Stefan Pabst, Loren Greenman, David A. Mazziotti, and Robin Santra. Impact of multichannel and multipole effects on the cooper minimum in the high-order-harmonic spectrum of argon. *Physical Review A*, 85(2):023411, February 2012.

[73] J. Cooper and R. N. Zare. Angular distribution of photoelectrons. *The Journal of Chemical Physics*, 48(2):942–943, September 2003.

[74] G.V. Marr and J.B. West. Absolute photoionization cross-section tables for helium, neon, argon, and krypton in the VUV spectral regions. *Atomic Data and Nuclear Data Tables*, 18(5):497–508, November 1976.

[75] K Codling, R G Houlgate, J B West, and P R Woodruff. Angular distribution and photoionization measurements on the 2p and 2s electrons in neon. *Journal of Physics B: Atomic and Molecular Physics*, 9(5):L83–L86, 1976.

[76] R G Houlgate, K Codling, G V Marr, and J B West. Angular distribution and photoionization cross section measurements on the 3p and 3s subshells of argon. *Journal of Physics B: Atomic and Molecular Physics*, 7(17):L470–L473, 1974.

[77] W Johnson and K Cheng. Photoionization of the outer shells of neon, argon, krypton, and xenon using the relativistic random-phase approximation. *Physical Review A*, 20(3):978–988, 1979.

[78] L. E. Hargrove, R. L. Fork, and M. A. Pollack. LOCKING OF HeNe LASER MODES INDUCED BY SYNCHRONOUS INTRACAVITY MODULATION. *Applied Physics Letters*, 5(1):4–5, November 2004.

[79] L.P. Barry, P.G. Bollond, J. M Dudley, J.D. Harvey, and R. Leonhardt. Autocorrelation of ultrashort pulses at 1.5 mu;m based on nonlinear response of silicon photodiodes. *Electronics Letters*, 32(20):1922–1923, September 1996.

[80] C. Iaconis and I.A. Walmsley. Self-referencing spectral interferometry for measuring ultrashort optical pulses. *IEEE Journal of Quantum Electronics*, 35(4):501–509, April 1999.

[81] Daniel J. Kane and Rick Trebino. Single-shot measurement of the intensity and phase of an arbitrary ultrashort pulse by using frequency-resolved optical gating. *Optics Letters*, 18(10):823–825, May 1993.

[82] Jonathan R. Birge, Richard Ell, and Franz X. Kärtner. Two-dimensional spectral shearing interferometry for few-cycle pulse characterization. *Optics Letters*, 31(13):2063–2065, July 2006.

[83] U. Morgner, F. X. Kärtner, S. H. Cho, Y. Chen, H. A. Haus, J. G. Fujimoto, E. P. Ippen, V. Scheuer, G. Angelow, and T. Tschudi. Sub-two-cycle pulses from a kerr-lens mode-locked ti:sapphire laser. *Optics Letters*, 24(6):411–413, March 1999.

[84] Rick Trebino, Kenneth W. DeLong, David N. Fittinghoff, John N. Sweetser, Marco A. Krumbgel, Bruce A. Richman, and Daniel J. Kane. Measuring ultrashort laser pulses in the time-frequency domain using frequency-resolved optical gating. *Review of Scientific Instruments*, 68(9):3277–3295, September 1997.

[85] D.J. Kane. Recent progress toward real-time measurement of ultrashort laser pulses. *IEEE Journal of Quantum Electronics*, 35(4):421–431, April 1999.

[86] M. Hentschel, R. Kienberger, Ch Spielmann, G. A. Reider, N. Milosevic, T. Brabec, P. Corkum, U. Heinzmann, M. Drescher, and F. Krausz. Attosecond metrology. *Nature*, 414(6863):509–513, November 2001.

[87] Y. Mairesse and F. Quéré. Frequency-resolved optical gating for complete reconstruction of attosecond bursts. *Physical Review A*, 71(1):011401, January 2005.

[88] P. M. Paul, E. S. Toma, P. Breger, G. Mullot, F. Augé, Ph Balcou, H. G. Muller, and P. Agostini. Observation of a train of attosecond pulses from high harmonic generation. *Science*, 292(5522):1689–1692, June 2001. PMID: 11387467.

[89] Michael Chini, Steve Gilbertson, Sabih D. Khan, and Zenghu Chang. Characterizing ultrabroadband attosecond lasers. *Optics Express*, 18(12):13006 13016, June 2010.

[90] G. Laurent, W. Cao, I. Ben-Itzhak, and C. L. Cocke. Attosecond pulse characterization. *Optics Express*, 21(14):16914–16927, July 2013.

[91] Siddharth Bhardwaj, Sang-Kil Son, Kyung-Han Hong, Chien-Jen Lai, Franz X. Krtner, and Robin Santra. Recombination-amplitude calculations of noble gases, in both length and acceleration forms, beyond the strong-field approximation. *Physical Review A*, 88(5):053405, November 2013.

[92] V. S. Yakovlev, J. Gagnon, N. Karpowicz, and F. Krausz. Attosecond streaking enables the measurement of quantum phase. *Physical Review Letters*, 105(7):073001, August 2010.

[93] S. Nagele, R. Pazourek, J. Feist, K. Doblhoff-Dier, C. Lemell, K. Tőkési, and J. Burgdörfer. Time-resolved photoemission by attosecond streaking: extraction of time information. *Journal of Physics B: Atomic, Molecular and Optical Physics*, 44(8):081001, April 2011.